Vol. 8 No. 1 June 2015
ISSN 2005-9043

Leading to the world of tomorrow

KIST Today

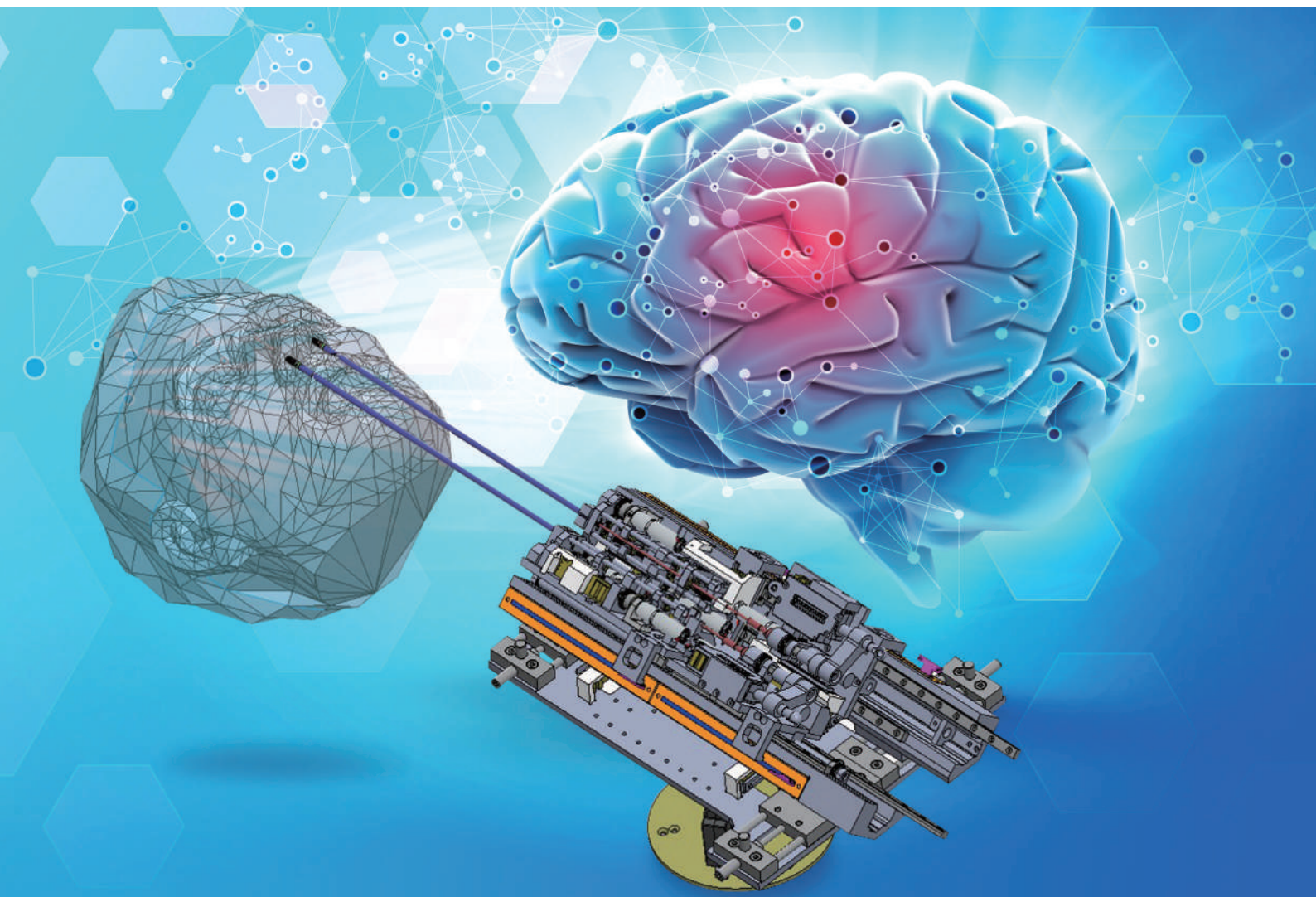

Bio / Medical

- ***Technical Review***
  Micro/Nanomechanical Sensors for Various Biological Applications

Materials / Systems

- ***Technical Review***
  Black Phosphorus, a Novel Material with High Carrier Mobility and Device Functionality

Energy / Environment

- ***Technical Review***
  Making Better Batteries for Sustainable Future: Batteries Based on Multivalent Charge Carriers

Korea Institute of Science and Technology

Contents

Foreword

In 1970, a commentary entitled “Korean Science Institute: A Model for Developing Nations?” was published in “*Science*”. The article speculated as to whether the establishment of KIST and its agressive R&D efforts would lead to the rapid economic development of Korea and serve as a prototype for other developing countries. Many decades have passed since that question was posed, and the answer is increasingly clear.

Since its establishment in 1966 when Korea had essentially no S&T capabilities, KIST has become a leading science research institute. Its early success was attributable not only to the active support of the Korean government, but also the support of the US government and the Battelle Memorial Institute, which provided invaluable assistance to properly equip KIST with research systems, infrastructure, administrative systems and staff training. At that time, Korea was a recipient of foreign aid, but now has evolved to donor status, as evidenced by KIST’s active engagement in promoting economic growth in other countries through science and technology.

One good example of such efforts is the V-KIST Project currently being implemented to establish a research institute of science and technology in Vietnam. The title of this research institute includes the name KIST, to reflect hopes that V-KIST will lead in the development of Vietnam just as KIST led Korea to become an economic powerhouse. KIST will provide active support for the construction and operation of V-KIST, including plans for its development, key avenues of research, training of researchers and research infrastructure. KIST continues to provide assistance to other countries as well, reflected in its IRDA program to train researchers from developing countries and its participation in a variety of ODA S&T programs, such as the construction of a bio-ethanol plant in Indonesia and the Korea-Mongolia Science and Technology Cooperation Center in Mongolia.

The article published in “*Science*” used a question mark in considering whether KIST could become a model for developing countries. We are now seeing the time when the question mark is being transformed to an exclamation point, indicating our very positive influence on the developing world. When we celebrate the 50th anniversary of KIST in 2016, it will be as a growing supporter of S&T development in nations who can benefit the most from the assistance and expertise we can provide. I am grateful for your interest and encouragement as we pursue these efforts.

Dr. Byung Gwon Lee
President of KIST

[Technical Review]

Micro/Nanomechanical Sensors for Various Biological Applications

Jinsik Kim
Center for BioMicrosystems
d14509@kist.re.kr

Kyo Seon Hwang
Center for BioMicrosystems
kshwang@kist.re.kr

Introduction

A “biosensor” is an analytical system which uses a transducer to sense specific biological elements and then transmit signals via an electrical component to a computer or operating system. The transducers that convert the presence of the biological elements into other kinds of signals can operate on a variety of physicochemical principles, including optical, piezoelectric, electrochemical, mechanical, etc., and are named accordingly. Each biosensor is developed to target specific biological elements such as proteins, deoxyribonucleic acid (DNA), cells or enzymes.

Following advances in micro and nanofabrication technologies, improvements have been made to sensors so that they are smaller, more efficient, have higher sensitivity and are able to be fabricated on a wafer-scale. In particular, mechanical biosensors have been greatly improved by reducing the physical size of the sensing device, and by extension, the biosensor itself, thereby enhancing its accuracy by reducing the effect of gravity. Most mechanical biosensors have their own resonant frequency and detect bio-elements when a shift in resonant frequency occurs due to biomolecular interactions. This resonant frequency shift generally occurs when biological elements are captured on the surface of the mechanical sensors. The captured bio-elements result in changes to the total mass and surface stresses, precipitating changes in resonant frequency.

The capture of biological elements on the surfaces of mechanical biosensors is accomplished with a highly selective affinity-based assay. The high specificity or affinity of assay of the targeted bio-materials is achieved with functionalized device surfaces. Generally, the interaction of antibody and antigen and chemical absorption at functionalized peptides have been used as highly specified assays.

In this article, we discuss our investigations of micro/nanomechanical biosensors driven by a piezoelectric layer and their various applications, such as rapid discrimination of DNA strands, determination of blood viscosity/density and biomaterial-based electronic noses.

Opto-calorimetric microcantilever sensors for rapid discrimination of DNA strands

Microcalorimetric infrared (IR) spectroscopy based on a bimetallic microcantilever has offered rapid molecular identification with high selectivity and sensitivity since it combines the sensitivity of a thermomechanical sensor and the selectivity of IR spectroscopy without the need for labels or the immobilization of probe molecules [1, 2]. The absorption of IR radiation by molecules adsorbed on the microcantilever results in a small variation in the cantilever temperature depending on the IR absorption characteristics of the molecules. Then this minute temperature variation as a function of illuminating IR wavelength is sensitively transduced as nanomechanical deflection of the bimetallic microcantilever, resulting in nanomechanical IR spectra. Furthermore, resonance frequency shifts of the cantilever enable the determination of the adsorbed mass of target molecules, making this technique quantitative. This multi-modal sensing method allows quantitative molecular recognition with minimal calibration [3]. In our research, we have demonstrated a rapid and facile prescreening technique for DNA and single nucleotide difference (SND) without the need for immobilized probe molecules. The selective detection of DNA with multiple nucleotides and rapid screening of SND were enabled by analyzing variations in the profile of calorimetric IR spectra due to different relative molar ratios of individual nucleotides.

Figure 1(a) shows the schematic illustration of the experimental setup. This technique provides two orthogonal signals in a single transducer platform from both pyroelectric and piezoelectric properties of the PZT microcantilever, as shown in Figures 1(b) and (c), used in the quantitative determination of adsorbed DNA mass and their spectral characteristics. The phonons generated by the nonradiative decay process heat the cantilever at a specific IR wavelength which can be observed as variations in the voltage generated by the cantilever. The microcalorimetric IR spectrum can be obtained by a differential plot of the amplitude of the voltage generation as a function of IR wavenumber with and without target molecules.

Figure 2(a) shows the normalized microcalorimetric IR absorption spectra of each nucleotide (A_{20}, T_{20}, G_{20}, and C_{20}). The IR spectra of each nucleotide were acquired separately as references and were consistent with previously reported results [5, 6]. The adsorbed masses of

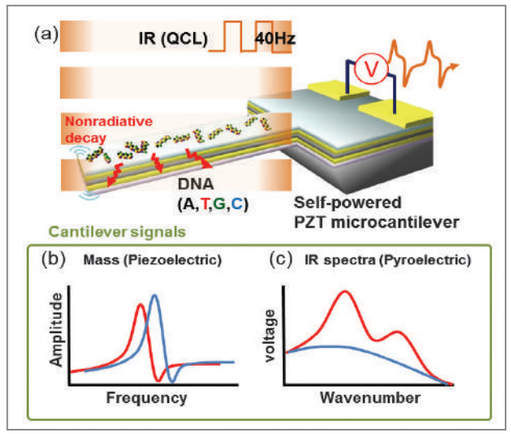

Figure 1. (a) Schematic illustration of a self-powered calorimetric IR spectrometer based on a PZT microcantilever. Schematic illustration of variations in the resonance frequency (b) and the microcalorimetric IR spectra (c) of the PZT microcantilever without (blue) and with (red) target molecules from its piezoelectric as well as pyroelectric properties [4].

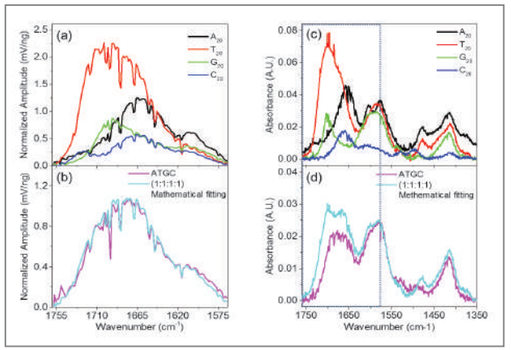

Figure 2. (a) Normalized calorimetric IR adsorption spectra of each nucleotide (A_{20} (black), T_{20} (red), G_{20} (green), and C_{20} (blue)). (b) Normalized calorimetric IR adsorption spectrum of ATGC (magenta) and a mathematically fitted IR spectrum of (1:1:1:1) individual nucleotide. (c) Conventional FTIR spectra of each nucleotide (A_{20} (black), T_{20} (red), G_{20} (green), and C_{20} (blue). (d) FTIR spectrum of ATGC (magenta) and a mathematically fitted IR spectrum of (1:1:1:1) individual nucleotide. The dashed square represents the dynamic range of the microcalorimetric IR spectra [4].

A_{20}, T_{20}, G_{20}, and C_{20} on the cantilever were approximately 4.02 ng, 3.44 ng, 3.72 ng, and 3.16 ng, respectively. Figures 2(c) and (d) show the conventional FTIR spectra of each nucleotide (A_{20}, T_{20}, G_{20}, and C_{20}), ATGC, and a weighted linear superposition of the individual nucleotide spectrum. The peak positions and profiles in the microcalorimetric IR spectra of ssDNA strands in Figures 2(a) and (b) agree quite well with those in the FTIR spectra.

To demonstrate whether or not this method is capable of distinguishing different components of nucleotides and SND in a given DNA strand, microcalorimetric IR spectra of various DNA strands on the PZT microcantilevers were collected. Figure 3 shows the normalized calorimetric IR spectra of three different strands (GTTGAA, ACTTCA, ACTCCA). The adsorbed masses of GTTGAA, ACTTCA, and ACTCCA on the cantilever were approximately 2.12 ng, 1.62 ng, and 2.06 ng, respectively. Different profiles of the normalized IR spectra in Figure 3(a) are mainly attributed to a different ratio between guanine and cytosine. GTTGAA is composed of $A_6T_7G_7$, whereas ACTTCA is composed of $A_7T_6C_7$. The dominant peaks in the profiles of the strands were induced by carbonyl C=O displacement (1694 cm^{-1}) in guanine and carbonyl C=O displacement (1724 and 1666 cm^{-1}) in cytosine, respectively. Figure 3(b) shows the normalized IR spectra of SND between ACTTCA and ACTCCA. ACTTCA is composed of $A_7T_6C_7$, whereas ACTCCA is composed of $A_7T_5C_8$. Even though the difference in the ssDNA was only a single nucleotide, the normalized IR spectra of ACTTCA and ACTCCA were highly distinguishable. The dominant peaks in the profiles of these strands were due to carbonyl C=O displacement (1718 cm^{-1} and 1709 cm^{-1}) and N-H bending mode (1661 cm^{-1}) in thymine

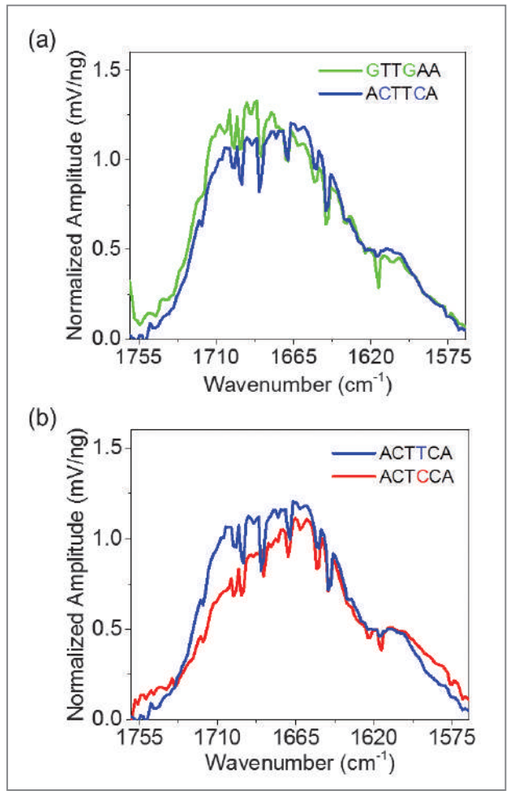

Figure 3. Normalized microcalorimetric IR adsorption spectra of (a) one different component (GTTGAA (green): ACTTCA (blue)) and (b) SND (ACTTCA (blue): ACTCCA (red)) [4].

and carbonyl C=O displacement (1724 cm^{-1} and 1666 cm^{-1}) in cytosine. The IR spectra of GTTGAA, ACTTCA, and ACTCCA fit very well with the data obtained using a combination of individual spectra of nucleotides following the linear superposition principle.

We have demonstrated a facile, rapid, and quantitative detection of DNA and screening of SND using immobilization-free, self-powered PZT microcantilevers. The microcalorimetric IR spectroscopy based on a PZT microcantilever offers excellent selectivity due to the unique molecular vibrational spectra of individual nucleotides in the mid IR region which can be monitored using the pyroelectric property of a PZT thin film.

Microdiaphragms sensors for the determination of blood viscosity and density

A blood test is the most widely used method for early diagnosis of illness because it is a simple, easy, and affordable test to confirm a disease. The diagnostic methods for blood tests are generally of three types: biochemical analyses that quantify the constituents of blood; cellular evaluations that give information about blood cells, such as a complete blood count, mean corpuscular volume, etc.; and molecular profiling that detects antibodies using specific antibody-antigen immune reactions. Of these, molecular profiling is the most widely used since it can diagnose a disease in early onset by detecting biomarkers, such as disease marker proteins or disease-specific DNA formed in the blood. Additionally, measuring the physical properties of blood, the density and the viscosity, is a promising method that can improve the accuracy of blood-based diagnosis. Diagnosis of diseases through measurements of the physical properties of blood can also be simple and inexpensive. Moreover, a condition, such as a cardiovascular disease, that is closely associated with changes in the physical properties of blood, can be diagnosed at an early stage using only

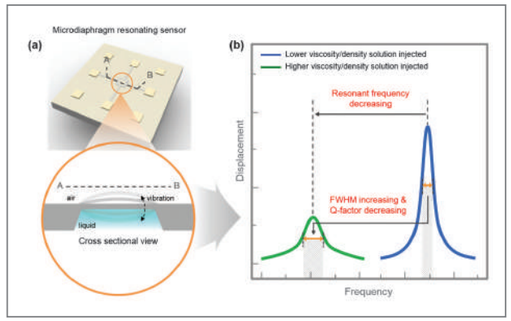

Figure 4. Schematic diagram of the density and viscosity of a liquid determined using a microdiaphragm resonating sensor. (a) Illustration of the microdiaphragm resonating sensor and cross sectional view of the resonating diaphragm. (b) Comparison of the resonant peaks of the microdiaphragm after injection with solutions of lower and higher density and viscosity [9].

measurements of the density and viscosity of blood. Many studies have actually demonstrated a correlation between cardiovascular disease and the density and viscosity of blood [7, 8]. In light of these findings, we developed a PZT microdiaphragm resonating sensor based on a microelectromechanical system fabrication technology which allowed us to measure the density and viscosity of glycerol/water mixtures and buffered serum solutions.

Figure 4 presents a schematic diagram of the detection of the density and viscosity of a liquid using our microdiaphragm resonating sensor. Due to the PZT actuating layer, the microdiaphragm resonating sensor vibrates when the test liquid is loaded under the surface of the sensor, as shown in Figure 4(a). Figure 4(b) shows that the microdiaphragm resonating sensor has a different resonant frequency and Q-factor depending on the density and viscosity of the loaded liquid. Generally, an increased liquid density decreases the resonant frequency and an increased liquid viscosity increases the FWHM of the microdiaphragm resonating sensor. By correlating the changes in the resonant frequency and the FWHM according to the density and viscosity of the tested liquid, the density and viscosity of an unknown liquid can then be determined with the microdiaphragm resonating sensor.

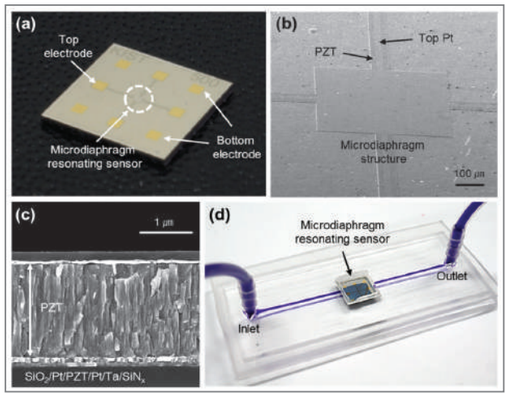

Figure 5. Fabricated microdiaphragm resonating sensor that measures the density and viscosity of a liquid. (a) Photograph of the unit sensor chip. (b) Top view and (c) cross sectional view SEM photographs of the microdiaphragm structure composed of SiO_2/Pt/PZT/Pt/Ta/SiN_x multi-layers. (d) Microdiaphragm resonating sensor packaged with a PDMS liquid cell [9].

The microdiaphragm resonating sensor we developed was fabricated as shown in Figure 5(a). Figures 5(b) and (c) show the scanning electron microscope (SEM) images of the fabricated sensor. The 500 μm square sensor, composed of SiO_2/Pt/PZT/Pt/Ta/SiN_x layers, had a thickness of about 3.45 μm. A liquid cell was used to load the liquid sample on the diaphragm resonating sensor, as shown in Figure 5(d).

In order to validate the performance of the sensor within the range of the density and viscosity of blood, the response of the microdiaphragm resonating sensor was measured using solutions of finely adjusted concentrations of glycerol. The sensor's response characteristics were measured according to the shift in the resonant frequency (Δf), the shift of FWHM (ΔFWHM), and Q-factor (Figure 6).

The change in the weight percentage of glycerol from 0 to 50% in DI water indicates density ranges from 0.998 to 1.1466 × 10^3 kg/m^3 and a viscosity range from 1 to 8.40 cP. Figure 6(a) shows the results of the numerically predicted (solid lines) and experimentally measured results (symbols) as a function of liquid density. The experimental results are the average values, and the standard deviations are less than 0.1 kHz for the (1,1) mode. As evidenced by the graph, we confirmed that the numerical prediction agreed quite well with the experimental data, especially for the (1,1) mode. The density sensitivity (Δf/Δdensity) of each mode was also calculated. The density sensitivity for the (1,1) mode was 28.03 Hz/kg·m^{-3} and for the (2,2) mode was 81.85 Hz/kg·m^{-3}. The sensitivity of the (2,2) mode was three times larger than the sensitivity of the (1,1) mode. Considering that the density of blood generally changes by less than 0.005 × 10^3 kg/m^3, depending on the type of disease, the microdiaphragm resonating sensor can thus be effective in measuring changes in blood density. The experimental FWHMs were determined and used to evaluate the performance of the

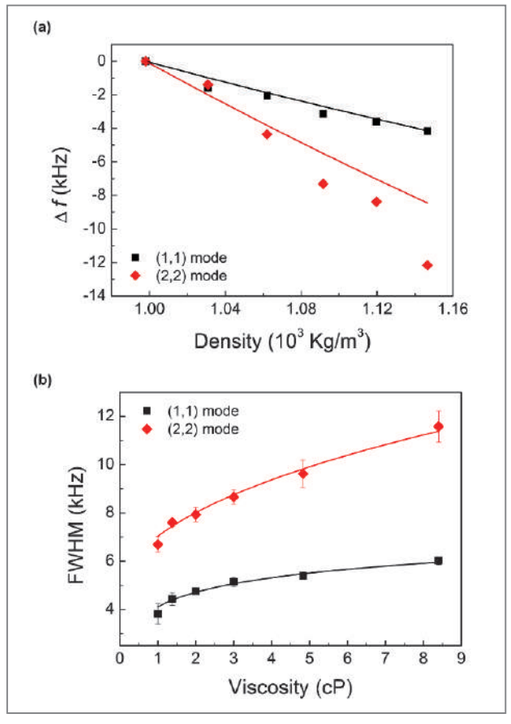

Figure 6. Changes in the (a) resonant frequency and (b) FWHM related to a mixture of glycerol and DI water with varying densities and viscosities within the range of the physical properties of blood [9].

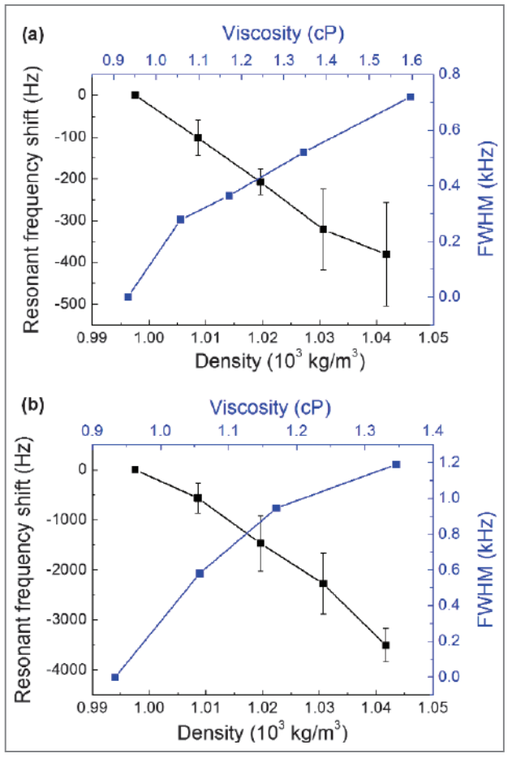

Figure 7. The resonant frequency shift and FWHM depending on the density and viscosity of PBS-buffered human serum in (a) (1,1) mode and (b) (2,2) mode [9].

microdiaphragm resonating sensor as a function of the viscosity of the liquid. The ΔFWHM of the (1,1) mode was 3.813, 4.435, 4.874, 5.142, 5.389, and 6.012 kHz as viscosity changed, while the ΔFWHM in the (2,2) mode was 6.694, 7.605, 7.935, 8.659, 9.625, and 11.579 kHz. The ΔFWHM had a logarithmic relationship in accordance with the change in the viscosity of the liquid. These results therefore confirm that the microdiaphragm resonating sensor can detect viscosity of liquid.

We verified the analysis potential of the microdiaphragm resonating sensor on the variation of blood density and viscosity by using real human serum (normal human serum, Merck Millipore, Darmstadt, Germany). To mimic the viscosity and density changes that actually occur in human blood, the human serum was mixed with phosphate buffered saline (PBS). The density and viscosity of the PBS buffer and the human serum were 0.998 × 10^3 kg/m^3, 1.042 × 10^3 kg/m^3 and 0.933 cP, 1.597 cP, respectively. Next, a range of mixtures was prepared by increasing the human serum portion by increments of 25% in each sample of PBS buffer. The resulting viscosities of the samples were 0.933 cP, 1.058 cP, 1.17 cP, 1.346 cP and 1.597 cP and the densities were 0.998 × 10^3 kg/m^3, 1.009 × 10^3 kg/m^3, 1.020 × 10^3 kg/m^3, 1.031 × 10^3 kg/m^3 and 1.042 × 10^3 kg/m^3. The density of the mixed human serum samples was calculated according to the serum portion of each solution and the viscosity of samples was measured using a viscometer (DV-I Prime Viscometer, Brookfield Engineering Laboratories, MA, US). Figure 7 shows the resonance frequency shift and FWHM with respect to the density and viscosity of PBS-buffered human serum. The black line represents the relation of density-resonant frequency shift, the blue line shows the relation of viscosity-FWHM. Similar to the results obtained with the glycerol/water mixtures, the resonant frequency decreased and the FWHM increased in each mode. This result demonstrates that the microdiaphragm resonating sensor is suitable for the measurement of small changes on human serum density and viscosity.

Microcantilever sensor-based electronic nose applications

Recently, there has been an increase in demand for sensitive and selective vapor detection systems because chemical vapor detection systems can be utilized for environmental monitoring, healthcare systems and explosives detection [10, 11]. In particular, the increased use of improvised explosive devices (IEDs) against civilian and military populations has prompted an urgency to investigate explosive-related chemical vapor sensors

based on micro/nanotechnology. Dinitrotoluene (DNT), which is the decomposition product of trinitrotoluene (TNT), has been used as a target material for explosive chemical detection since TNT is commonly used to make IEDs. Our team at KIST has quantitatively detected 2,4-dinitrotoluene (DNT) vapor in the gas phase at concentrations as low as parts-per-billion (ppb) based on resonant frequency changes of a DNT-specific peptide receptor immobilized microcantilever. We used the peptide receptor to enhance the selectivity of the cantilever sensors. The sequence of the peptide that specifically interacted with DNT was identified by phase display cloning [12]. The peptide receptor allowed the microcantilever sensor to selectively detect DNT in material vapor containing compounds with chemically similar structures (toluene and nitrotoluene).

To demonstrate multi-target detection, we fabricated a cantilever array chip with four reaction chambers that includes four cantilever units (Figure 8). The piezoelectric microcantilever has a unique function of direct electrical detection via piezoelectric materials. We fabricated the microcantilever with piezoelectric ($Pb(Zr_{0.52}Ti_{0.48})O_3$, PZT) thin films composed of multi-layers of SiN_x/Ta/Pt/PZT/Pt/SiO_2. The microcantilever had a total thickness of 2.88μm and featured a self-actuating and self-sensing operation without the aid of optical components, thus allowing for easy application in a hand-held mobile device. For the multiplexing sensor, we designed four micro-wells (four cantilever units) and acquired individual surface functionalization. In the cantilever surface functionalization process, the gold-coated cantilever arrays were immersed in a 70-μL microreaction chamber, as shown in Figures 8(d) and (e).

To identify the DNT selective peptide, a DNT derivative, 4-(2,4-dinitrophenyl)butan-1-amine, was synthesized and immobilized on a gold surface through the formation of a self-assembled monolayer (SAM). The immobilized DNT derivative plays an important role in improving the interaction between the DNT target and the displayed 12-mer peptides. The DNT-specific peptides used in the microcatilevers sensor were isolated from the M13 phase library through biopanning. In this screening procedure, Lys-Met-His-Thr-Ala-Ser-Leu-Ser-Gln-Pro-Leu-Met was found to be the strongest DNT binding sequence.

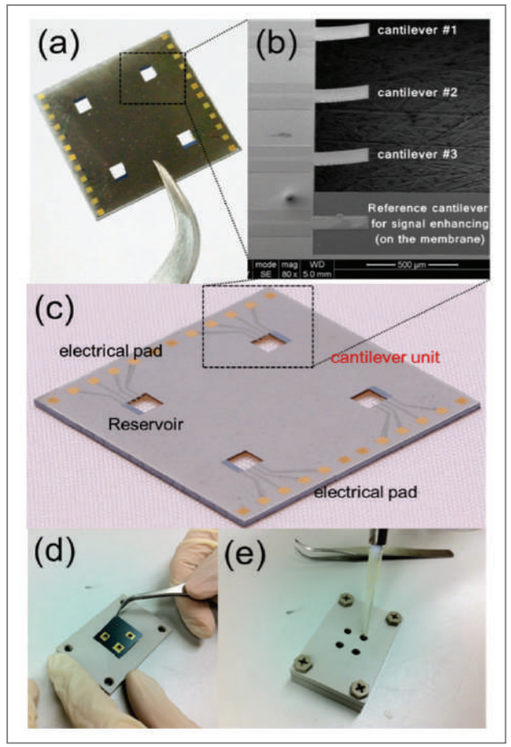

Figure 8. Multiplexed cantilever array chip with four reaction chambers. (a) Photograph of multiplexed cantilever including four cantilever units. (b) SEM photograph of one cantilever unit containing three cantilevers and a reference cantilever to enhance the signal by cancelling the parasitic capacitance. (c) Close up photographic image of multiplexed cantilever, (d) cantilever chip loading, and (e) sample loading for multiplexing functionalization on the fabricated reaction chamber [13].

In order to verify that the peptide could function as receptor molecules in the gas phase and that DNT vapor could be detected by this DNT-specific peptide immobilized microcantilever, the functionalized microcantilever array chip containing the immobilized peptide receptor was immersed in a sensing chamber.

The sensing chamber was designed to pass a controlled gas flow from the mass flow controller (MFC) and to connect the electrodes of the microcantilever chip and measurement unit.

Figure 9 shows the resonance response of the microcantilevers when the microcantilevers were continuously exposed to DNT, toluene, and nitrotoluene vapor. The concentration of the injected DNT vapor was about 100 ppb and DNT vapor was generated by flowing nitrogen gas through solid DNT at atmospheric conditions and room temperature [15]. Standard toluene and nitrotoluene at a concentration of 200 ppm was also used. As shown in Figure 9, when the functionalized microcantilever was exposed to the gas vapor after reaching steady-state by nitrogen pursing, the resonance response of the microcantilever was extremely fast and sensitive. When three different gas vapors were injected into the sensing chamber, the change in the resonant frequency of the reference microcantilever was about 2 Hz in all cases (green line). This demonstrated that physical adsorption of the injected vapor on the microcantilever surface gave rise to a small change in the resonant frequency when compared with the change that occurred due to the specific interaction. Based on the response of the reference microcantilever, the differential resonant frequency (difference of resonant frequency change between the DNT-specific peptide immobilized microcantilever and reference microcantilever) demonstrated that the response was generated from only specific interactions. This result indicates that the peptide on the sensor surface can be used as a receptor in the gas phase for chemical compound detection. Moreover, it also demonstrates that the peptide receptor can be applied in a number of micro/nanotechnology-based sensing platforms with high sensitivity to improve the selectivity of the developed sensors. The differential quantity of the resonant frequency change was about 10 Hz due to mass loading of the DNT vapor and surface stress generated on the microcantilever structure [16]. The specific interaction between DNT and DNT-specific peptide may affect the mechanical properties of the microcantilever, resulting in a greater resonant frequency change than the mass loading [17].

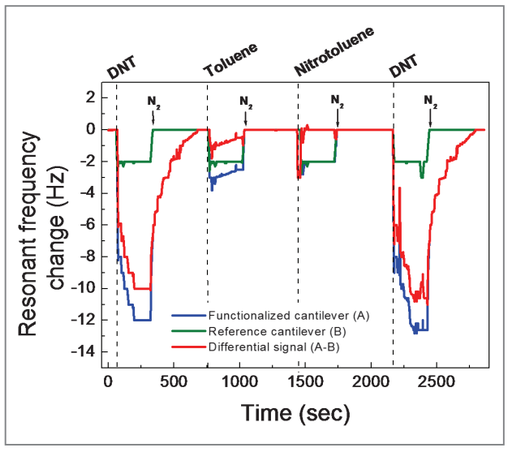

Figure 9. Changes in the resonant frequency of a microcantilever containing a DNT-specific peptide receptor. Both the DNT as a specific target vapor and toluene/nitrotoluene as a nonspecific chemical vapor were injected sequentially into the sensing chamber where the functionalized microcantilever was located [14].

When nitrogen was injected into the sensing chamber after the resonance signal reached equilibrium, the resonant frequency of the functionalized microcantilever returned to the same level observed before the interaction event. The recovery time of the microcantilever exposed to the specific target was longer than the recovery time of the microcantilevers exposed to the nonspecific targets (toluene and nitrotoluene) because of the difference in the interaction force. Even though a small resonant frequency change was observed from binding between the peptide receptor and chemically similar structured nonspecific targets, the resonant responses were instantly recovered by nitrogen pursing. After signal recovery of the microcantilever sensor by nitrogen pursing, we confirmed that the resonant frequency of the DNT-specific peptide immobilized microcantilever decreased and ranged from 9.3 to 10.6 Hz (differential resonant frequency change).

Conclusion

We have developed micro/nanomechanical biosensors that provide specific target detection in liquid and/or air environments. Monitoring the mechanical property changes of micro/nanomechanical biosensors allows accurate read-outs of various biological information. Indeed, micro/nanomechanical biosensors are flexible enough to be used as common bioanalysis tools for high-throughput detection of biomolecules as well as the mechanical properties of biofluids and specific gas vapors. We anticipate micro/nanomechanical biosensors will lead to the development of useful analytical systems that can be used in a number of fields.

Note

This article and images are drawn from "Rapid discrimination of DNA strands using an opto-calorimetric microcantilever sensor" in *Lab on a Chip*, Vol. 14, pg. 4659, "Piezoelectric layer embedded-microdiaphragm sensors for the determination of blood viscosity and density" in *Applied Physics Letters*, Vol. 105, pg. 153504, "Peptide receptor-based selective dinitrotoluene detection suing a microcantilever sensor" in *Biosensors & Bioelectronics*, Vol. 30, pg. 249, and "Multifunctionalized cantilever systems for electronic nose applications" in *Analytical Chemistry*, Vol. 84, pg. 8240.

References

[1] Arakawa ET, Lavrik NV, Rajic S, Datskos PG. *Ultramicroscopy* 2003; 97: 459-465.

[2] Wig A, Arakawa ET, Passian A, Ferrell TL, Thundat T. *Sens. Actuators B* 2006; 114: 206-211.

[3] Kim S, Lee D, Liu X, Neste CV, Jeon S, Thundat T. *Sci. Rep.* 2013; 3: 1111.

[4] Lee D, Hwang KS, Kim S, Thundat T. *Lab Chip* 2014; 14: 4659-4664.

[5] Dovbeshko GI, Gridina NY, Kruglova EB, Pashchuk OP. *Talanta* 2000; 53: 233-246.

[6] Mateo-Marti E, Briones C, Roman E, Briand E, Pradier CM, Martin-Gago JA. *Langmuir* 2005; 21: 9510-9517.

[7] De Backer TLM, De Buyzere M, Segers P, Carlier S, De Sutter J, Van de Wiele C, De Backer G. *Atherosclerosis* 2002; 165: 367-373.

[8] Jeong SK, Cho YI, Duey M, Rosenson RS, *Cardiovasc. Drug Ther.* 2010; 24: 151-160.

[9] Kim HJ, Kim J, Zandieh O, Chae MS, Kim TS, Lee JH, Park JH, Kim S, Hwang KS. *Appl. Phys. Lett.* 2014; 105: 153504.

[10] Pinnaduwage LA, Boiadjiev V, Hawk JE, Thundat T. *Appl. Phys. Lett.* 2003; 83: 1471-1473.

[11] Southworth DR, Bellan LM, Linzon Y, Craighead HG, Parpia JM, *Appl. Phys. Lett.* 2010; 96: 163503.

[12] Jaworski JW, Raorane D, Huh JH, Majumdar A, Lee SW. *Langmuir* 2008; 24: 4938-4943.

[13] Yoo YK, Chae MS, Kang JY, Kim TS, Hwang KS, Lee JH. *Anal. Chem.* 2012; 84: 8240-8245.

[14] Hwang KS, Lee MH, Lee J, Yeo WS, Lee JH, Kim KM, Kang JY, Kim TS. *Biosens. Bioelectron.* 2011; 30: 249-254.

[15] Rose A, Zhu Z, Madigan CF, Swager TM, Bulovic V. *Nature* 2005; 434: 876-879.

[16] Hwang KS, Eom K, Lee JH, Chun DW, Cha BH, Yoon DS, Kim TS, Park JH. *Appl. Phys. Lett.* 2006; 89: 173905.

[17] Craighead HG. *Nature Nanotech.* 2007; 2: 18-19.

[**Feature Articles**]

EEG Spectral Power Analysis to Assess the Cognitive Engagement of Stroke Patients During Motor Rehabilitation

Wanjoo Park
Center for Bionics
wanjoo@kist.re.kr

Da-Hye Kim
Center for Bionics
dahyekim@kist.re.kr

Laehyun Kim
Center for Bionics
laehyunk@kist.re.kr

Introduction

Stroke is one of the leading causes of death and currently ranked the second most severe disease worldwide [1]. Stroke occurs primarily as a result of blood circulation problems in the brain, which can induce injuries to motor and sensory nerve systems [2]. Rehabilitation training involving repeated movement of the upper and lower limbs can stimulate damaged brain areas and lead to partial or full motor function recovery [3].

Previous studies have highlighted the clinical importance of a sense of accomplishment in limb movement based on a patient's motor intention during rehabilitation [4, 5]. However, in contrast to motor intention, active engagement during rehabilitation training has rarely been studied in stroke patients. Measuring patient engagement during training is important for both refining training paradigms and tracking recovery. Motivation and feedback have been known to influence the brain's reward system for rehabilitation training in the basal ganglia, playing an important role in recovering motor functions [6]. Thus, it is important to maintain stroke patients' motivation throughout rehabilitation therapy by providing feedback of active patient engagement in real time during rehabilitation training.

The present study aimed to assess patient engagement during rehabilitation training using an EEG-based brain-computer interface (BCI) system. Information related to motor task engagement can be extracted

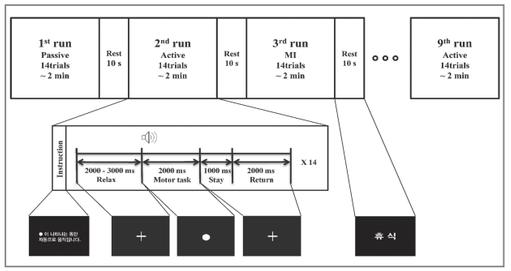

Figure 1. Experimental protocol.

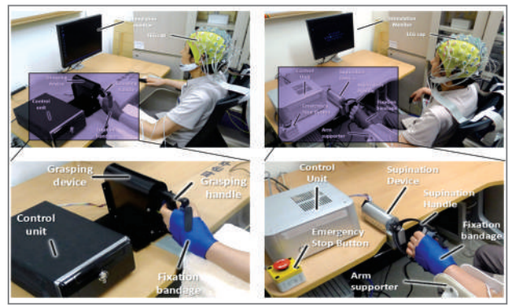

Figure 2. Two robotic devices used in our study for motor rehabilitation with grasping (a) and supination (b) movements. Expanded figures (c) and (d) represent zoomed-in sections of (a) and (b), respectively.

from distinct neural activity patterns associated with either active or passive movement. Previous research has revealed that neural activity patterns differ when a subject actively moves a limb versus passive limb movement by an external force [7, 8]. In our research, EEG patterns, specifically ERD/ERS (event-related desynchronization/event-related synchronization), were evaluated during active/passive grasping and supination movements in stroke patients. These hand movements were selected based on their involvement in upper limb rehabilitation. To examine the feasibility of developing an online monitoring tool, we compared the differences between EEG patterns associated with active and passive movements on a single-trial basis. Our hypothesis was that the ERD during an active task would be stronger than during a passive task. We hypothesized that an active task involving a wider range of neural activities would yield greater ERD.

Materials and methods

Participants

Eleven chronic stroke patients participated in this study (8 males, 3 females; mean age = 55.5 ± 5.6). All participants were first-time stroke patients, exhibited unilateral motor problems in their upper extremities/limbs, continued to have issues at least 3 months after their strokes, were between 45 and 70 years old, and were categorized as moderate or mild by FMA scoring. Participants with other cognitive disorders rendering them unable to understand task instructions and/or with other orthopedic disorders that had led to amputation or joint contraction were excluded. Mean FMA scores were 46.4 ± 9.2 for affected and 64.7 ± 1.4 for unaffected sides. Stroke patients in our study did not have a history of neurological illness and had not previously participated in an EEG experiment. The Institutional Review Boards of the Samsung Medical Center (SMC, Application Number: SMC 2013-02-091) and Korea Institute of Science and Technology (KIST, Application Number: KIST 2013-009) approved this study. Participants were informed about the study's purpose as well as the experimental procedures involved and were allowed to withdraw at any time. Written informed consent was obtained from all participants. All research data were collected and analyzed under IRB guidance.

Experimental protocol and EEG processing

We selected two types of movement for analysis, grasping and supination, because these two movements are among the last movements recovered during upper limb rehabilitation. In many actual motor rehabilitation programs, these movements are intensively trained, and therefore, were selected as target movements in our study. We expected greater ERD with the supination movement than with grasping because supination is more difficult to perform for stroke patients in general.

For each movement, three motor tasks were performed: passive (P) movement of a robotic device, active (A) movement of a robotic device, and motor imagery (MI) of kinetic movement.

Participants were trained on each motor task before the actual experiment (Figure 1). The main experiment involved nine runs of motor tasks separated by 10-second breaks. Motor task order was permutated (e.g., P-A-MI-A-MI-P-MI-P-A), such that the first task was chosen randomly for counterbalancing. Each motor task consisted of 14 trials and took approximately 2 minutes to complete. Participants performed 42 trials of each motor task for both grasping and supination movements.

At the beginning of each run, task instructions were shown on the screen. Then, a fixation cross was displayed, and participants were instructed to stare at the cross without moving their head. In the few seconds that followed, participants waited for a task cue while gazing at the fixation cross. When the fixation cross changed to a circle paired with a beep sound, the participants performed a motor task for 2000 ms. The training device stopped for 1000 ms, and the circle changed back to the fixation cross. The training device then returned to its starting position for 2000 ms. During this return period, participants were instructed not to exert control on the device.

The robotic devices used were designed to guide users to complete tasks that call for active and passive movement. Using these devices, participants performed upper limb motor tasks involving grasping and supination (Figure 2). During the experiment, participants sat in a chair that either had a board to support their arm during grasping (Figure 2a) or an arm supporter for supination movement (Figure 2b). The participant's affected hand was fastened around the handle of the device with a bandage. A monitor that displayed instructions and visual feedback was located at eye level and 1 meter away from participants. Contrast and luminosity were adjusted to optimize concentration and comfort for all participants.

For EEG signal processing, we extracted spectral features by dividing the period after the movement cue into six non-overlapping 500-ms segments. Spectral power values at each frequency (1-Hz resolution) within mu and beta bands (8–32 Hz, a total of 25 frequencies in this range) were time-averaged within each segment. This resulted in 300 (25 × 6) features for each channel. Next, a one-way ANOVA was conducted to select a subset of features that showed a significant difference between active and passive movement ($p < 0.01$). The number of selected features differed among participants and movement types.

Using the selected features as input, we classified single-trial EEG data as involving either active or passive movement. A naïve Bayes classifier was used and classification was performed using a ten-fold cross-validation method [9, 10]. Classification was performed separately for grasping and supination in all participants. Further analysis was conducted to investigate the effect of the task type on classification using features from the motor task period (0–2000 ms after the cue), the stay period (2000–3000 ms after the cue), or both.

Results

Spectral power differences between active and passive motor tasks

To investigate spectral power differences between active and passive movements during the motor tasks, event-related changes in mu and beta band power for every case were examined, as shown in Figure 3. Overall, both active and passive grasping/supination movements induced significant decreases in mu and beta band power following the movement cue (ERD; $p < 0.01$). However, there were still differences in the temporal patterns of ERD between active and passive tasks.

The active task consistently induced ERD in mu and beta band power during the entire post-stimulus period in bilateral sensorimotor areas and the supplementary motor

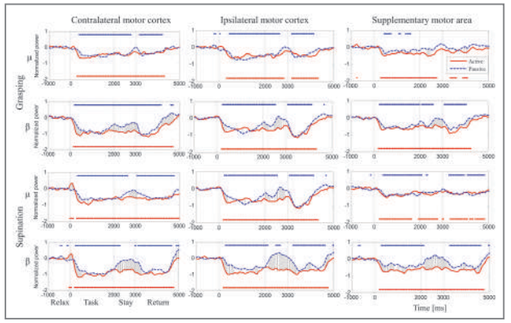

Figure 3. Comparisons of event-related changes in the power of sensorimotor rhythms between the active and passive motor tasks in bilateral motor cortical and supplementary motor areas. The point marks above and below the lines signify time points when spectral power showed a statistically significant change relative to baseline power ($p < 0.01$). The blue mark represents significant changes for the passive motor task, and the red mark represents significant changes for the active motor task. The vertical lines connecting the two curves depict time points when the spectral powers of the active and passive motor tasks were significantly different ($p < 0.01$).

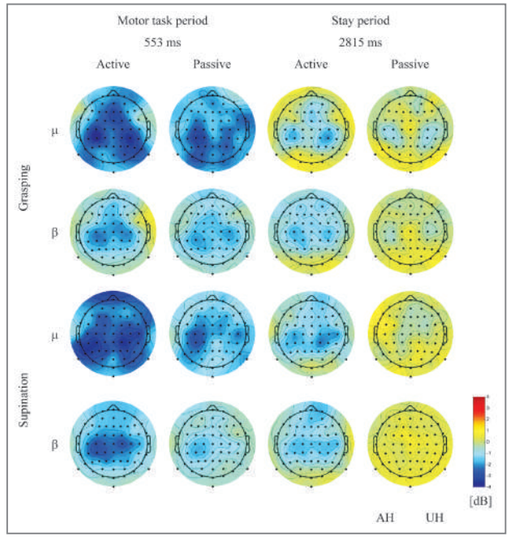

Figure 4. EEG spectral power topography during active and passive motor tasks.

area (SMA). The passive task also induced ERD in mu and beta power during the motor tasks in all three areas. However, during the period immediately after the task, it induced ERD for most bands, areas, and movement types outside of the mu band in the SMA for both movements and the beta band in the SMA for supination. During the return period in which the training device returned to its initial position, the passive task induced ERD for everything except the mu band in the SMA during grasping. Thus, it appears that the active task induces ERD more consistently throughout the whole movement period than the passive task.

We also identified time windows in which spectral power was significantly different between active and passive tasks. Differences were observed in the beta band of all areas for grasping and supination. This difference was observed to be greatest during the stay period immediately following the motor task. We also observed differences in the mu band, but only for a few windows within this same period for supination in bilateral sensorimotor cortical areas and grasping in the SMA. Paired t-tests revealed that beta band differences between the two tasks over the entire period (0–5000 ms) were larger than mu band differences for both grasping and supination movements ($p < 0.01$) in bilateral sensorimotor areas and SMA.

Figure 4 illustrates EEG spectral power topography of the grand average band power across 64 EEG channels at 553 ms and 2815 ms following the movement cue. Average ERD during the active motor task was at its maximum at 553 ms following the movement cue in bilateral sensorimotor areas and the SMA for all bands, movement types, and tasks. ERD in sensorimotor areas was also larger during the active task than the passive task ($p < 0.05$) except for the beta band with grasping movements 553 ms after movement cues. Furthermore, the associated ERD was larger in the affected hemisphere than in the unaffected hemisphere in the case of the beta band with supination movements 553 ms after movement cues ($p < 0.05$). Average spectral power during the passive motor task peaked 2815 ms after the movement cue, during the stay period that followed the motor task, in bilateral sensorimotor areas and the SMA for all bands.

Single-trial classification of active and passive motor tasks

We classified EEG features from a single trial into two classes based on whether they were associated with active or passive motor tasks. For grasping, classification accuracy was at 76.4 ± 0.1% when using features extracted from the motor task period only, 76.8 ± 0.1% when using features extracted from the stay period only, and 80.7 ± 0.1% when using a combination of both (Figure 5a). For supination, classification accuracy was at 79.3 ± 0.1%, when using features from the motor task period only, 78.5 ± 0.1% when using features from the stay period only, and 82.8 ± 0.1% when using a combination of both (Figure 5b). There was no significant difference in classification accuracy between supination and grasping. Classification accuracy was significantly higher than chance level for all participants ($p < 0.01$) except for three (3, 6, and 9) for grasping and two (2 and 8) for supination. Classification accuracy using features from both task and stay periods was significantly higher than from each alone for grasping ($p < 0.05$). For supination, classification accuracy using features from a combination of both periods was significantly higher than from just using features related to the stay period ($p < 0.05$). This was not significant when looking at the task period only ($p > 0.05$).

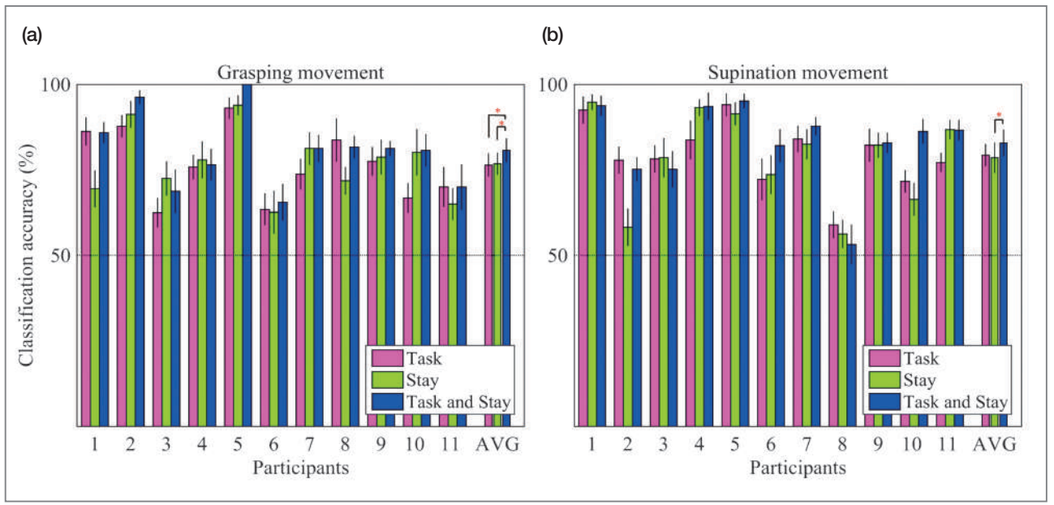

Figure 5. Classification accuracies for grasping (a) and supination (b). The result of a pairwise statistical analysis on differences in classification accuracies between three different cases is also marked (*: $p < 0.05$).

Discussion

These studies relied on ERD/ERS of sensory motor rhythms (SMRs) to detect information related to imagined, planned, or executed movements. However, since the EEG signals of patients with brain lesions due to stroke may exhibit different neuronal characteristics, it is valuable to verify if ERD/ERS of SMRs can be directly studied in stoke patients to extract motor-related information. Our results demonstrate that we can infer information about motor task engagement using ERD/ERS of SMRs in

chronic stroke patients undergoing physical therapy.

Our analysis revealed that larger differences are shown between active and passive tasks in beta band relative to mu band power in both bilateral sensorimotor areas and the SMA.

Our results also imply that beta oscillations exhibit larger differences between active and passive upper limb movements than mu oscillations, and therefore, may be more useful for monitoring engagement in stroke patients. This is in line with previous reports that showed larger post-movement increases in beta band power relative to mu band power [11, 12]. In our study, we observed clear differences in beta and mu bands, especially during the post-movement period.

Furthermore, there were significant differences between the active and passive motor tasks during the post-movement period, even though participants were supposed to stop moving during this time. We suspect that this result is dependent upon our experimental protocol. We performed video recordings for behavior analysis and observed hand movements during the task. We confirmed that patients did not immediately stop at the end of the motor task, and remained moving during active tasks. We suspect that these extra movements might be due to difficulties in motor control by stroke patients; the patients may not be able to stop moving in a timely manner as healthy individuals do. Also, we suspect that the one-second stay period in a resting position after the motor task might be too short for stroke patients to follow. Thus, the patients seemed to recognize the stay period not as a stop but rather as an interval to enable a smooth transition from the motor task to a return position. Therefore, the ERD of SMRs associated with active movement may be sustained during the stay period following active movement (see Figure 3). By contrast, for the passive motor task, ERD may have diminished quickly after the motor task period because patients did not have to volitionally stop movement. Instead, they did not receive proprioceptive feedback. These observations suggest that incorporating a holding task into the design of motor tasks may lead to better assessment of patient active engagement.

There were slight changes in power during the pre-movement period especially during the passive task. As these changes occurred particularly during the more difficult supination movement, we suspect that some on-going neural activity in preparation for the supination movement may have caused these pre-movement changes in sensorimotor rhythms. However, further investigations are required to address this issue.

Our target application is different from typical motor intention detection devices used to initiate robotic assistance. The primary application of our findings is to monitor whether stroke patients are actively participating in motor training tasks during robot-assisted therapy. In robot-assisted passive training, patients often do not pay much attention to training. This may reduce the effects of rehabilitation due to lack of motivation and feedback [13]. In clinical therapy, therefore, it is important to encourage patients to be actively engaged in a training task even though their limbs are passively moved. Monitoring active engagement may be better achieved by analyzing brain activity because active engagement is mostly a cognitive effort, making limb movements indistinguishable from passive movements. EMG or force sensing would also be unstable and inconsistent due to motor impairment. Our study focused on this point and aimed to develop an EEG-based active engagement monitoring system to provide real-time feedback of active engagement, thereby maintaining patient motivation throughout therapy.

Latent sensorimotor function can be retained through goal-directed therapy, even when a long time has passed following a stroke [6]. Rehabilitation goals may be better achieved when encouraging motivation and active engagement in stroke patients. For stroke rehabilitation therapy, an online monitoring tool that can deliver real-time feedback on performance and engagement level may lead to better rehabilitation outcomes for patients. Patient engagement may be further optimized when using an online monitoring tool with additional tools like video games and virtual reality.

We recruited patients who were categorized as moderate or mild according to FMA scoring. However, severe stroke patients may also benefit from our proposed system. Although the present study recruited stroke patients with moderate and mild FMA scores and obtained obviously active or passive training data to determine the feasibility of active engagement monitoring with EEG, the experimental protocol can easily be modified to collect data even in the absence of physical movement, as would be expected in severely affected patients. For instance, a training paradigm could be developed in which active and passive movements are discriminated by visual cues to obtain training data for these two classes for further analysis. We would expect to observe similar ERD/ERS patterns of sensorimotor rhythms to those shown in the present study. A follow-up clinical study will investigate this possibility in severe stroke patients.

Conclusion

In this study, we investigated whether we could assess active engagement in stroke patients during rehabilitation training using a non-invasive BCI. We observed that in bilateral sensorimotor cortical areas and the SMA, active movement induced larger ERD in the beta band than passive movement. A larger ERD associated with active movement was observed when participants executed motor tasks. We extracted spectral features of sensorimotor rhythms in the regions above and classified them into active or passive motor tasks on each trial. Classification accuracy was 80.7 ± 0.1% for grasping and 82.8 ± 0.1% for supination. Our results demonstrate the importance and feasibility of developing an online monitoring system of active engagement for stroke patients during motor rehabilitation training.

Note

This article and images are drawn from “Assessment of cognitive engagement in stroke patients from single-trial EEG during motor rehabilitation” in *IEEE Transaction on Neural Systems and Rehabilitation Engineering*, in press.

References

[1] Murray CJ, Lopez AD. *Lancet* 1997; 349: 1269-1276.

[2] Toole J. Philadelphia: *Lea & Febiger*. 1984; 152.

[3] Sharp SA, Brouwer BJ. *Arch. Phys. Med. Rehabil.* 1997; 78(11): 1231-1236.

[4] Petrella L, McColl M, Krupa T, Johnston J. *Brain Inj.* 2005; 19(9): 643-655.

[5] Ylvisaker M, Mcpherson K, Kayes N, Pellett E. *Neuropsychol. Rehabil.* 2008; 18(5-6): 713-741.

[6] Dobkin BH. *Lancet Neurol.* 2004; 3(9): 528-536.

[7] Tombari D, Loubinoux I, Pariente J, Gerdelat A, Albucher JF, Tardy J, Cassol E, Chollet F. *Neuroimage* 2004; 23(3): 827-839.

[8] Ramos-Murguialday A, Schürholz M, Caggiano V, Wildgruber M, Caria A, Hammer EM, Halder S, Birbaumer N. *PLoS One* 2012; 7(10): 1-10.

[9] McLachlan G. New York: Wiley. 2004;

[10] Kohavi R. in Proc. Int. Joint Conf. Artificial Intell. 1995; 1137-1145.

[11] Jurkiewicz MT, Gaetz WC, Bostan AC, Cheyne D. *Neuroimage* 2006; 32(3): 1281-1289.

[12] Chang HC, Lee PL, Lo MT, Wu YT, Wang KW, Lan GY. *IEEE Trans. Neural Syst. Rehabil. Eng.* 2013; 21(4): 607-615.

[13] Daly JJ, Wolpaw JR. *Lancet Neurol.* 2008; 7(11): 1032-1043.

Haptic and Brain-Machine Interface Lab.

Medical IT team, Center for Bionics

[**Feature Articles**]

New Secondary Metabolites of Microorganisms Isolated from Abandoned Mine and Marine Samples

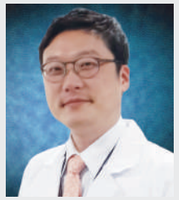

Hak Cheol Kwon
Natural Products Research Center,
KIST Gangneung Branch
hkwon@kist.re.kr

Introduction

Microbial metabolites have provided a variety of bioactive chemical structures in drug discovery programs, and the chemical diversity from the microbial resources is continuously increasing. In particular, actinomycetes have been extensively studied because they can potentially provide pharmaceutical candidates; approximately 70% of clinically useful antibiotics are derived from natural sources. However, the chemical redundancy of products isolated from these bacteria has become one of the current challenges in the discovery of novel natural product-derived drug candidates. One approach to overcome this problem is to utilize actinomycetes derived from unique habitats, such as abandoned mine environments, deep sea samples, mutualistic associations with hosts, etc.; these strains have been exploited to provide novel microbial chemotypes over the last few years. Many recent investigations have uncovered compelling evidence that actinomycetes derived from unique environmental samples might lead to the discovery of secondary metabolites with significant biological activity [1]. Research on the metabolites of marine plants and animals began in the early 1970s, yielding, to date, large numbers of novel compounds that possess potent biological activities. Despite these productive results, marine discovery efforts have not been equally extended to microorganisms, in part due to the possibility that these bacteria are introduced into the marine environment from terrestrial sources, such as wind blown spores or river runoff. However,

it is now known that new actinomycete taxa occur in the ocean and that some display specific adaptation for life in the marine environment [2]. Acidic mine drainage is generated by the oxidative reactions that result from the exposure of sulfide minerals, such as iron pyrite or iron disulfide, to the atmosphere. Acidic mine drainage is a geochemically extreme environment, and the acidic water system provides ecologically unique habitats for the growth and metabolism of diverse microbes. Under such harsh environmental conditions, microorganisms may face ecological competition, driving their metabolic potential and requiring the biosynthesis of new secondary metabolites [3].

In the course of our investigation on microbial strains isolated from abandoned mine and marine samples, the chemical analysis and dereplication of a liquid cultured actinomycete strain KMC-004 (Figure 1) led to the isolation of two new angucyclic auinones, angumycinones A and B along with six known angucyclinone analogues. The structures of these compounds were established using extensive spectroscopic data analyses, including NMR, HRFABMS, UV, CD and X-ray crystallography [3]. In addition, two new tetracenedione derivatives, nocatriones A and B, were discovered from the culture broth of a marine actinomycete, *Nocardiopsis* sp. KMF-002, which was isolated from the tissue of an unidentified dark purple marine sponge (Figure 1). The structures, which are tetracenediones containing α-pyrone substituents, were determined to be 3,8,10,11-tetrahydroxy-2-(4-hydroxy-2-oxo-2*H*-pyran-6-yl)-1-methyltetracene-5,12-dione and 3,8,10,12-tetrahydroxy-2-(4-hydroxy-2-oxo-2*H*-pyran-6-yl)-1-methyltetracene-6,11-dione [4].

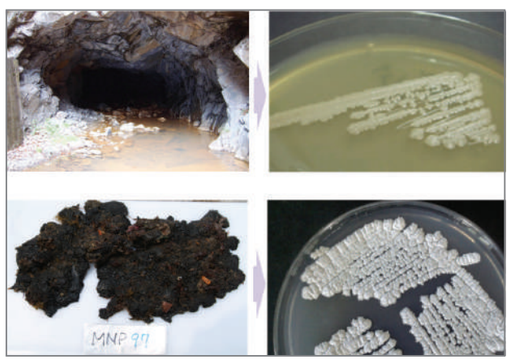

Figure 1. Bacterial strains isolated from an abandoned coal mine and a marine sponge.

Results

The isolation of actinomycetes strains from marine and mine samples

Acidic mine drainage samples (containing 209 ppm Fe,6.7 ppm Mn, 0.8 ppm Pb, 0.8 ppm Cu, pH 3.0) were collected from a horizontal pit situated at an elevation of 750 m in the abandoned Young-dong coal mine located in Gangneung. The acidic water samples were subsequently diluted with autoclaved distilled water and heated to 55°C for 6 min before the resulting suspension (100 μL) was inoculated onto several types of agar plates. The plates were incubated for 2 weeks at 25°C under aerobic conditions. A pure strain (KMC-004) was isolated from the YM agar medium. The strain KMC-004 was cultivated in YM liquid medium for 10 days at 25°C. The 16S rRNA gene sequence of the KMC004 strain was compared to the primary sequence information within the GenBank/EMBL/DDBJ nucleotide sequence database via the BLAST algorithm. The KMC004 strain was identified as a *Streptomyces* sp. based on a 98.3% 16S rDNA sequence similarity with that of a *Streptomyces chryseus* strain (EU841613).

The other actinomycete strain, KMF-002, was isolated from the tissue of an unidentified dark purple marine sponge, which is very similar to *Lotrochota baculifera*, collected by scuba diving at a depth of 20 m near Yeonggeumjeong, Sokcho, off the east coast of Korea. The strain KMF-002 was subjected to phylogenetic analyses based on the comparison of 16S rRNA sequences by BLAST to the National Center for Biotechnology Information (NCBI) database, demonstrating 100% identity with that of *Nocardiopsis* sp. A88Ydz-ZZ (EU257253, 1412/1412 bp).

New angucyclic quinones derived from the Streptomyces sp. KMC-004 strain from acidic coal mine drainage

The initial high-performance liquid chromatography mass spectrometry (HPLC/MS) analyses of the liquid cultured KMC-004 revealed six major constituents with characteristic quinone-like ultraviolet (UV) chromophores. To identify their molecular structures, the whole culture broth was extracted with ethyl acetate, and the extracts were subjected to gradient reverse-phase chromatography. The six major metabolites were identified as known angucyclinone structures [MM 47755 (**3**), (+)-rubiginone B_2 (**4**), (+)-ochromycinone (**5**), (+)-hatomarubigin A (**6**), (+)-rubiginone D_2 (**7**) and X-14881 E (**8**)] by comparing their spectroscopic data with previously reported spectroscopic data (Figure 2). Angucyclinones are characterized with an angular tetracyclic (benz[*a*]anthracene) carbon skeleton and are one of the many aromatic polyketides predominantly isolated from soil-derived *Streptomyces* spp. Most of the previously reported angucyclinone analogues have exhibited a broad range of biological properties, including cytotoxicity, antibacterial, and platelet aggregation inhibition properties. Angucyclic quinones have continuously become more attractive as a class of natural products due to their structural diversity, biomedical potential, and well-defined biosynthetic pathways. Therefore, we investigated the liquid culture media of KMC004 further to discover novel angucyclic quinones. Consequently, two highly oxygenated angucyclic quinones (Figure 2) were isolated as minor constituents (compounds **1** and **2**) from ethyl acetate extracts of *Streptomyces* sp. KMC-004 strain and named angumycinones A (**1**) and B (**2**).

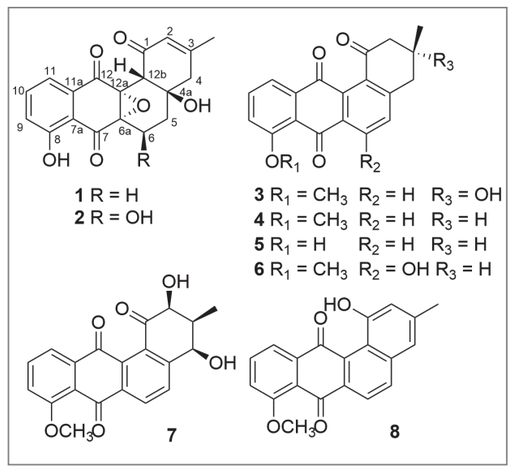

Figure 2. Structures of compounds **1**-**8**.

The relative configuration of chiral centers of angumycinone A (**1**) were determined by interpreting the 2D NOESY NMR spectral data and long range correlation between H-12b and H-5β in the ^1H-^1H COSY spectrum. These data allowed us to assign the relative configuration of H-12b and H-5β to be *cis*-configuration. The absolute configuration of **1** was deduced with direct method to be 4a*R*, 6a*S*, 12a*R*, and 12b*R* via single crystal X-ray diffraction analyses conducted with Mo Kα radiation, resulting in a refined Flack parameter value of 1.2(9) using 1553 Friedel pairs (Figure 3). The relative and absolute configurations of angumycinone B (**2**) were assigned by analyzing the NOESY correlations together with CD spectral data. The CD and NOESY spectra of angumycinone B (**2**) were very similar to that

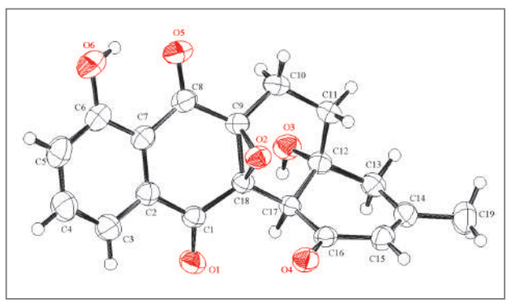

Figure 3. X-ray Oak Ridge Thermal Ellipsoid Plot (ORTEP) drawing of compound **1**.

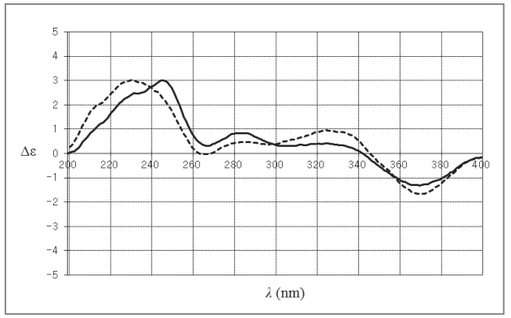

Figure 4. CD spectra of compounds **1** (---) and **2** (—).

of angumycinone A (**1**). The absolute configuration of the compound **2** was determined to be 4a*S*, 6*R*, 6a*S*, 12a*R*, and 12b*R* and was validated with the very similar CD spectra of compounds **1** and **2** (Figure 4)

Compounds **1**–**8** were tested for their antimicrobial activity against four Gram-positive bacteria, including *Micrococcus luteus* KCCM1548, *Enterococcus hirae* KCCM11768, *Bacillus subtilis* KCTC1021, and *Staphylococcus aureus* CCARM3089 (MRSA), in addition to three Gram-negative bacteria (*Salmonella typhimurium* KCCM11862, *Klebsiella pneumonia* KCCM35454, and *Escherichia coli* KCTC2593) and three fungal strains (*Aspergillus fumigatus* HIC6094, *Trichophyton rubrum* KCCM60443, and *Candida albicans* KCCM11282) using the previously described minimum inhibitory concentration (MIC) assay method. Ampicillin and amphotericin B were used as positive controls for pathogenic bacteria and fungi, respectively. Ampicillin exhibited antimicrobial activities against *M. luteus*, *E. hirae*, *B. subtilis*, MRSA, *S. typhimurium*, *K. pneumonia*, and *E. coli* with MIC values of 0.78, 0.78, 3.13, 12.5, 12.5, 12.5, and 6.25 μg/mL, respectively. The MIC values of amphotericin B were 1.56 μg/mL against each fungal strain (*A. fumigatus*, *T. rubrum*, and *C. albicans*). Angumycinone A (**1**) exhibited moderate antimicrobial activities against *M. luteus* and *E. hirae* (MIC values of 6.25 and 12.5 μg/mL, respectively); however, angumycinone B (**2**) was more active than **1** against the same strains (0.78 and 1.56 μg/mL, respectively). In addition, **2** demonstrated moderate activity against methicillin-resistant *S. aureus* (MRSA), displaying a MIC value of 12.5 μg/mL. The three known angucyclinone analogues, **3**, **5**, and **8**, also exhibited antimicrobial activity against *M. luteus* and *E. hirae*, while the other compounds (**4**, **6**, and **7**) were not active against any of the tested strains.

New tetracenediones derived from the Nocardiopsis sp. KMF-002 strain from a dark purple marine sponge

The KMF-002 was cultivated in A1 liquid medium supplemented with sea salt at 27°C for 15 days at which point the culture broth was extracted with EtOAc. Tetracenedione compounds, nocatriones A (**9**) and B (**10**), were purified from the EtOAc extract using a combination of diverse chromatographic techniques. The structures of **9** and **10** (Figure 5) were elucidated using spectroscopic methods, including 1D and 2D NMR techniques (Figure 6). The structure of nocatrione A (**9**), which contains an α-pyrone attached to the C-2 position of a tetracene-5,12-

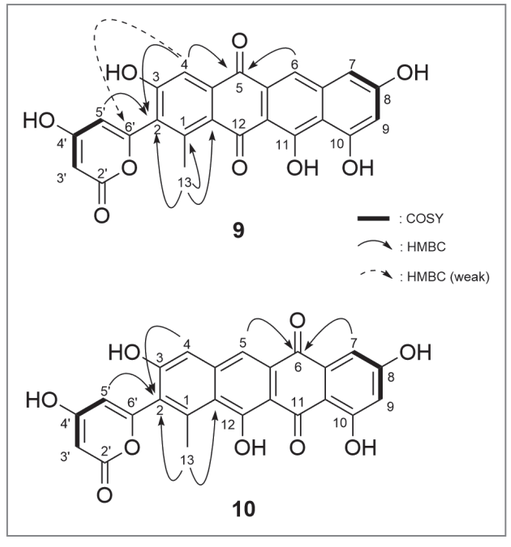

Figure 5. Structures and the key 2D NMR correlations of compounds **9** and **10**.

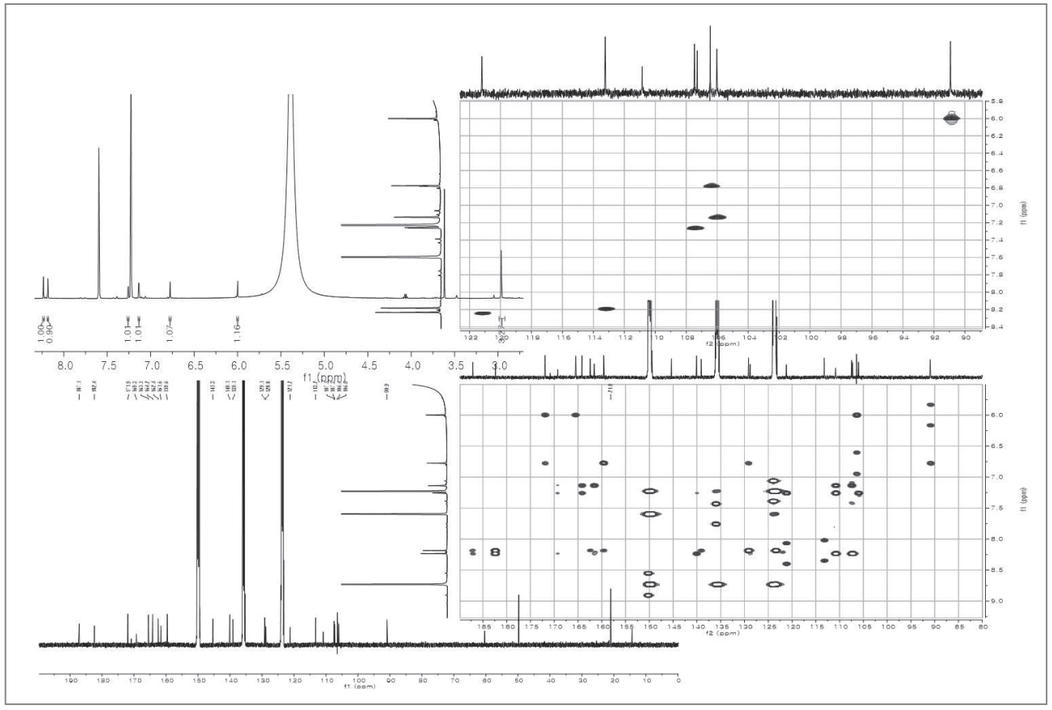

Figure 6. ^{1}H, ^{13}C, gHSQC, and gHMBC NMR spectra of the compound **9**.

dione, was determined to be 3,8,10,11-tetrahydroxy-2-(4-hydroxy-2-oxo-2*H*-pyran-6-yl)-1-methyltetracene-5,12-dione. In addition, the 1D and 2D NMR data for nocatrion B (**10**) displayed signals due to an α-pyrone unit attached to the C-2 position of the tetracene-6,11-dione moiety. The point of connection between the α-pyrone and tetracenedione substructures was confirmed by analyzing the key HMBC NMR correlations (Figure 5). Therefore, the structure of nocatrione B (**10**) was determined to be 3,8,10,12-tetrahydroxy-2-(4-hydroxy-2-oxo-2*H*-pyran-6-yl)-1-methyltetracene-6,11-dione.

To investigate the photoprotective effects of compounds **9** and **10** on cultured human dermal fibroblasts (MCTT MC1233), we first examined MMP-1 secretion and cell viability under UVB non-irradiated normal conditions. MMP-1, a member of MMPs and interstitial collagenase, initiates the degradation of type I and III collagens. Exposure to UV increases MMP-1 and reduces type I procollagen levels, and that finally induces skin photoaging [5]. We examined the effects of compounds **9** and **10** on UVB-irradiated normal human dermal fibroblasts (UV-NHDFs). When the NHDFs were exposed to UVB at 144 mJ/cm^2, cell viability decreased approximately 17% and MMP-1 expression increased approximately fourfold compared to non-irradiated cells. However, treatment of UV-NHDFs with compounds **9** and **10** caused a decrease of MMP-1 expression in a concentration-dependent manner with no cytotoxicity. At 10 μM concentration, the compound **9** significantly down-regulated MMP-1 production (65% reduction), while

the compound **10** modestly down-regulated MMP-1 production (18% reduction) compared to that of untreated UV-NHDFs (control cells). We also checked the effects of compounds **9** and **10** on another NHDF cell line (ScienCell 2320) using the same method. The data revealed that **1** and **2** significantly down-regulated MMP-1 production (99% and 91% reduction, respectively) compared to that of untreated UV-NHDFs at 10 μM concentration.

Conclusion

The angumycinones (**1** and **2**) represent highly oxygenated angucyclic quinones; this scaffold is characterized by the presence of an epoxide group situated between C-6a and C-12a. Only nine natural 6a,12a-epoxybenz[a]anthracene derivatives have been reported so far from soil-based *Streptomyces* species. Of these nine structures, angumycinone A (**1**) is the most similar in structure to grecocycline A aglycon, which features a hydroxyl group positioned at C-12b. One critical difference in structure between **1** and grecocycline A aglycon is the absolute configurations of the stereocenters at C-12b and C-4a. A hydroxyl group at C-6, similar to the one in angumycinone B (**2**), can also be observed in simocyclinone D4 aglycon, which contains additional hydroxyl groups at C-12b and C-7. However, the absolute configuration of these molecules has never been reported. All isolates from the strain KMC-004 were tested for antimicrobial activity against ten pathogenic microbial or fungal strains. Angumycinone B (**2**) exhibited antimicrobial activity against *Micrococcus luteus*, *Enterococcus hirae*, and methicillin-resistant *Staphylococcus aureus* (MRSA) with minimum inhibitory concentration values of 0.78, 1.56, and 12.5 μg/mL, respectively.

Numerous compounds containing a tetracene moiety have been isolated from *Streptomyces* species. However, compounds containing a tetracenedione connected to an α-pyrone moiety by a C-C bond have not been reported. Moreover, compounds containing a tetracene quinone moiety have never been isolated from *Nocardiopsis* sp. The biological activity data show that nocatrione A (**9**) exhibits a significant protective effect against UVB-irradiation in both NHDF cell lines, whereas nocatrione B (**10**) has a protective effect against UVB in a specific NHDF cell line. Therefore, nocatriones A and B from a marine-derived *Nocardiopsis* sp. may provide UVB photoprotection by adjusting the activity of matrix metalloproteinase. The discovery of new angumycinones and nocatriones from actinomycetes associated with unique environmental conditions demonstrates that exploration of new microbial secondary metabolites via a series of chemical analysis can be an efficient approach to obtain chemical diversity in microbial natural products.

Note

This article and images are drawn from "Nocatriones A and B, photoprotective tetracenediones from a marine-derived *Nocardiopsis* sp." in the *Journal of Natural Products*, Vol. 77, pp. 2326-2330 and "Angumycinones A and B, two new angucyclic quinones from Streptomyces sp. KMC004 isolated from acidic mine drainage" in *Tetrahedron Letters*, Vol. 55, pp. 63-66.

References

[1] (a) Takagi M, Shin-ya K. *J. Antibiot.* 2012; 65: 443-447. (b) Olano C, Méndez C, Salas JA. *Mar. Drugs.* 2009; 7: 210-248. (c) Oh D-C, Scott JJ, Currie CR, Clardy J. *Org. Lett.* 2009; 11: 633-636. (d) Header S, Wirth R, Herz H, Spiteller D. *Proc. Natl. Acad. Sci. USA.* 2009; 106: 4742-4746. (e) Kroiss J, Kaltenpoth M, Schneider B, Schwinger M-G, Hertweck C, Maddula RK, Strohm E, Svatoš A. *Nat. Chem. Biol.* 2010; 6: 261-263.

[2] Kwon HC, Kauffman CA, Jensen PR, Fenical W. *J. Org. Chem.* 2009; 74: 675-684.

[3] Park HB, Lee JK, Lee KR, Kwon HC. *Tetrahedron Lett.* 2014; 55: 63-66.

[4] Kim MC, Hwang EH, Kim T, Ham J, Kim SY, Kwon HC. *J. Nat. Prod.* 2014; 77: 2326-2330.

[5] Fisher GJ, Kang S, Varani J, Bata-Csorgo Z, Wan Y, Datta S, Voorhees JJ. *Arch. Dermatol.* 2002; 138: 1462-1470.

[**Technical Review**]

Black Phosphorus, a Novel Material with High Carrier Mobility and Device Functionality

Junhong Na
Center for Opto-Electronic Materials and Devices
mozildori@kist.re.kr

Won Kook Choi
Materials and Life Science Research Division
wkchoi@kist.re.kr

Yong-Won Song
Center for Opto-Electronic Materials and Devices
ysong@kist.re.kr

Historical overview of 2-dimensional van der Waals materials before the introduction of black phosphorus

The silicon-based semiconductor industry is facing significant challenges as a result of the physical limitations of silicon material when used in smaller devices with new demands for greater flexibility and transparency. As a result, researchers are actively seeking new materials to meet the challenge [1]. Graphene, discovered in 2004 [2], has emerged as a promising alternative to silicon for electronic and optoelectronic applications due to its superior carrier mobility, thermal conductivity, mechanical strength, flexibility, and transparency [3]. Its atomically thin body thickness and perfect two-dimensional (2D) nanostructure have prompted extensive work by both experimental and theoretical researchers. Unfortunately, the zero band gap of graphene yields a very low on/off current ratio which is not appropriate for logic device applications [4]. Therefore, in addition to graphene, other 2D layered materials that have intralayer (within layers) covalent bonding and interlayer (between layers) van der Waals (vdW) interactions, namely vdW materials, have moved into the spotlight [5, 6].

Transition-metal dichalcogenides (TMDs), exemplary vdW materials which include molybdenum disulfide (MoS_2) and tungsten diselenide (WSe_2), have a layered structure which is similar to graphene, yet also a definite band gap, a significant difference from graphene [5]. A paper published in 2011 triggered the explosion of interest in 2D TMDs. This research reported that monolayer MoS_2 field-effect transistors (FETs) exhibited a high carrier mobility of ~217 $cm^2\ V^{-1}\ s^{-1}$ at room temperature, high on/off current ratio of ~10^8 owing to the suppression of Coulomb scattering in a high-*k* environment, and the existence of a reasonable band gap (~1.8 eV for monolayer and ~1.2 eV for multilayer MoS_2) [7]. These features of MoS_2 were enough to compensate for the drawbacks of both silicon and graphene. However, this carrier mobility value of the monolayer MoS_2 was later corrected down to ~15 $cm^2\ V^{-1}\ s^{-1}$ by properly calculating the gate capacitance in a dual-gate configuration [8, 9]. Nevertheless, various kinds of TMDs produced from the combination of transition-metal and chalcogen elements can give us various material properties, such as metallic, semiconducting, superconducting, as well as topological insulator material, and as a result, continue to attract researchers [5]. In addition, the mechanism of the high-*k* effect on vdW layered materials remains unclear; thus, relevant studies must continue in this area.

Approaches for enhancing device performance and the emergence of black phosphorus as a channel material

Studies to enhance the carrier mobility values of MoS_2 transistors in terms of intrinsic or extrinsic treatment effects on MoS_2 are ongoing [10]. The literature on intrinsic treatments that alter the structural defects of MoS_2, such as point defects and dislocations, is so far very limited. Some research activities regarding the plasma treatment effects on MoS_2 have been reported [11, 12], but further work remains to obtain high-quality MoS_2 and other vdW layered materials. In contrast to the limited investigations into enhancement of intrinsic effects, extrinsic treatment approaches that improve the interface qualities between MoS_2 and the metal electrodes or gate dielectrics have been thoroughly studied. Alternative metals to form an interface with MoS_2 and serve as electrodes for devices were considered to decrease the effective Schottky barrier height and reduce the contact resistance, which can be explained in terms of the work function variation and Fermi level energy pinning [13, 14]. For example, scandium metal-contacted MoS_2 transistors have recorded high carrier mobility values of ~184 $cm^2\ V^{-1}\ s^{-1}$ [13]. In addition, enhancement in the interface quality between MoS_2 and the gate dielectric can also be regarded as one of the extrinsic treatment approaches to increase the carrier mobility in transistors; therefore, various gate dielectrics such as poly(methyl methacrylate) (PMMA) [15], Al_2O_3 [16], and boron nitride [17], have been applied to MoS_2 devices. In various dielectric environments, for example, MoS_2 transistors encapsulated and passivated with PMMA [15] and Al_2O_3 [13] showed high carrier mobility values of ~470 and ~700 $cm^2\ V^{-1}\ s^{-1}$ at room temperature, respectively. Nevertheless, these superior carrier mobility values of MoS_2 devices must be confirmed through further study to ensure reliability.

In the absence of applicable intrinsic or extrinsic treatment approaches for MoS_2, black phosphorus (BP), an allotrope of phosphorus and another vdW layered material, has been demonstrated as a channel material that can achieve high-performance FETs with a carrier mobility value of ~1000 $cm^2\ V^{-1}\ s^{-1}$ at room temperature, even in the form of few-layer BP transistors [6]. According to results that reported carrier mobility values on the order of 10^2 $cm^2\ V^{-1}\ s^{-1}$ [18, 19], BP materials can somewhat retain their bulk carrier mobility values in a few-layer form, in contrast to other TMDs. Liu et al. [20] claim that BP is an allotrope of phosphorus which is a mono-elemental vdW material, unlike TMDs which are hetero-elemental vdW materials; thus, BP can be electronically less sensitive to defects than TMDs. Also, the reasonable on/off current ratio of ~10^5 demonstrated in few-layer BP FETs can be achieved by proper thickness selection of the flakes. From this perspective, few-layer BPs are considered a promising channel material for high-performance electronic device applications. A surge in

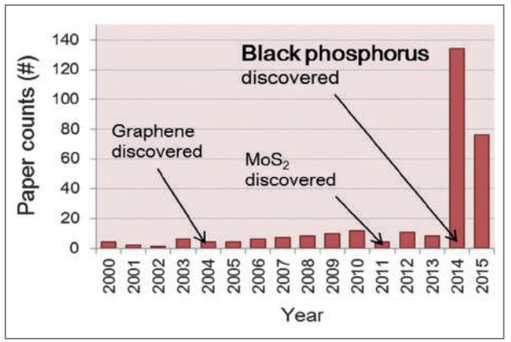

Figure 1. The annual number of published items found using the search word: "black phosphorus" or "phosphorene." The data was extracted from the Thomson Reuters *Web of Science* website (webofknowledge.com) on April 11, 2015.

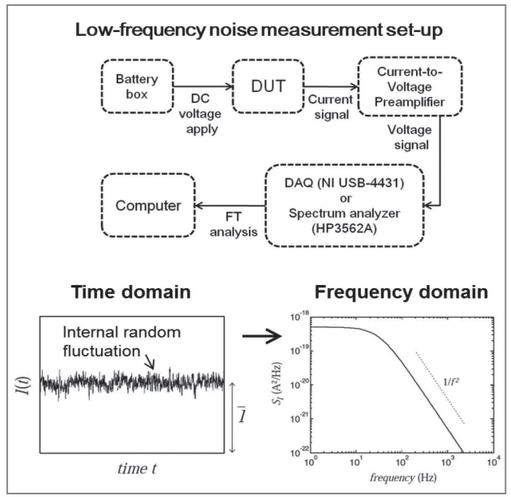

Figure 2. (Top) Simple diagram representing low-frequency noise measurement system. (Below) Different expressions of the noise in time and frequency domains.

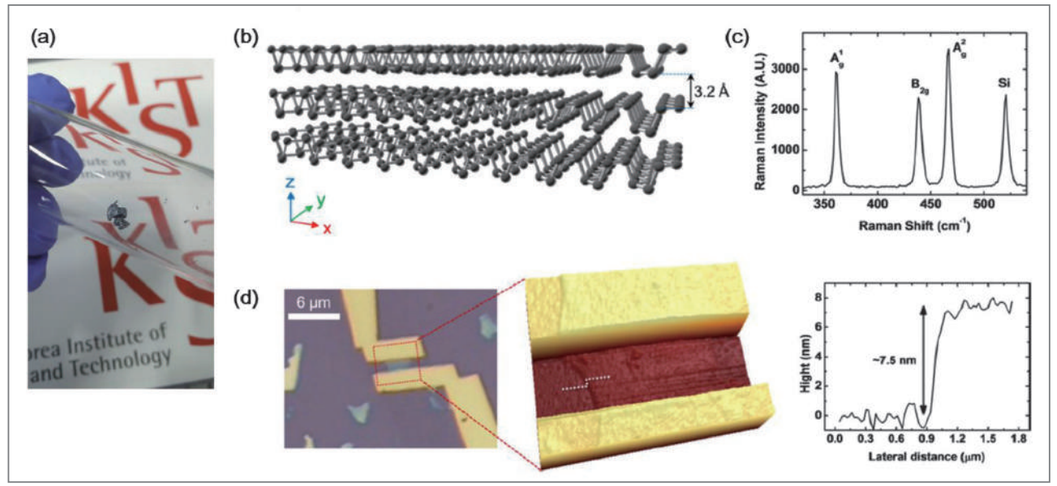

Figure 3. (a) Photograph of bulk black phosphorus. (b) Schematic image of a few-layer BP. (c) Raman spectrum of a few-layer BP placed on a SiO_2/Si substrate. (d) (Left) Optical image of a metal-contacted few-layer BP. (Center) Three-dimensional image of a few-layer BP with Au contact metals measured by AFM. (Right) Thickness of the few-layer BP was measured to be ~7.5 nm.

research related to black phosphorus was observed in 2014, as shown in Figure 1. To further increase device performance and improve device analysis on few-layer BP FETs, it will be critical to conduct research on the effects of high-*k* layer on few-layer BPs relative to other vdW layered materials.

Role of low-frequency noise characterization in BP

The low-frequency noise (LFN) characterization method has been used as a tool for diagnosing carrier transport behavior and interface quality between a semiconductor and an insulator in conventional metal–oxide–semiconductor FETs (MOSFETs) [21, 22]. Simple LFN measurement set-up and expression of the noise in time and frequency domain are expressed in Figure 2. Other methods of obtaining interface quality information on devices, namely, capacitance–voltage measurement and deep-level transient spectroscopy, are limited by the area size of the interface; hence, measurement using nanoscale devices becomes difficult [22]. Fortunately, LFN measurement can be applied regardless of the area size of the interface, which is one of the advantages of this method in nanodevice analysis. Because downscaling of the device can be performed aggressively, the increase in the signal-to-noise ratio emphasizes the importance of LFN characterizations [23]. Moreover, reduction of the noise level in devices can affect device performance; therefore noise-level reduction methods in vdW materials have to be developed and analyzed.

To the best of our knowledge, our work on the LFN characteristics of few-layer BP FETs is the first report on this subject. Here, we also propose a method to reduce current fluctuations using an Al_2O_3-passivation layer.

Fabrication method of few-layer BP FETs

In our work, BP was investigated as a layered material in which each layer was stacked with vdW interactions along the *z*-direction, as shown in Figures 3a and 3b. The interlayer distance between the closest individual layers was estimated to be ~0.32 nm. A few-layer BP can also be exfoliated from bulk BP and placed onto a Si/SiO_2 substrate, which, in this study, consisted of a highly p^{++} Si and a thermally oxidized 300-nm-thick SiO_2 layer. Representative Raman spectra (532 nm, Nd:Yag Laser) of a few-layer BP on the Si/SiO_2 substrate are shown in Figure 3c, and the Raman peak locations indicate that the material was indeed BP [24]. To characterize the electrical properties of few-layer BPs, an Au-only metal (~100-nm thick) was used as a source and drain electrode using subsequent electron beam lithography and thermal evaporation. The optical image of the as-fabricated few-layer BP device is shown in Figure 3d (left image). To determine the thickness of the few-layer BP, atomic force microscopy (AFM) was used, and the three-dimensional image is shown in Figure 3d (center image). The thickness of the few-layer BP was confirmed to be ~7.5 nm, as shown in Figure 3d (right image). Thermal annealing and Al_2O_3 deposition were sequentially applied to the devices, and static and LFN measurements were performed between process intervals.

DC characterizations of few-layer BP FETs

Figure 4b shows the typical output characteristics of a few-layer BP FET measured with the microprobe tips shown in Figure 4a. The transfer characteristics of the few-layer BP FET is shown in Figure 4c. As shown by the graph in Figure 4c, p-branch enhanced ambipolar characteristics appear in most of the thermally annealed few-layer BP FETs.

Figure 4d shows that the quantitative changes in the subthreshold slope (*SS*) and hysteresis values resulting from the thermal annealing and Al_2O_3-passivation effects on the device performance of the few-layer BP FETs are reliable. After the thermal annealing, the *SS* values were significantly reduced, but the hysteresis values were only

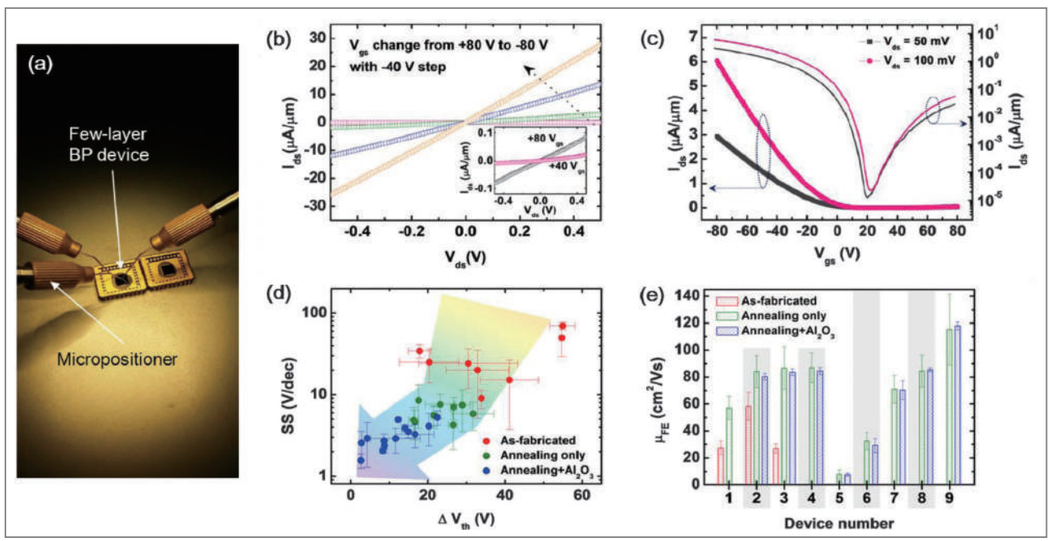

Figure 4. (a) Photograph of measuring electrical properties with probe tips. (b) Output and (c) transfer characteristics of the few-layer BP FET. (d) Quantitative *SS* and ΔV_{th} data for three cases of few-layer BP FETs: "As-fabricated," "Annealing only," and "Annealing + Al_2O_3." (e) μ_{FE} changes in three steps for each few-layer BP FET.

slightly reduced. The removal of polymer residues near the BP layers [25] and the improvement in the contact properties [26] through thermal annealing can affect the reduction in the *SS* values. Thermal annealing and electrical measurement in vacuum were not the *in situ* processes applied in this study; thus, the hysteresis values could remain if the dominant hysteresis sources are adsorbates such as water and/or oxygen molecules near the BP layers and/or the silanol groups on the SiO_2 surface [27, 28]. Through Al_2O_3 passivation by the atomic layer deposition (ALD) process, the *SS* and hysteresis values were evidently reduced. The remaining water and/or oxygen molecules near the BP layers can be effectively removed during the preheating step of the ALD process (~220°C) [27, 28]. Further, the sequential chemisorptions of trimethylaluminum (TMA) precursor to the hydroxyl groups on the SiO_2 and the surface oxidation layer of the BP can also reduce the water and/or oxygen molecules and hydroxyl groups that probably affected the *SS* and hysteresis values [29]. This tendency of reduced *SS* and hysteresis values by the Al_2O_3 deposition suggests that the Al_2O_3 passivation can be a positive method of realizing high performance few-layer BP FETs.

LFN characterizations of few-layer BP FETs

Figure 5a shows the drain current spectral density (S_I) as a function of the frequency at different gate voltages obtained from the LFN measurement of the thermally annealed few-layer BP FET. These data were Fourier transformed to the frequency range on the basis of the time-domain drain current fluctuation of the device at different gate voltages, as shown in Figure 5b.

Two types of LFN models are widely accepted for describing the noise characteristics in conventional silicon MOSFETs: carrier number fluctuation (CNF) and Hooge mobility fluctuation (HMF) models [21, 22]. The CNF model suggests that current fluctuations arise from the change in the charge carrier density due to the charge trapping/detrapping phenomena at the trap sites near the channel–insulator interface. The HMF model describes that the change in the carrier mobility resulting from the variation of the scattering cross section induces current fluctuations. To figure out which type of LFN model is dominant and best expresses the carrier transport behavior in a few-layer BP FET, the normalized drain current spectral density (S_I/I_{ds}^2) as a function of the drain current is shown in Figure 5c. In the CNF model, the normalized drain current spectral density can be expressed as:

$$\frac{S_I}{I_{ds}^{\ 2}} = \left(\frac{g_m}{I_{ds}}\right)^2 S_{Vfb} \qquad (1)$$

where g_m is the gate transconductance and S_{Vfb} is the flat band voltage spectral density that can also be expressed as:

$$S_{Vfb} = \frac{q^2 k_B T N_{it}}{WLC_{ox}^{\ 2} f} \qquad (2)$$

where *W* and *L* are the width and length of the channel, respectively, and N_{it} is the interface trap density [21]. Using this CNF model, we obtained the best-fit result for the thermally annealed few-layer BP FET, as shown in Figure 6c.

After the Al_2O_3 passivation on the thermally annealed few-layer BP FETs, S_I/I_{ds}, which is also considered as a noise level, was reduced over the entire device operation regime, as shown in Figure 5d. According to the reduced *SS* and hysteresis values shown in Figure 4, we expected that the removal of the remaining adsorbates and hydroxyl group near the BP layer could affect the reduction in noise level resulting from the suppression of the charge trapping/detrapping process. We should note that Al_2O_3 passivation is one way of reducing the noise level in few-layer BP FETs. Moreover, by dealing with the device shown in Figure 5, the N_{it} values obtained for the thermally annealed and Al_2O_3-passivated few-layer BP FETs were ~1.2 × 10^{12} and ~1.5 × 10^{11} cm^{-2} eV^{-1}, respectively.

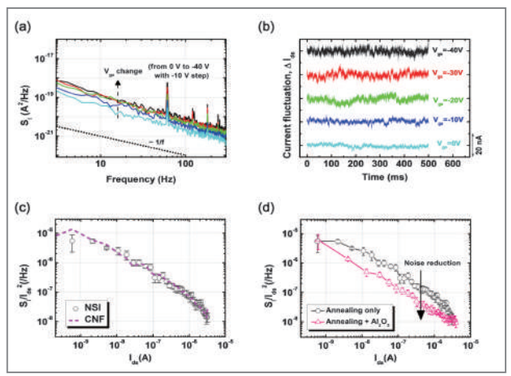

Figure 5. LFN characteristics of the few-layer BP FET. (a) Drain current spectral density as a function of frequency for the thermally annealed few-layer BP FET. (b) Current fluctuation in the time domain at the same gate voltage values as those in (a). (c) Mean normalized drain current spectral density (NSI). The corresponding CNF model is fitted to the NSI data. (d) Noise reduction due to Al_2O_3 passivation represented by the mean normalized drain spectral density as a function of the drain current.

Degradation and passivation effects in few-layer BP FETs

BP flakes are well known to degrade when stored in ambient air without any passivation layers [18]. This phenomenon has not been precisely investigated yet, but surface reactions with gas molecules in ambient air has been considered as a dominant factor in the degradation. To further verify the ALD Al_2O_3-passivation effect, the few-layer BP flakes passivated with an Al_2O_3 layer were stored in ambient air at room temperature for two months. The optical images and Raman spectra shown in Figure 6 confirm that the Al_2O_3 layer can effectively block the surface reactions between the BP and gas molecules in ambient air, resulting in the passivation effect on the few-layer BP flakes. This result suggests that an ALD Al_2O_3 layer can be a promising candidate in passivating few-layer BP flakes and enhancing device performance.

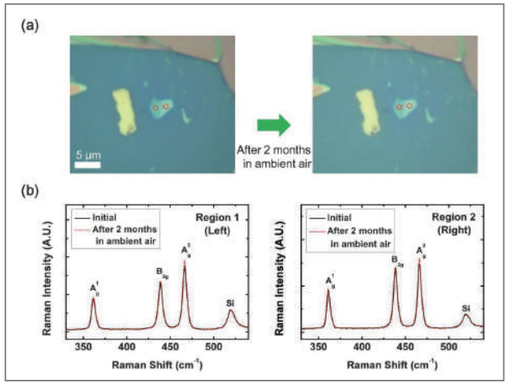

Figure 6. Al_2O_3-passivation effect on the Raman spectra of the few-layer BP. (a) Optical images of (right) few-layer BP flakes passivated with an Al_2O_3 layer and (left) the same flakes stored in ambient air after two months. (b) Raman spectra corresponding to the same few-layer BP flakes indicated by the two red and dashed circles (left and right) in (a).

Conclusion

In summary, current fluctuation, considered as a noise level in devices, was reduced throughout the device operation regime in few-layer BP FETs as a result of Al_2O_3 passivation. Our static analysis also confirmed the positive effects of Al_2O_3 passivation on the tested devices by qualitatively and quantitatively monitoring the device parameters such as hysteresis, *SS* and D_{it}. Moreover, through a separate analysis of the thermal annealing and Al_2O_3-passivation effects, the static and LFN characteristics of few-layer BP FETs were verified to be more reliable. To analyze the LFN characteristics, we introduced a CNF model which suggests that current fluctuation is induced by the charge carrier trapping/detrapping process in the trap sites near the gate insulator. By comparing the D_{it} and N_{it} values obtained from the static and LFN analyses, respectively, we observed the same trend in which the interface trap density values decreased after Al_2O_3 passivation. Finally, we confirmed through identical Raman spectra that Al_2O_3 passivation plays a major role in conserving few-layer BP flakes in ambient air for two months. Our study can be applied in understanding the role of high-*k* dielectric in the performance of few-layer BP FETs and in realizing high-performance passivated few-layer BP FETs.

Note

This article and images are drawn from “Few-layer black phosphorus field-effect transistors with reduced current fluctuation” in *ACS Nano*, Vol. 8 (11), pp.11753-11762.

References

[1] Liu CW, Östling M, Hannon JB. *MRS Bulletin* 2014; 39: 658-662.
[2] Novoselov KS, Geim AK, Morozov SV, Jiang D, Zhang Y, Dubonos SV, Grigorieva IV, Firsov AA. *Science* 2004; 306: 666-669.
[3] Yang H, Heo J, Park S, Song HJ, Seo DH, Byun KE, Kim P, Yoo I, Chung HJ, Kim K. *Science* 2012; 336: 1140-1143.
[4] Schwierz F. *Proc IEEE.* 2013; 101: 1567-1584.
[5] Chhowalla M, Shin HS, Eda G, Li LJ, Loh KP, Zhang H. *Nat Chem.* 2013; 5: 263-275.
[6] Li L, Yu Y, Ye GJ, Ge Q, Ou X, Wu H, Feng D, Chen XH, Zhang Y. *Nat Nanotechnol.* 2014; 9: 372-377.
[7] Radisavljevic B, Radenovic A, Brivio J, Giacometti V, Kis A. *Nat Nanotechnol.* 2011; 6: 147-150.
[8] Fuhrer MS, Hone J. *Nat Nanotechnol.* 2013; 8: 146-147.
[9] Radisavljevic B, Kis A. *Nat Nanotechnol.* 2013; 8: 147-148.
[10] Jung Y, Shen J, Cha J. *Nano Convergence* 2014; 1: 18-8.
[11] Chen M, Nam H, Wi S, Priessnitz G, Gunawan IM, Liang X. *ACS Nano* 2014; 8: 4023-4032.
[12] Chen M, Nam H, Wi S, Ji L, Ren X, Bian L, Lu S, Liang X. *Appl Phys Lett.* 2013; 103: 142110-4.
[13] Das S, Chen HY, Penumatcha AV, Appenzeller J. *Nano Lett.* 2012; 13: 100-105.
[14] Gong C, Colombo L, Wallace RM, Cho K. *Nano Lett.* 2014; 14: 1714-1720.
[15] Bao W, Cai X, Kim D, Sridhara K, Fuhrer MS. *Appl Phys Lett.* 2013; 102: 042104-4.
[16] Kim S, Konar A, Hwang WS, Lee JH, Lee J, Yang J, Jung C, Kim H, Yoo JB, Choi JY, et al. *Nat Commun.* 2012; 3: 1011-7.
[17] Chan MY, Komatsu K, Li S, Xu Y, Darmawan P, Kuramochi H, Shu N, Ferreira AA, Watanabe K, Taniguchi T, et al. *Nanoscale* 2013; 5: 9572-9576.
[18] Koenig SP, Doganov RA, Schmidt H, Castro Neto AH, Özyilmaz B. *Appl Phys Lett.* 2014; 104: 103106-4.
[19] Liu H, Neal AT, Zhu Z, Luo Z, Xu X, Tománek D, Ye PD. *ACS Nano* 2014; 8: 4033-4041.
[20] Liu Y, Xu F, Zhang Z, Penev ES, Yakobson BI. *Nano Lett.* 2014.
[21] Ghibaudo G, Roux O, Nguyen-Duc C, Balestra F, Brini J. *Phys Status Solidi A.* 1991; 124: 571-581.
[22] von Haartman M, Östling M. *Low-Frequency Noise in Advanced MOS Devices.* Springer: 2007.
[23] Ghibaudo G, Boutchacha T. *Microelectronics Reliability* 2002; 42: 573-582.
[24] Morita A. *Applied Physics A.* 1986; 39: 227-242.
[25] Kumar K, Kim YS, Yang EH. *Carbon* 2013; 65: 35-45.
[26] Woo Y, Duesberg GS, Roth S. *Nanotechnology* 2007; 18: 095203-7.
[27] Zhuravlev LT. *Colloids Surf A.* 2000; 173: 1-38.
[28] Zhang W, Jie J, Luo L, Yuan G, He Z, Yao Z, Chen Z, Lee CS, Zhang W, Lee ST. *Appl Phys Lett.* 2008; 93: 183111-3.
[29] Helbling T, Hierold C, Roman C, Durrer L, Mattmann M, Bright VM. *Nanotechnology* 2009; 20: 434010-10.

[Feature Articles]

Giant Electrode Effect on Tunneling Electroresistance in Ferroelectric Tunnel Junctions

Doo Seok Jeong
Center for Electronic Materials
dsjeong@kist.re.kr

Introduction

We are living in the era of digital technology, which has had remarkable staying power. Although initiated many decades ago, the digital era is still alive and well due to continuous advances in digital technology. This has surprised many since the technology would seem to have obvious physical limits. Interestingly however, groundbreaking technologies have been developed just as current ones are unable to meet new demands, thus prolonging the era by years. However, even digital optimists admit that advances in digital technology tend to be difficult as well as costly, with technical maturity still a factor. In an attempt to overcome technical obstacles, a new research trend has emerged which adopts various physical phenomena that exhibit two distinctive physical variables for binary numbers in the digital framework.

One of these physical variables is ferroelectricity in which spontaneous electric polarization remains despite the lack of an external electric field [1]. More importantly, the electric polarization is flipped upon the application of the opposite electric field and the new polarization remains. Given this spontaneous polarization feature of ferroelectrics – materials featuring ferroelectricity – some attempts have been made to utilize the feature in nonvolatile memory, so-called ferroelectric random access memory (FRAM). Despite these efforts, the inherent difficulty in integrating capacitance-based memories has hindered the utilization of the technology. One possible workaround solution to this difficulty is the use of ferroelectrics in resistors, rather than capacitors, which does not bring about serious scaling-down issues [1]. In other words, a resistance-based memory based on ferroelectrics may be an alternative to FRAM [1-4].

Ferroic nanostructures comprising materials such as ferromagnets and ferroelectrics and involving components with different levels of conductivity (metals, semiconductors, insulators) represent an important class of heterostructures that are very promising for applications in advanced electronic devices. Remarkably, in layered heterostructures, where insulating layers have the thickness of only a few nanometers, quantum mechanical electron tunneling becomes the dominant conduction mechanism. A prominent example of such *quantum nanostructures* is a magnetic tunnel junction (MTJ), where two ferromagnetic electrodes are separated by an ultrathin insulating layer acting as a potential barrier. Another promising quantum nanostructure has the form of a ferroelectric tunnel junction (FTJ), where the tunnel barrier is made of a ferroelectric material.

The choice of electrode materials seems to have a pronounced influence on the TER effect due to different screening and chemical properties at the interface. Therefore, it is essential to examine the impact of different electrode materials on the TER characteristics of FTJs. Furthermore, the TER effect associated with ferroelectric switching is inferred from the occurrence of resistance switching at voltages corresponding to the coercive fields of the ferroelectric tunnel barrier.

In the work described in this article, we fabricated asymmetric FTJs comprising $La_{0.7}Sr_{0.3}MnO_3$ bottom electrodes (BEs), 3 nm thick $BaTiO_3$ tunnel barriers, and two different top electrodes (Au and Cu TEs). The current-voltage (*I-V*) characteristics of these FTJs were measured by applying a voltage to the micron-sized TEs using a conductive atomic force microscope (C-AFM). The ferroelectric behavior of the $BaTiO_3$ barrier was identified using a piezoresponse force microscopy (PFM) technique. After analyzing the complete set of experimental data theoretically, we propose an explanation for the observed giant electrode effect on the TER of the asymmetric FTJs.

Results and discussion

The microstructure of the fabricated FTJ with Cu TE is shown in Figure 1a. The BTO was epitaxially grown on the LSMO BE and the Cu TE hardly formed an interfacial oxide phase such as CuOx as justified by the electron energy loss spectroscopy spectra in Figure 1b.

High-quality epitaxial $La_{0.7}Sr_{0.3}MnO_3/BaTiO_3$ (LSMO/BTO) heterostructures used in this study were deposited on a (001)-oriented single-crystalline $SrTiO_3$ (STO) substrate. Atomic force microscopy measurements on the LSMO/BTO heterostructures revealed atomically flat terraces separated by steps of approximately 0.4 nm height (a single unit cell), which is similar to those of the STO substrate (Figure 2e). The x-ray diffraction (XRD) patterns identified that their crystallographic planes were parallel to the (001) planes of STO (see Figure 1a), i.e., the BTO tetragonal *c* axis was perpendicular to

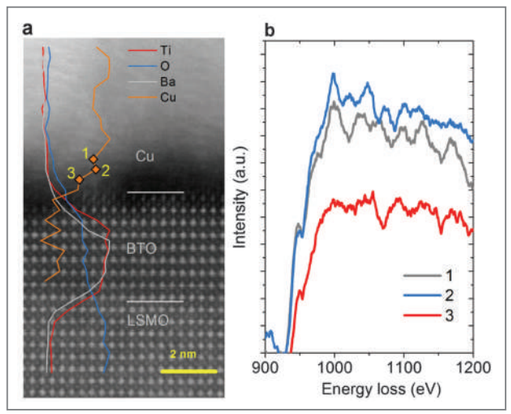

Figure 1. (a) Cross-sectional scanning tunneling electron microscopy image of the LSMO/BTO/Cu FTJ and distributional profiles of Ti, O, Ba, and Cu across the junction. (b) Electron energy loss spectroscopy spectra of Cu in the vicinity of the BTO/Cu interface at three locations, numbered 1, 2, and 3 in panel (a).

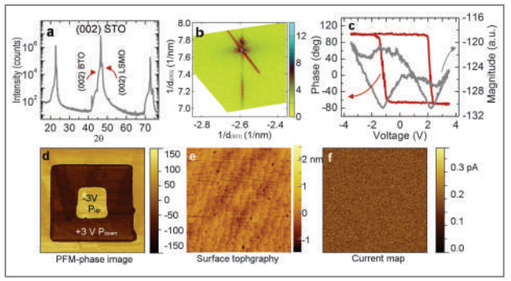

Figure 2. (a) Hysteretic behavior of the PFM phase and magnitude signals plotted as a function of the bias voltage applied to the Au TE of the LSMO/BTO/Au FTJ. (b) A typical *I-V* curve and (c) the corresponding *R-V* behavior (CC denotes compliance current). (d) Bias dependence of TER derived from the *R-V* characteristics in the shadowed voltage range. All measurements were performed at room temperature using C-AFM.

the substrate surface. In order to assess the substrate-induced strains and to evaluate the lattice parameters of the heterostructures, x-ray reciprocal space mapping measurement was performed around the asymmetric (103) Bragg reflection. As can be seen from the reciprocal space map shown in Figure 2b, the LSMO/BTO heterostructures were fully strained in a compressive manner, ensuring a high polarization in the BTO film. The in-plane and perpendicular-to-plane lattice constants of the ultrathin BTO film were found to be 3.905 Å and 4.134 Å, respectively.

Ferroelectric properties of the BTO film were investigated at room temperature using the PFM. As shown in Figure 2c, a clear hysteretic behavior was observed in both phase (~180^0 difference) and magnitude signals, acquired at a resonance frequency of the cantilever (542 kHz) as a function of a voltage *V* applied to the C-AFM tip (the LSMO BE was grounded). These results clearly show ferroelectric switching behavior of the 3 nm thick BTO film. The ferroelectric switching (coercive) voltages creating the downward polarization $P^{\downarrow}$ (directed towards the LSMO BE) and the upward polarization $P^{\uparrow}$ (directed towards the C-AFM tip) were found to be about +2.5 V and –1.2 V, respectively.

Applying a constant voltage $V = \pm 3$ V to the tip and scanning the film surface, we poled different regions of the BTO film. Figure 2d shows a PFM phase image of the poled film, acquired at a frequency close to the cantilever resonance frequency. Since the ultrathin BTO film was subjected to a high in-plane biaxial compressive strain of about 2%, ensuring perpendicular-to-plane polarization orientations, a large phase contrast of ~180^0 between the square domains written at +3 V and –3 V qualitatively demonstrates the appearance of the $P^{\downarrow}$ and $P^{\uparrow}$states, respectively. The unpoled region outside the larger domain displays the out-of-plane spontaneous polarization $P^{\uparrow}$, which can be attributed to the presence of substrate-induced strains and internal bias in the BTO film. The topography image acquired during the PFM phase image acquisition indicates no surface deformation during the film poling (see Figure 2e). Interestingly, no change in the local conductance of the BTO film upon the polarization switching was observed, as can be seen in the current map shown in Figure 2f. This finding is not consistent with the previous observations [5]. We believe that it was due to the very low leakage current of the BTO barrier and the high contact resistance between the tip and the BTO surface.

We eventually looked into the ferroelectric properties of the BTO barriers sandwiched between two electrodes in complete FTJs. The latter were fabricated by covering the 3 nm thick BTO film grown on LSMO by Au and Cu TEs of 2 m^2 areas, and PFM measurements were performed with the C-AFM tip brought into contact with the TE. Figures 3a and 3b show the phase and amplitude of the local out-of-plane piezoresponse for the FTJs with Au and Cu TEs, respectively. The observed reproducible phase change ~180^0 of the piezoresponse during the voltage sweep indicates that the BTO film retains its ferroelectric state in the presence of the TE as well. It should be noted that extended TEs minimize the electrostatic contribution to the PFM signal and make the electric field inside the probed film almost homogeneous.

To investigate the TER effect, the same FTJs were

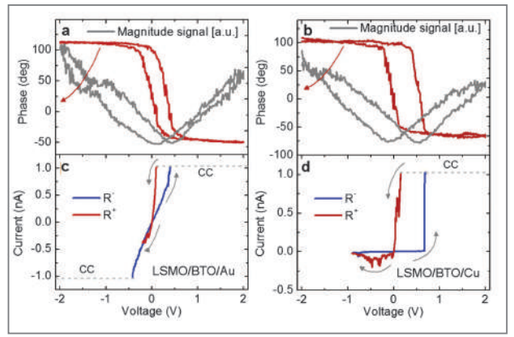

Figure 3. Hysteretic behavior of the PFM phase and magnitude signals with a bias voltage for (a) LSMO/BTO/Au and (b) LSMO/BTO/Cu FTJs. A typical *I-V* curve representing the TER effect in (c) LSMO/BTO/Au and (d) LSMO/BTO/Cu FTJs.

further characterized by measuring their hysteretic *I-V* curves. For each FTJ, a representative *I-V* curve is shown in Figures 3c (FTJ with Au TE) and 3d (FTJ with Cu TE). The FTJs with the extended TEs display hysteretic *I-V* behavior characterized by two dissimilar resistances *R-* and *R+*. Although these resistances vary significantly with the applied voltage, the existence of the distinct high- and low-resistance states of the FTJs is evident. It should be noted that the initial high-resistance state (HRS with *R* = *R-*) switches to the low-resistance state (LRS with *R* = *R+*) at a certain positive voltage and recovers during the negative voltage sweep. The revealed hysteretic electrical behavior and the occurrence of resistive switching events at the coercive voltages of the BTO barrier point to the ferroelectric-driven TER effect. Although the FTJs with Au and Cu TEs display qualitatively similar FE-TER behaviors, their TER ratios differ dramatically. Thus, the TER ratios of the two FTJs may differ by more than 2 orders of magnitude at the same voltage. This drastic difference demonstrates the *giant electrode effect* on TER.

The revealed large difference in the TER ratio between the LSMO/BTO/Cu and the LSMO/BTO/Au FTJs should be attributed to the microscopic interfacial effect. To demonstrate the feasibility of this explanation, we fitted the measured *I-V* curves in the range of small

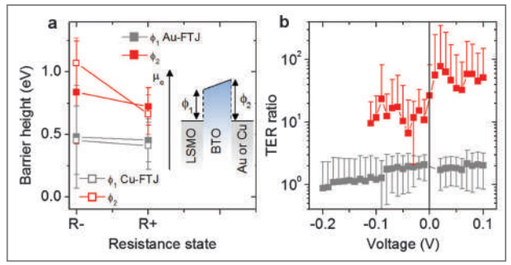

Figure 4. (a) Statistical data on the barrier heights ϕ_1 and ϕ_2 determined by fitting the *I-V* curves of FTJs with Au and Cu TEs measured on five different junctions of the same area (2 μm^2) for each FTJ type (the inset depicts a schematic profile of electron's electrochemical potential μ_e across the junction). (b) Statistical data on the TER ratios of FTJs with Au and Cu TEs obtained from the same five junctions for each FTJ type.

voltages using the tunneling equation. The barrier heights ϕ_1 and ϕ_2, depicted in Figure 4a, were regarded as adjustable parameters independent of applied voltage in the considered voltage range. The barrier heights, determined by the method of least squares, are shown in Figure 4a for the two different FTJs. Interestingly, the change $\Delta\phi_2$ in the barrier height ϕ_2 at the BTO/Au(Cu) interface upon switching between *R+* and *R-* appears to be much larger in the case of the Cu TE. In contrast, only small changes in the barrier height ϕ_1 at the LSMO/BTO interface take place after resistive switching. Since the TER ratio is governed by changes in the barrier heights, the giant electrode effect on TER may be attributed to the difference in $\Delta\phi_2$ between the junctions with Cu and Au TEs.

Although the occurrence of the resistive switching in our FTJs at the coercive voltages of the BTO barrier indicates its ferroelectric origin, BTO is also known as a redox-based resistance switching material [1,6]. Therefore, it is critically important to investigate the redox-based resistive switching behavior of our FTJs in order to clearly distinguish this mechanism from the FE-TER effect. It is known that an electroforming process is usually required to activate redox-based resistance switching phenomena in complex oxide materials. In the present study, considering the electric fields required to trigger

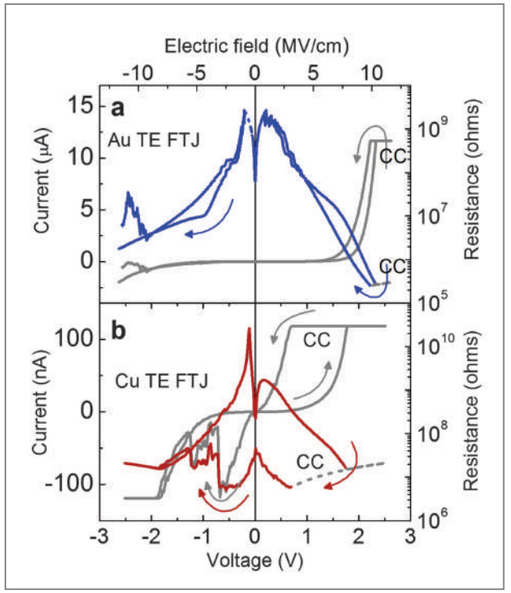

Figure 5. Typical redox-based resistance switching characteristics (*I-V* and *R-V*) of LSMO/BTO heterostructures with (a) Au and (b) Cu TEs. In both panels, the gray curve shows an *I-V* characteristic. The blue and red curves demonstrate *R-V* characteristics of the FTJs with Au and Cu TEs, respectively. CC means compliance current. The upper horizontal axis shows the electric field in the tunnel barrier, which corresponds to the applied voltage given by the lower horizontal axis.

a soft breakdown of the BTO tunnel barrier, we applied comparatively large-range quasi-static voltage sweeps (starting from maximum negative voltage) to the LSMO/BTO/Au and LSMO/BTO/Cu heterostructures using the C-AFM tip to contact the TEs. Figure 5 shows the measured *I-V* and corresponding *R-V* characteristics for the redox-based resistance switching of the LSMO/BTO/Au and the LSMO/BTO/Cu junctions. One can clearly see that in this case the voltages required for the switching to the LRS and back to the HRS are 5-10 times higher than the average switching voltages of the FE-TER effect. Accordingly, the electric fields required for the redox-based switching (ca. 4-8 MV/cm) appear to be much higher than the ferroelectric coercive field of the studied BTO layer.

Conclusion

We have observed the tunneling electroresistance effect in FTJs comprising an ultrathin BTO barrier epitaxially grown on a LSMO BE and covered by micron-sized Au and Cu TEs. Combining the *I-V* measurements performed by C-AFM with the PFM characterization, we found that the resistance switching occurred at voltages consistent with the coercive voltages of the BTO barrier, which confirms its ferroelectric origin. Remarkably, the giant electrode effect on the tunneling electroresistance was revealed, which manifests itself in a drastic reduction (by two orders of magnitude) of the relative resistance changes upon polarization reversal when the Cu TE is replaced by the Au one. A theoretical analysis of the *I-V* curves allowing for the results of additional capacitance measurements indicates that the observed resistance switching is caused by the microscopic interfacial effect, but not by the depolarizing-field effect.

It should be emphasized that it is very unlikely that the TER effect in our FTJs is governed by structural defects. Since the ultrathin epitaxial BTO film is fully strained by the $SrTiO_3$ substrate, misfit dislocations should be practically absent here. Ferroelastic domain walls also cannot form in the BTO film because the substrate-induced high (~ 2%) compressive in-plane strains strongly favor the single-domain state. The transmission electron microscope (TEM) images of the BTO/LSMO interface available in the literature demonstrate the sharpness of this interface, which points to the absence of a defect-rich layer at the BTO/BE interface.

Note

This article and images are drawn from “Giant electrode effect on tunneling electroresistance in ferroelectric tunnel junctions” in *Nature Communications* 2014, Vol. 5. P. 5414.

References

[1] Jeong DS, Thomas R, Katiyar RS, Scott JF, Kohlstedt H, Petraru A, Hwang CS. *Rep Prog Phys.* 2012; 75:076502.

[2] Soni R, Petraru A, Meuffels P, Vavra O, Ziegler M, Kim SK, Jeong DS, Pertsev NA, Kohlstedt H. *Nat Commun.* 2014; 5:5414.

[3] Tsymbal EY, Kohlstedt H. *Science* 2006; 313:181.

[4] Kohlstedt H, Pertsev NA, Contreras JR, Waser R. *Phys Rev B.* 2005; 72:125341.

[5] Maksymovych P, Jesse S, Yu P, Ramesh R, Baddorf AP, Kalinin SV. *Science* 2009; 324:1421.

[6] Kohlstedt H, Petraru A, Szot K, Rudiger A, Meuffels P, Haselier H, Waser R, Nagarajan V. *Appl Phys Lett.* 2008; 92:062907.

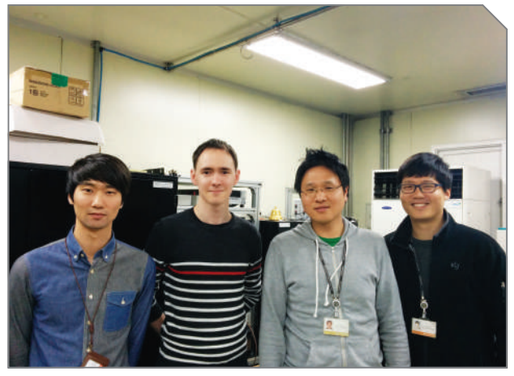

[Feature Articles]

Engineering the Shape and Structure of Materials by Fractal Cut

Insuk Choi
High Temp. Energy Materials Research Center
insukchoi@kist.re.kr

Introduction

Most materials can be stretched to a small degree, depending on their elastic limits and failure properties. For most materials, the maximum elastic dilatation is very small, implying that the macroscopic shapes to which an elastic body can be deformed are severely limited. The focus of this article is the simple modification of any material via hierarchical cut patterns to allow for extremely large strains and shape changes and a large range of macroscopic shapes. This is an important step in the development of shape-programmable materials. This article provides the mathematical foundation, simulation results, and experimental demonstrations of the concept of fractal cut. This approach effectively broadens the design space for engineered materials for applications ranging from flexible/stretchable devices and photonic materials to bioscaffolds.

The physical properties of materials are largely determined by structure: atomic/molecular structure, phase distribution, internal defects, nano/microstructure, sample geometry and electronic structure. Among these, engineering the geometry of the sample can provide a direct, intuitive, and often material-independent approach to achieve a predetermined set of properties. Metamaterials are fabricated based on geometric concepts. In two dimensions, periodic geometries have been adopted to tune the mechanical properties of membranes. From simple shapes, such as circles, triangles, and quadralaterals, to more complex shapes, a broad range of mechanical behavior has been observed, including pattern transformation, negative Poisson's ratio (auxetic), elastic response, and isostaticity. *Origami* and *Kirigami*, the arts of paper folding and paper cutting, create beautiful patterns and shapes that scientists had hoped to apply to two-dimensional materials (e.g., graphene, polymer films, etc.). However, application of conventional Origami and Kirigami approaches to achieve desired material response requires complex cutting and/or folding patterns that are often incompatible with engineered materials. Dr. In-Suk Choi of KIST and his collaborators have proposed a new approach to the design of two-dimensional structures which can achieve a wide range of desirable programmed shapes and mechanical properties.

The study started from the question, "Can we design two-dimensional structures that can be formed by simply cutting a sheet which can then morph into a specific shape?" In nature, many biological and natural systems can be found which employ a hierarchical structure to produce different properties and/or shapes. One such example is a stem cell. An embryonic, pluripotent stem cell can differentiate into any type of cell in the body. By recursively dividing, the stem cell can transform into particular cell types or remain unspecialized with the potential to transform. Using the analogy to the stem cell, KIST researchers demonstrated that starting from a simple sheet of material (the pluripotent state), it is possible to apply different hierarchical cut-patterns (differentiation) to achieve a wide range of macroscopic (unipotent) shapes. Specifically, the researchers focused on "fractal cut" patterns that allow for precise control of differentiated material structures. Their goal was to broaden the design space for engineered materials and systems for a wide range of applications, such as flexible/stretchable devices, photonic materials, and bioscaffolds. They illustrated the concept through numerical simulation, theory and experimental realization.

Results

Basic principle: rotating units

For simplicity, research was focused on a base material in the form of a flat, flexible sheet which was subjected to a prescribed cut pattern. The essence of the design was that cuts divided the material into rotating units, depending on the cut pattern, as exemplified in Figure 1A. The units (e.g., squares or triangles) between cuts were effectively rigid and the connections between these units behaved as nearly free rotational hinges, such that the deformation of the structure (e.g., biaxial or uniaxial stretching) occurred primarily through rotation of the units, rather than by significant deformation of the units themselves.

Fractal cut pattern: hierarchy

In this research, two classes of cut patterns were used: hierarchical and motif alternation. The hierarchical pattern concept is illustrated in Figure 1B for a simple pattern of cuts producing square units. Such square units can be subdivided into smaller squares by repeating the cut pattern within the original square. While the subdivision can, in principle, go on *ad infinitum* creating a true fractal

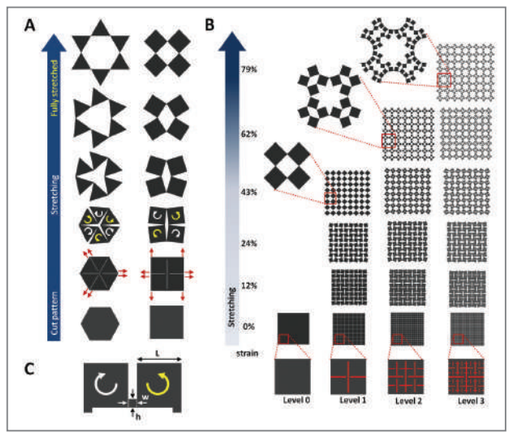

Figure 1. Basic principles behind the patterns of the design cuts.

cut pattern, the focus was on patterns of finite hierarchy degree or level (i.e., the number of times the same cut-pattern is reproduced on the units left by the preceding cuts). Increasing the hierarchy level led to increasingly complex structures and increased expandability. Along with expandability, pore shape, apparent density, and elastic stiffness (assuming the hinges have some resistance to rotation) all varied with the hierarchy level. The variables that determined the final structure of the stretched sheet were the rotation angles between rotating units. The number of independent variables increased as hierarchy level increased.

Fractal cut pattern: motif

Besides hierarchy, another design parameter involved the cut motif. As described in the previous section, the cut motif was kept constant (square or triangular), as indicated by the red lines in Figure 1B (the α-motif). This same motif applied homogeneously led to the same unit rotation pattern across the entire structure as indicated by the white and yellow arrows in Figure 1A. The number of degrees of freedom, F, grew monotonically with the hierarchy level, while the increment of rotation angle became smaller. Another motif, β, could be formed by rotating the α-motif by 90°, as shown in blue at the bottom of Figure 2. In this motif the square units rotated in opposite directions relative to those in the α-motif. Thus, the combination of α- and β-motif between levels produced alternating rotation directions of the units, leading to larger rotation angles and strains at higher levels (see Figure 2B).

Engineering shape and structure via fractal cut

Hierarchical levels and motifs provide the basic palette that can be used to draw (i.e., cut pattern) on a blank canvas (or material sheet). Different motifs and levels give different rotation patterns and strains allowing for tunability. In the case of two motifs, the total number of ways to cut the material was evaluated. At the first level, where the α- or β-motif can be applied, there were only

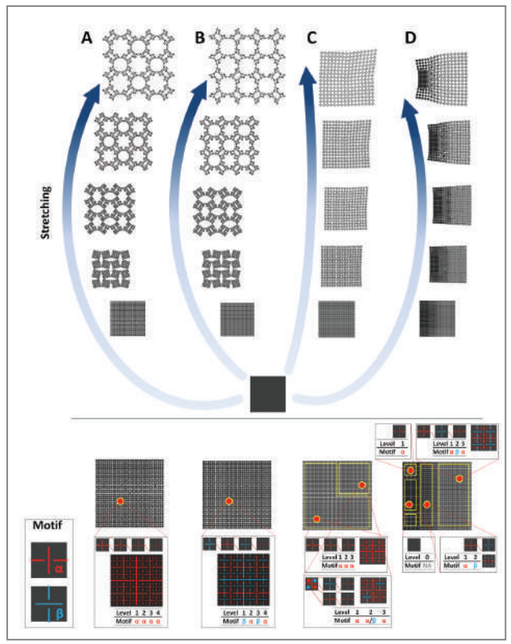

Figure 2. Two cut motifs in a hierarchical structure.

two permutations. At level 2, each of the four sub-squares had one of two motifs (i.e., 16 possibilities). Therefore, in a level 2 structure, there were 32 permutations. Any level N structure with two motifs can be described with a simple equation.

Here, level and motif distributions represent a mechanism for pluripotency. The original sheet (intact square) is pluripotent; when the fractal cut design is embedded, the sheet becomes unipotent. Upon stretching, the rotation of the units activates the differentiation. The final sheet shape can be programmed. For example, Figure 2C shows the non-uniform expansion of a level 3 structure with an inhomogeneous combination of α- and β-motifs, and Figure 2D shows the expanded shape resulting from a mixture of different hierarchy-levels and motifs. The pluripotency of a single square sheet can be exploited to reproduce shapes of considerable

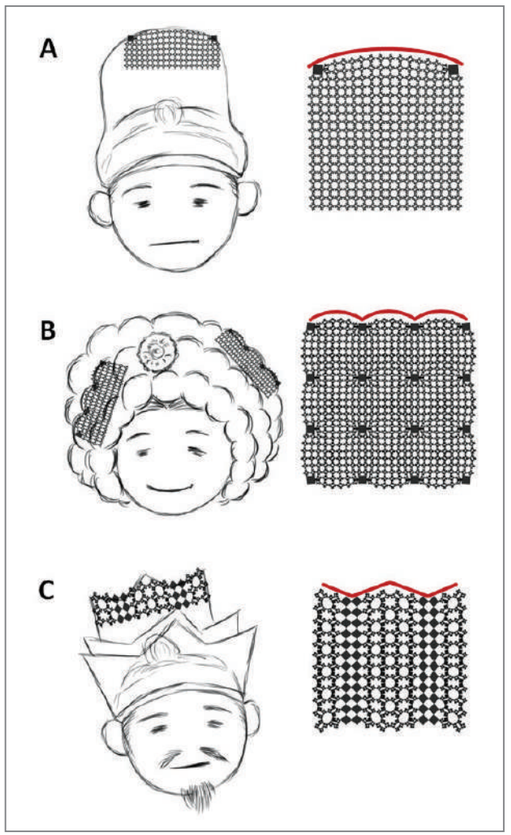

Figure 3. Fractal-cut traditional Korean hats and hairstyles.

complexity. Figure 3 applies such an approach to reproduce traditional Korean hats and hairstyles.

Experimental realizations

Structural differentiation was experimentally realized as shown in Figure 4. Square sheets of silicone rubber with four different fractal cut patterns were fabricated using three-dimensional printed molds. Figures 4A-D correspond to the simulated patterns from Figures 2A-D. When stretched, the square sheets showed final shapes which very nearly matched the simulation results.

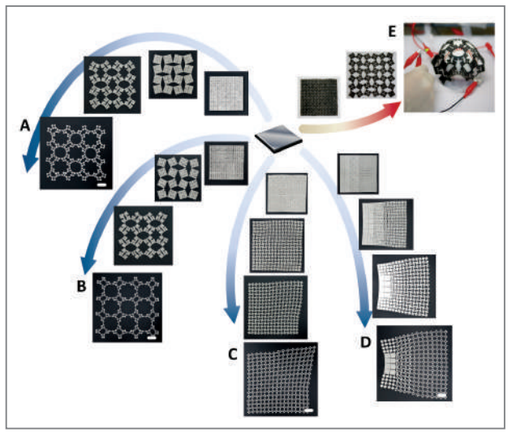

Figure 4. Macroscopic experimental realization.

Obviously, the concept of fractal cutting is not confined to a specific material system nor to a specific feature size. For example, reducing the smallest feature scale in the level 4 structures in Figures 4A and 4B from 2 mm to 40 μm using photolithography to make molds into which polydimethylsiloxane (PDMS) sheets were cast, led to identical differentiation (see Figure 5). Hence, the described approach to forming highly expandable pluripotent materials can be applied on a macro-, or micro-scale.

Discussion

The pluripotent material approach provides an effective means for the design of structural platforms for stretchable and flexible devices. Since stretching occurs by unit rotation rather than deformation, the material in the structure is inherently nearly strain free (except at the hinge points); this is essential for stretchable platforms. It can also be strained without buckling. Thus, deformation of the structure will not alter the physical properties/function of the materials deposited on top of the units. Figure

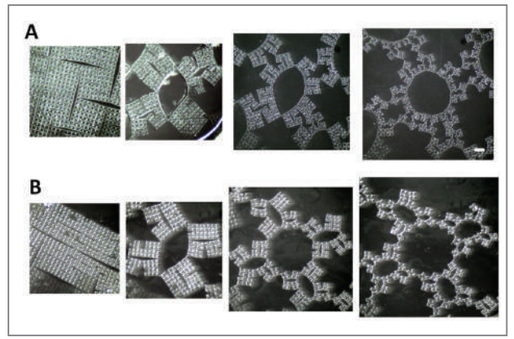

Figure 5. Microscopic experimental realization.

4E shows a proof of concept of a stretchable electrode with a fractal cut. A conductive film of multiwall carbon nanotubes was deposited on a silicone rubber sheet with an embedded homogeneous N=3, α-motif. An LED was continuously powered through the conductive film as the cut silicone rubber sheet was stretched over a spherical baseball. The conformal wrapping of the sheet around a non-zero Gauss curvature object (a sphere in this case) leads to non-uniform stretching (and non-uniform opening patterns), which can easily be accommodated by the fractal cut sheet. This approach to stretchable/flexible substrates differs from others presented in the literature, where expansion and conformal wrapping of a flexible device consisted of rigid components connected through stretchable elements (e.g., springs and serpentines). In the KIST-developed system, since the deformation is based on unit rotation, a highly expandable device can be fabricated by placing conventional hard devices (e.g., battery, circuit, LED, etc.) on the rotating units without sacrificing device performance during large deformation.

Achieving a target expandability for distribution/morphology in material design is an inverse problem in cut geometry. Unlike many materials design problems, the inverse problem for fractal cut structures is relatively straightforward, as evidenced by the simple design palette (cuts) described here and the straightforward calculations implied by the theoretical idealization. While the present results focused on two-dimensional sheets with square based units as a starting point, the same approach can be applied with (a) different two-dimensional base units and (b) three-dimensional materials using one of the many recent technological advances in three-dimensional printing. By prescribing the geometry of cuts in a sheet, not only can the meso/nano structure of a sheet be easily controlled, but also, all of the properties that contribute to its structure can be engineered, including those associated with shape (pore size, pore shape, macro-geometry, maximum strain), mechanical properties (full stiffness tensor), and even material properties coupled with structures (electrical, photonic, acoustic properties). Many of these properties require additional manipulation of the connections between the rotating units (e.g., stiffness depends on finite length of the material in hinges). Designing actuation or pre-rotations into the structure can further enhance the flexibility and functionality of cut structures for various applications.

Conclusion

In this article we discussed the transformation of a sheet of material into a wide range of desired shapes and patterns by introducing a set of simple cuts in a multilevel hierarchy with different motifs. Each choice of hierarchical cut motif and cut level allowed the material to expand into a unique structure with a unique set of properties. We could reverse-engineer the desired expanded geometries to find the requisite cut pattern without changing the physical properties of the initial material. This concept was experimentally realized and applied to create an electrode that expanded to >800% of the original area with only very minor stretching of the underlying material. The generality of our approach greatly expands the design space for materials so that they can be tuned for diverse applications.

Note

This article and images are drawn from “Engineering the shape and structure of materials by fractal cut” in *PNAS*, Vol. 111 (49), pp. 17390-17395.

References

[1] Babaee S, Shim J, Weaver JC, Chen ER, Patel N, Bertoldi K. Adv Mater 2013;25:5044.
[2] Lee, J, Singer, PJ, Thomas LE. Adv Mat. 2012;24:4782.
[3] Grima JN, Alderson A, Evans KE. Comp Meth Sci & Tech 2004;10:9.
[4] Kang SH, Shan S, Kosmrlj A, Noorduin WL, Shian S, Weaver JC, Clarke DR, Bertoldi K. Phys Rev Lett 2014;112.
[5] Schenk M, Guest SD. Geometry of Miura-folded metamaterials. P Natl Acad Sci USA 2013;110:3276.
[6] Sun K, Souslov A, Mao XM, Lubensky TC. P Natl Acad Sci USA 2012;109:12369.

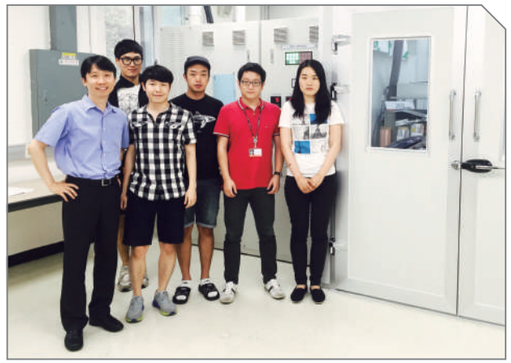

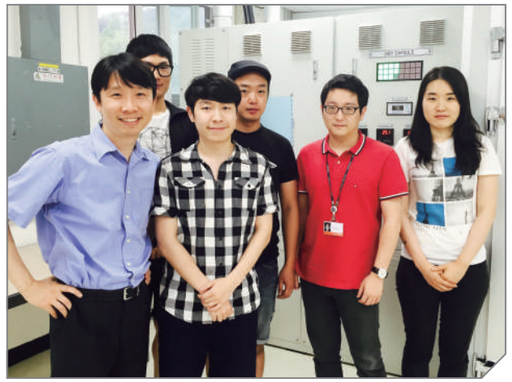

[Technical Review]

Making Better Batteries for a Sustainable Future: Batteries Based on Multivalent Charge Carriers

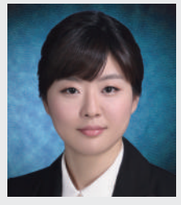

Boeun Lee
Center for Energy Convergence Research
215013@kist.re.kr

Si Hyoung Oh
Center for Energy Convergence Research
sho74@kist.re.kr

Introduction

With the rapid expansion of global markets for electric vehicles (EV) and commercial energy storage systems (ESS), the demand for safe, low-cost energy storage systems with a high energy density has intensified (Figure 1). The growth of these markets has resulted from grave concerns about global climate change and increasing international regulations on greenhouse gas emissions. These emissions have been implicated as a factor associated with many weather-related disasters around the world [1].

To date, Li-ion batteries have been the standard for powering portable electronic devices, but in order to power large-scale applications such as electric vehicles or ESS, new energy storage systems with fundamentally different reaction mechanisms are needed to meet the economic and safety requirements for commercialization. In the search for effective alternatives, extensive investigation is underway into a variety of new energy storage systems based on multivalent cation charge carriers, such as Mg^{2+}, Zn^{2+}, and Al^{3+} ions [2-9]. These elements are attractive since they are not only abundant in the earth's crust but also have a high volumetric capacity. Therefore, these materials are considered to be inexpensive, yet-to-be efficient negative electrode materials (Figure 2).

Unfortunately, battery systems based on multivalent cations face serious technical challenges, but researchers worldwide are looking for solutions. A common difficulty is to develop a working electrolyte system containing

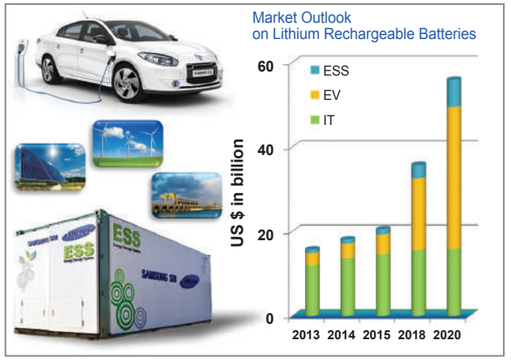

Figure 1. Representative commercial products (IT devices, electric vehicles and ESS) for mid- to large-scale battery applications and recent trends in these rising markets. (source: SNE Research, Competitiveness Report on the Leading Rechargeable Battery Makers. (Feb 2015))

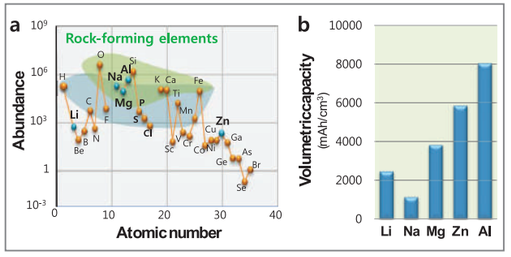

Figure 2. (a) Abundance of major chemical elements in earth's crust. (b) Comparison of volumetric capacity of certain metals of interest based on $M \rightarrow M^{2+} + ze^-$. Aluminum has the highest volumetric capacity of all elements due to its trivalency and high material density.

multivalent cation charge carriers which is stable during the electrode reactions and which has a high energy efficiency. Since a multivalent cation carries a high positive charge within a small ionic radius, these cations induce strong electrostatic interactions with neighboring solvent molecules or ionic species present in the solutions, forming bulky coordinated complex ions [7, 10]. This leads to large effective Stokes' radii for most multivalent cations, which deters the diffusion of the charge-transport carriers through the electrolyte.

The strong coordination between a multivalent cation with its ligands also causes costly large de-solvation energy for the complex ions to overcome when they enter into the crystal structure of electrode materials. The development of positive electrode material which undergoes reversible electrode reactions with multivalent cations and also exhibits reasonable performance at high current rate is another challenge [7, 10]. It is well known that the high coulombic interaction between a multivalent cation and its surrounding crystal structure disturbs the diffusion of cations through inorganic hosts due to the difficulty in redistributing the multiple charges within the local crystal structure. The diffusion constant of these cations within the same material can be several orders lower in magnitude than monovalent ones, such as Li^+ ions. So far, many attempts have been made to tackle this issue, such as downsizing the material to nanoscale to reduce the diffusion path, or using additives to shield the high charge from the multivalent cations.

Magnesium rechargeable batteries

Magnesium is attractive as a negative electrode material since it has a low standard reduction potential of -2.372 V vs a standard hydrogen electrode (SHE) and high gravimetric and volumetric capacity of 2,205 Ah/kg and 3,822 Ah/L, respectively. Furthermore, it is abundant in the earth's crust, as evidenced by sea water which contains 0.13% of magnesium as one of its main constituents. Primary batteries of the metal-air type using a magnesium metal anode have been investigated since the early 20th century; however, a prototype cell using a rechargeable system was demonstrated only in 2000 by D. Aurbach et al. In the prototype cell, Mo_6S_8 Chevrel phase was adopted as an efficient Mg^{2+}-intercalating host for a cathode material, and an *in situ* electrolyte solution based on Mg organohaloaluminate was employed as an electrolyte system (Figure 3) [6].

The main drawback of the electrolyte used by Aurbach et al. in their first report was its unsatisfactory anodic stability, although this stability was much improved

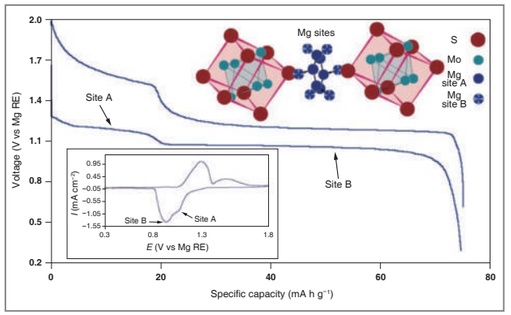

Figure 3. (a) The performance of a magnesium rechargeable battery prototype cell made of Chevrel phase and a magnesium organohaloaluminate electrolyte solution.

compared to that in a conventional Grignard solution, which is too low to employ any other cathode material than Chevrel phase. Accordingly, much of the research in this field has been focused on the development of a new electrolyte system which shows a wide electrochemical window while maintaining its reversible character on negative electrode reactions [10]. Recently, many approaches have been taken to the development of a new electrolyte system based on the concept of combining Lewis acid and Lewis base to produce stable *in situ* electrolyte solutions [11-13]. The right choice of appropriate Lewis base for producing a stable *in situ* electrolyte having much reduced nucleophilicity is of key importance. The development of cathode materials has been slow due to the lack of a working electrolyte system which can be used to evaluate their properties. Since the divalent Mg^{2+} ions undergo much stronger electrostatic interactions with their surrounding crystal structures when they pass through a solid host, materials with a large crystallographic tunnel such as α-MnO_2 or those with a wide interlayer spacing, for example, orthorhombic V_2O_5, have been proposed so far as plausible candidates [7, 10]. Control of the coordination chemistry of Mg^{2+} has also been reported to reduce the effective charge from a divalent cation, but this approach requires a very large tunnel size of the hosting material to incorporate large coordinated complex ions into its crystal structure [7, 10].

Aluminum rechargeable batteries

For a long time, aluminum has been considered a future energy material by many researchers due to its high energy density originating from its trivalent charge and high material density. It is the most abundant metallic species in the earth's crust (8.3% by weight). Its specific capacity, 2,980 Ah/kg, is comparable to that for lithium, 3,861 Ah/kg, and it has a relatively low standard reduction potential of -1.662 V vs. SHE. Most of all, its volumetric capacity, 8,046 Ah/L, is one of the highest in all elements, and four times higher than that of lithium (2,062 Ah/L). However, in most cases, aluminum forms a compact and stable passivating layer on its surface, which interferes with a reversible deposition/dissolution of aluminum from the electrolyte except in the case of some known ionic liquids containing a strong Lewis acid [9]. For example, ionic liquids such as 1-ethyl-3-methylimidazolium tetrachloroaluminate ($AlCl_3$-EMIC), and 1-butyl-3-methylimidazolium tetrachloroaluminate ($AlCl_3$-BMIC) are utilized as an effective electrolyte system to guarantee a reversible plating and stripping of aluminum from the negative electrode (Figure 4). However, due to the highly corrosive nature of these ionic liquids, proper protection of cell components is always required by applying a resistive coating layer or adding corrosion inhibitors [14].

Research for potential cathode materials has been focused on developing a new intercalation host for Al^{3+} ions since this insertion process is considered even more difficult than that for Mg^{2+} ions due to the trivalent character of Al^{3+} ions. So far, the properties of vanadium oxides with a layered or tunnel structure, such as orthorhombic V_2O_5 and monoclinic VO_2, have been explored [9], but in many cases, it has been determined that the electrochemical signals from these experiments were actually related to the corrosion of cell components, such as current collectors, and thus, research remains in early stages [14].

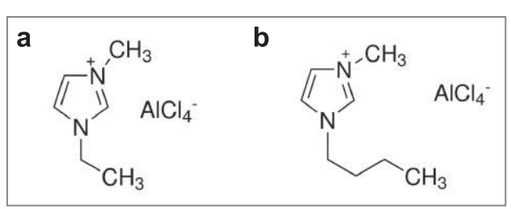

Figure 4. Common ionic liquids used as electrolyte systems for Al rechargeable batteries: (a) 1-ethyl-3-methylimidazolium tetrachloroaluminate; and (b) 1-butyl-3-methylimidazolium tetrachloroaluminate.

Zinc rechargeable batteries

Fundamentals of Zinc Rechargeable Batteries

Rechargeable zinc batteries have gained world-wide attention as one of the most viable candidates for replacing Li-ion batteries since reported by Kang et al. in 2012 [2-5]. They consist of totally environmentally benign electrode materials: MnO_2 cathodes, zinc metal anodes and aqueous electrolyte systems. Furthermore, they can potentially be manufactured very economically. They can employ many forms of polymorphic MnO_2 as cathode material, including α-MnO_2, β-MnO_2, γ-MnO_2, λ-MnO_2, and todorokite, that can incorporate zinc ions into their tunneled structures [15-20]. Specifically, α-MnO_2 can produce large discharge capacities (as large as 210 mAh g^{-1}) with a practical discharge potential of 1.3 V at a moderate current rate, leading to an energy density of 225 Wh kg^{-1} [2-5], which is substantially greater than values reported for competing systems based on multivalent cation charge carriers, such as magnesium rechargeable batteries (146 Wh kg^{-1}) [6-8]. However, Zn/α-MnO_2 batteries show significant capacity fading during long-term cycling and also suffer from poor performance at high current rates.

Structural and morphological development of cathodes during cycling

In a study conducted by KIST researchers, α-MnO_2 nano-rods were synthesized from $KMnO_4$ by a hydrothermal method [21]. The use of nano-rods enables

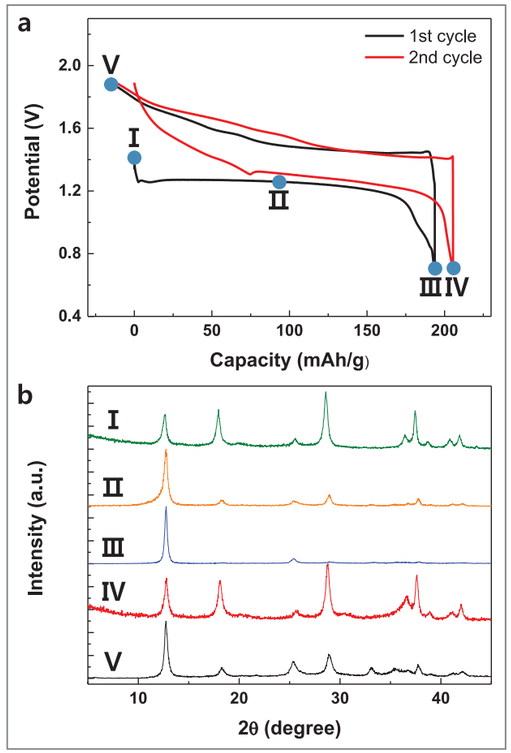

Figure 5. (a) Potential profiles of a zinc/α-MnO_2 Zn-ion battery during the first (black line) and the second (red line) cycles, and its cycling performance up to 30 cycles (inset). (b) *Ex situ* X-ray diffraction patterns of the electrodes at various stages, as indicated in Figure 5a.

any morphological changes to be easily detected following electrochemical reactions. Coin cells containing α-MnO_2 cathodes, zinc metal anodes, and aqueous 1.0 M $ZnSO_4$ electrolyte were employed for electrochemical evaluations. Figure 5a exhibits the discharge-charge profile of a zinc/α-MnO_2 battery for its first two successive cycles using a slow current rate of C/20 and a cycling capacity retention up to 30 cycles. During the first discharge, a potential plateau near 1.3 V suggests that two phases are involved in the reaction [22, 23]. The observed capacity of α-MnO_2 was approximately 194 mAh g^{-1} for the first cycle and increased to 205 mAh g^{-1} for the second. These values are close to those reported in previous papers [2-5].

Changes to the crystal structure of the α-MnO_2 nano-rods following interaction with zinc ions were investigated by analyzing *ex situ* X-ray diffraction (XRD) patterns of the original (I), half-discharged (II), fully-discharged (III), charged (IV), and 2nd discharged (V) cathodes, as shown in Figure 5b. After a full discharge to 0.7 V (III), a strong single reflection from a new phase with a *d*-spacing of approximately 7 Å was observed in addition to a few minor reflections, and those of α-MnO_2 disappeared. After charging to 1.9 V (IV), the new phase disappeared and the original α-MnO_2 structure resurfaced, implying that the process was reversible. At the half-discharge (II), a mixture of the α-MnO_2 and the new phase was observed, in accordance with electrochemical measurements. After the second discharge (V), the new phase reappeared as the main discharge product.

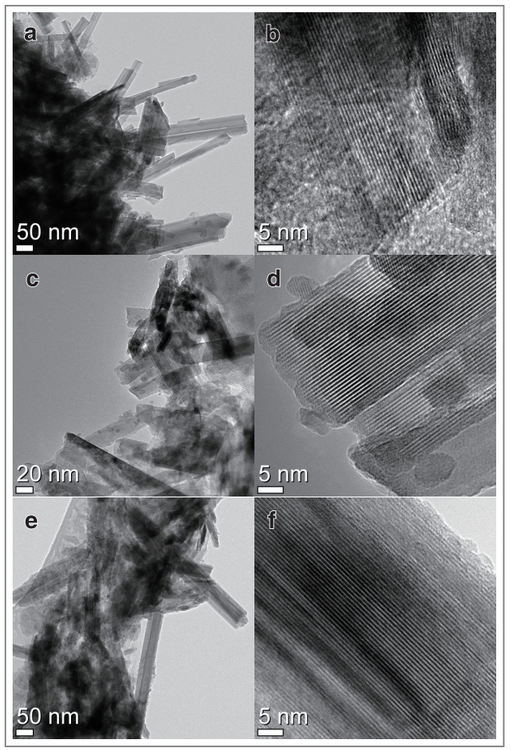

Figure 6. High-resolution transmission electron micrograms at low and high magnification, respectively; **(a), (b)** for the original undischarged cathodes containing α-MnO_2 nano-rod; **(c), (d)** for the first discharged cathodes; and **(e), (f)** for the discharged and then recharged cathodes.

Morphological observations of the cathodes indicated that the original nano-rod shape and crystallographic integrity of α-MnO_2 were well-preserved throughout the first discharge-charge cycle. Specifically, tunnels or layers, homogenously spaced approximately 7 Å apart, were clearly visible throughout the entire electrochemical process (Figure 6). These observations indicate that the structure of the new phase in the discharged electrode was closely related to that of the original α-MnO_2 and that intercalation is mostly likely responsible for the electrochemical reaction, as reported previously [2,5].

Identification of the discharge product

Since the XRD pattern is not conclusive in clarifying the discharge product, transmission electron microscopy (TEM) analysis was carried out on individual nano-rods. Figure 7a shows an electron diffraction pattern of an original α-MnO_2 nano-rod before electrochemical cycling. The diffraction pattern was indexed to the [-110] zone of a tetragonal lattice in the I4/m space group. The lattice spacing estimated from the electron diffraction pattern matched the literature value and XRD data well. A bright field TEM image of the discharged nano-rod is shown in Figure 7b. Although the nano-rod morphology remained intact after full discharge, the non-uniform contrast suggests that the observed nano-rod was likely highly strained. The corresponding electron diffraction pattern, shown in Figure 7c, was indexed to the [012] zone of triclinic chalcophanite ($ZnMn_3O_7 \times 3H_2O$) (space group P-1) [24, 25]. In order to ascertain the correct indexing of the diffraction pattern, a simulated kinematic electron diffraction pattern of the [012] zone, produced using WebEMAPS [26], is shown in Figure 7d. Two diffraction vectors, (100) and (-121), are denoted in Figures 7c and 7d to illustrate that the two patterns (experimental and simulated) match each other. A similar analysis for other zones also indicates that the structure of discharge product is that of triclinic chalcophanite.

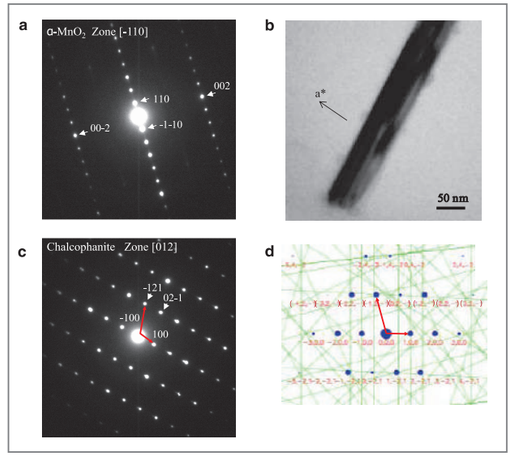

Figure 7. (a) Electron diffraction pattern of the original α-MnO_2 nano-rod, indexed to the [-110] zone of a tetragonal lattice with space group I4/m. (b) Bright field TEM image of the discharged nano-rod, (c) its corresponding electron diffraction pattern, indexed to the [012] zone of a triclinic lattice with space group P-1, and (d) a simulated kinematic electron diffraction pattern of the [012] zone produced using WebEMAPS.

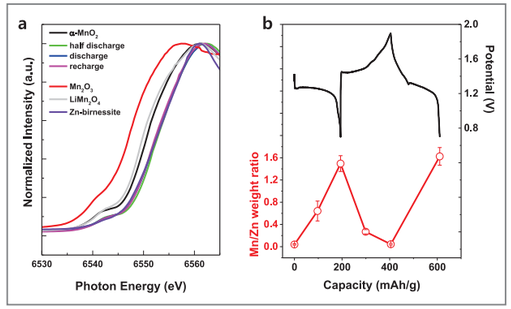

Figure 8. (a) Mn K-edge X-ray absorption spectra for as-prepared α-MnO_2 and electrodes at various discharge and charge stages, as indicated in Figure 5a. (a) also includes reference spectra for Mn_2O_3, $LiMn_2O_4$, and Zn-birnessite. (b) Mn/Zn weight ratio in the electrolyte (red square) measured by AAS during electrochemical cycling and the discharge-charge profile (black).

The electron diffraction and chemical analysis of the discharged product suggest that the α-MnO_2 nano-rods underwent a phase transition during discharge to form Zn-birnessite, a triclinic chalcophanite-like layered structure with P-1 space group [24, 25]. The structure of chalcophanite closely resembles that of layered Na-birnessite ($Na_4Mn_{14}O_{27} \cdot 9H_2O$), in which intercalated Zn^{2+} ions sit above and below Mn vacancy sites within the layers and form octahedra by coordinating with three oxygen atoms from water molecules and three oxygen atoms from the Mn vacancy sites below [24, 25, 27, 28]. In contrast to Na-birnessite, the chalcophanite structure is stable even in the absence of water and has been widely investigated to clarify the structure of the birnessite family. When the number of Zn ions intercalated into layers is small, Zn ions accommodate tetrahedral coordination with three oxygen atoms from Mn vacancy sites and one from a water molecule [25, 26].

To further confirm the discharge product, we investigated the oxidation state of the manganese in the electrode by measuring Mn K-edge X-ray absorption spectra, shown in Figure 8a. At the Mn K-edge, the selection rule for electrical dipolar transitions ($\Delta l = \pm 1$) requires that a 1s electron jump to an empty 4p orbital ($1s^2 4p^0 \rightarrow 1s^1 4p^1$). The position of the absorption edge is affected by the oxidation state of the central absorbing atom [29, 30]. From Figure 8a, the oxidation state of the manganese in the discharged material is estimated to be nearly identical to that of the Zn-birnessite synthesized from Na-birnessite using the hydrothermal method. Therefore, we conclude that Zn-birnessite is the main discharge product remaining at the electrode.

Intercalation mechanism of zinc ions into α-MnO_2

The Mn K-edge absorption spectra, shown in Figure 8a, indicate that the average oxidation state of manganese in the discharged electrode increases, then remains almost unchanged upon further recharging, since the Mn K-edge moves to higher energies as oxidation state increases [29, 30]. This indicates that some manganese goes into the electrolyte in the form of Mn^{2+} ions, leaving Mn vacancy sites in the electrode. This

can occur as the manganese in α-MnO_2 is reduced from tetravalent to trivalent, upon electrochemical intercalation of zinc ions, and Mn^{3+} disproportionates into Mn^{4+} and Mn^{2+} according to the following reactions.

$$Mn^{4+}(s) + e^- \rightarrow Mn^{3+}(s) \quad (1)$$

$$2Mn^{3+}(s) \rightarrow Mn^{4+}(s) + Mn^{2+}(aq) \quad (2)$$

The dissolved Mn^{2+} ions accumulate in the electrolyte during discharge. Considering that the solubility of Mn^{2+} ions in water is typically high, a substantial number of manganese ions have been dissolved into the electrolyte by the end of the discharge process. It is well known that Mn^{3+} ions, having a high-spin d^4 ($=t_{2g}^3e_g^1$) electronic configuration in octahedral symmetry, are highly unstable due to the Jahn-Teller effect, and susceptible to structural transformations [30, 32]. This structural instability often triggers a disproportionate reaction, resulting in the dissolution of some manganese and the destruction of the original structure of the host material. To confirm this, the amounts of Mn in the electrolyte at various stages of the charge/discharge cycle were evaluated by analyzing Mn/Zn ion ratios of the electrolyte using atomic absorption spectroscopy (AAS). As shown in Figure 8b, the amount of Mn increased as the discharge process proceeded, reaching a maximum at the end of the discharge process. Compared to the concentration of zinc ions in the electrolyte (1.0 mol/L), the amount of Mn, following discharge, corresponds to approximately 1/3 of the total manganese in the electrode. During charging, the Mn concentration of the electrolyte became negligibly small, which means that dissolved Mn^{2+} ions returned to combine with Mn vacancy sites of the layered structure and were oxidized to become Mn^{3+} and Mn^{4+}.

$$Mn^{2+}(aq) \rightarrow Mn^{4+}(s) + 2e^- \quad (3)$$

Therefore, the manganese in the electrode maintained a high oxidation state throughout the entire discharge-charge process, as observed in the Mn K-edge spectra in Figure 8a.

The α-MnO_2 has one-dimensional 2 x 2 and 1 x 1 tunnels, comprised of four identical cross-linking double chains of MnO_6 octahedra that extend along the c-axis, the edges of which are connected by corner-sharing MnO_6 octahedra, as described in Figure 9. Conversely, Zn-birnessite has a layered structure with an interlayer spacing of approximately 7 Å, which is similar to the size of the tunnels of α-MnO_2, also shown in Figure 9. In fact, the crystal structure of Zn-birnessite would be closely related to that of α-MnO_2 if there were bridges connecting adjacent layers in Zn-birnessite. Therefore, noting the similarities of the crystal structures of α-MnO_2 and Zn-birnessite, it is reasonable to assume that during discharge the MnO_6 units of two opposite chains of α-MnO_2 undergo destructive dissolution and that Mn vacancies form in the upper and underlying layers. Furthermore, during recharging, Mn^{2+} ions intercalate back into the layers and start to form bridges between layers.

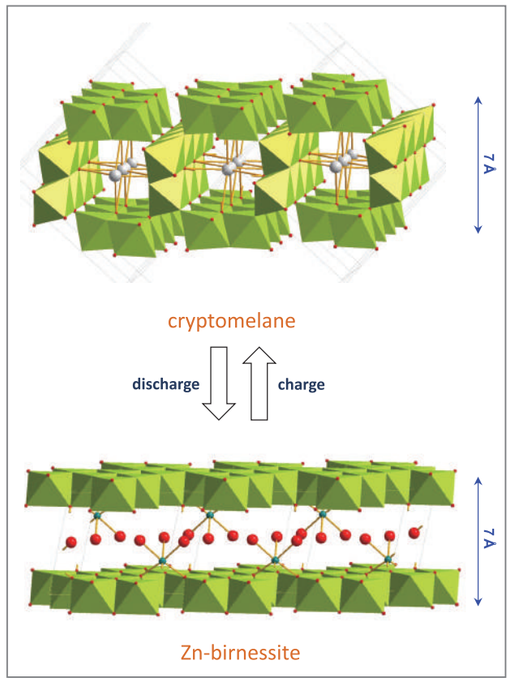

Figure 9. Schematic illustrating the mechanism of zinc intercalation into 2 x 2 tunnels of α-MnO_2 and subsequent phase transition to layered zinc-birnessite.

Structural degradation and capacity fading upon cycling

Figure 10 shows charge-discharge profiles at the 1st, 5th, and 10th cycles and XRD patterns of fully-discharged and fully-charged electrodes at those cycles. The profiles show that while Zn-birnessite and α-MnO_2 still form at later cycles after the discharge and charge process, respectively, amorphous phase grows as the cycle proceeds. An excessive structural stress developed by the repeated phase transitions probably caused the gradual destruction of the original structure and the conversion to amorphous phase.

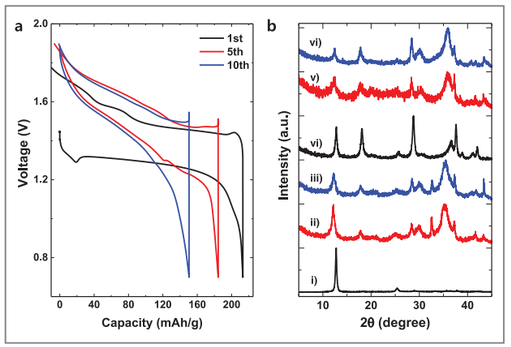

Figure 10. (a) Discharge-charge curves at the 1st, the 5th and the 10th cycles at C/10 current rate. (b) XRD patterns of fully discharged cathodes at (i) the 1st, (ii) the 5th, and (iii) the 10th cycles and those of fully charged cathodes at (iv) the 1st, (v) the 5th, and (vi) the 10th cycles.

Conclusion

The accumulation of greenhouse gases from the burning of fossil fuels for the last several centuries and the depletion of worldwide natural resources has sparked an urgent need for the development of green energy sources and ways to efficiently use existing resources. This trend is expected to persist throughout this century, creating immense emerging markets for products such as electric vehicles and ESS to make efficient use of electrical energy. In this regard, the development of large-scale energy storage systems with a higher energy density at much lower cost than conventional Li-ion batteries will be one of the most important topics for the scientific community to pursue. Battery systems based on multivalent charge carriers provide one of the most viable options to meet these needs due to their high intrinsic energy densities and natural abundance in the earth's crust. Therefore, intensive research is urgently needed in this field to solve the many technical challenges that remain and prepare for the impact of climate change.

References

[1] *Understanding and Responding to Climate Change*, United States National Academy of Sciences, 2008.
[2] Xu C, Li B, Du H, Kang, F. *Angew. Chem. Int. Ed.* 2012; 51: 933-935.
[3] Xu C, Li B, Chiang SW, Ma J, Kang F. *J. Electrochem. Soc.* 2013; 160: A93-A97.
[4] Lee J, Ju JB, Cho WI, Cho BW, Oh SH. *Electrochimica Acta.* 2013; 112: 138-143.
[5] Lee B, et al. *Sci. Rep.* 2014; 4: 6066. DOI:10.1038/srep06066
[6] Aurbach D, et al. *Nature* 2000; 407: 724- 727.
[7] Levi E, Gofer Y, Aurbach D. *Chem. Mater.* 2010; 22: 860-868.
[8] Jayaprakash N, Das SK, Archer LA. *Chem. Commun.* 2011; 47: 12610-12612.
[9] Wang W, et al. *Sci. Rep.* 2013; 3: 3383. DOI:10.1038/srep03383
[10] Yoo HD, et al. *Energy Environ. Sci.*, 2013; 6: 2265-2279.
[11] Mizrahi O, et al. *J. Electrochem. Soc.* 2008; 155: A103-A109.

[12] Kim HS, et al. *Nat. Commun.* 2001; 2: 427. DOI:10.1038/ncomms 1435
[13] Liu T, et al. *J. Mater. Chem. A* 2014; 2: 3430-3438.
[14] Reed LD, Menke E. *J. Electrochem. Soc.* 2013; 160: A915-A917.
[15] Post JE. *Proc. Natl. Acad. Sci.* 1999; 96: 3447-3454.
[16] Thackeray MM. *Prog. Solid St. Chem.* 1997; 25: 1-71.
[17] Neburchilov V, Wang H, Martin JJ, Qu W. *J. Power Sources* 2010; 195: 1271-1291.
[18] Gritter RJ, Wallace TJ. *J. Org. Chem.* 1959; 24: 1051-1056.
[19] Villalobos M, Lanson B, Manceau A, Toner B, Sposito G. *Am. Mineral.* 2006; 91: 489-502.
[20] Chabre Y, Pannetier J. *Prog. Solid St. Chem.* 1995; 23: 1-130.
[21] Gao Y, Wang Z, Wan J, Zou G, Qian Y. *J. Cryst. Growth* 2005; 279: 415-419.
[22] Delmer O, Balaya P, Kienle L, Maier J. *Adv. Mater.* 2008; 20: 501-505.
[23] Yamada A, et al. *Nat. Mater.* 2006; 5: 357-360.
[24] Wadsley AD. *Nature* 1953; 172: 1103-1104.
[25] Wadsley AD. *Acta Cryst.* 1955; 8: 165-172.
[26] Zuo JM, Mabon JC. (2004) *Web-based Electron Microscopy Application Software: Web-EMAPS, Microsc Microanal 10 (Suppl 2).* Retrieved from http://emaps.mrl.uiuc.edu/
[27] Kwon KD, Refson K, Sposito G. *Geochim. Cosmochim. Acta.* 2009; 73: 1273-1284.
[28] Toner B, Manceau A, Webb SM, Sposito G. *Geochim. Cosmochim. Acta.* 2006; 70: 27-43.
[29] Mehadji C, Nour S, Chermette H. *Chem. Phys.* 1990; 148: 95-102.
[30] Kobayahi S, Kottegoda IRM, Uchimoto Y, Wakihara M. *J. Mater. Chem.* 2004; 14: 1843-1848.
[31] Thackeray MM, et al. *Electrochem. Solid-State Lett.* 1998; 1: 7-9.
[32] Berg H, Göransson K, Nölang B, Thomas JO. *J. Mater. Chem.* 1999; 9: 2813-2830.

[**Feature Articles**]

Membrane Fouling Control Using Rotary Disks and Sponge Media in a Submerged Anaerobic Membrane Bioreactor

Jaewon Shin
Center for Water Resource Cycle Research
213007@kist.re.kr

Kyung Guen Song
Center for Water Resource Cycle Research
kgsong@kist.re.kr

Introduction

The anaerobic wastewater process is increasingly attractive as an alternative to aerobic treatment because its electricity, capital, maintenance, and operating costs may be offset by methane production [1]. Anaerobic processes do not require aeration, which can account for nearly one-half of the total energy input for biological wastewater treatment [2]. The effluent quality of conventional anaerobic treatments, however, does not generally meet the stringent regulatory limits for chemical oxygen demand (COD) and suspended solids (SS). The use of a membrane can retain microorganisms within the system, lengthen the solid retention time (SRT), shorten the hydraulic retention time (HRT), and enhance effluent quality. The introduction of submerged membrane modules in wastewater treatment has significantly reduced the energy consumed during operation relative to cross-flow membrane bioreactors (MBRs). This efficiency has accelerated the utilization of MBRs [3].

One of the most frustrating issues in MBR application is membrane fouling, which causes a significant reduction in the flux, membrane efficiency, and membrane replacement period, and increases the operation costs. Several attempts have been made to reduce membrane fouling in MBR technologies (e.g., by treating the feedwater, reducing the flux and backwashing processes, cleaning the chemical and physical membranes, and generating turbulence) [4]. Among the many available fouling control

techniques, the addition of free-floating media into MBRs shows promise. Several media materials (e.g., polyurethane, polystyrene, polyethylene, activated carbon, zeolite, clay, polycaprolactone, etc.) have been tested in submerged MBRs and were reported to reduce membrane fouling significantly due to the continuous rubbing action of the moving media [5, 6]. Low-cost polyurethane sponges, in particular, present a reasonable mobile carrier in many MBR technologies due to their high porosity, which can immobilize microbes and remove nutrients, and their robust mechanical characteristics in the context of membrane scouring [7, 8].

The study presented here sought to design a rotary disk-assisted membrane system for efficiently controlling membrane fouling during anaerobic treatment (known as ARMBR for anaerobic rotary membrane reactor). Rotary filter and disk filtration systems have been successfully applied to a variety of systems, presumably by reducing cake buildup and membrane fouling by creating high shearing forces on the membrane surfaces using a rotating disk. A previous study [9] found that the use of a rotating disk reduced the concentration polarization and resulted in an order of magnitude improvement in yeast cell concentration. A report by Zhu et al. [10] showed that the combination of high shear stress and low trans-membrane pressure (TMP) introduced by the rotating disk in parallel with the membrane facilitated solute rejection by the membrane in a chicory juice extraction process. Rotary filtration systems are economically beneficial compared with conventional cross-flow filtration systems, as the improved permeability substantially reduces the number of modules and/or membrane areas used [11]. In addition to the intrinsic antifouling effects introduced by rotary disks, disk rotation can increase the shear force between the floating media and a membrane relative to the shear force produced using other supporting methods, such as gas sparging and pump recirculation. Thus, the filtration obtained by the simultaneous use of a rotating disk and supporting media into the MBR process would be expected to improve.

The present study tested the feasibility of using a rotary disk in an ARMBR. Short-term operational studies were performed to investigate the effects of scouring under the action of the rotating disk and the supporting media on membrane fouling. Rotational speed and media packing volume were varied in an effort to optimize the process. The stability of the ARMBR under long-term operation was evaluated both with and without a pretreatment step (pretreatment performed in an anaerobic expanded bioreactor, AEBR), resulting in two-stage AEBR-ARMBR or single-stage ARMBR processes.

Material and methods

The synthetic wastewater used in this study had a COD of 342.3 mg/L, a dissolved oxygen (DO) of 0.5 mg/L, an alkalinity of 192.9 mg·$CaCO_3$/L, an ammonium nitrogen (NH_4-N) of 19.3 mg/L, and an orthophosphate (PO_4-P) of 3.6 mg/L. The pH value was 7.4. Wastewater was continuously fed to the reactors using a peristaltic pump (Dongseo Science, Korea).

Figure 1 shows the schematic diagram and operation mode of the laboratory-scale AEBR and ARMBR systems under long-term operation. The 6 L AEBR (10 x 85 cm, D x H acrylic tube) contained a supporting media for microbial growth consisting of a 50% volume fraction polyurethane sponge (5 mm cube) with 97.9% voids

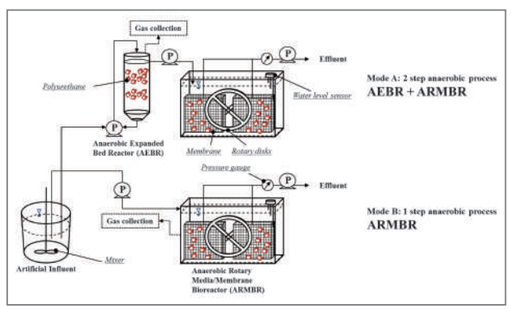

Figure 1. Process flow chart for anaerobic wastewater treatment in two-stage (mode A) and single-stage (mode B) MBR systems.

and an apparent density of 20 kg/m^3. The compression recovery was 97.7%. A peristaltic pump was used for wastewater recirculation to maintain the sponge expansion in the AEBR.

Four liters of ARMBR (30 x 6 x 30 cm, L x W x H) contained two submerged membrane modules, a polyurethane sponge and a rotary disk, as described in Figure 1. Polyethylene flat sheet membranes with a pore size of 0.2 μm and a membrane surface area of 0.03 m^2/module were attached to either side of the module. Two rotary disks (22 cm diameter) were rotated in parallel with the membrane surfaces on either side of each membrane module. The rotation speed of the rotary disks was controlled using a speed control motor (GGM Corp., Korea). A constant permeate flow was generated from the ARMBR by connecting two membrane modules to a peristaltic pump set to achieve the desired membrane flux. The peristaltic pump was operated intermittently, and the intermittent on/off ratio was 8 min/2 min. The TMP required to maintain the constant permeate flow was monitored using a pressure gauge and automatically acquired using a LabView system.

The AEBR and ARMBR systems were operated using a 5,500 ppm activated sludge mixed liquor suspended solids (MLSS). The operating temperatures of both the AEBR and ARMBR systems were maintained at 30°C in a temperature-controlled chamber.

During short-term operation, the variations of the TMP in the ARMBR were monitored to assess the effects of the disk rotation and the synergetic effects between the disk rotation and the media volume on the membrane fouling. During long-term operation, two different operation modes were implemented. The operating conditions are listed in detail in Table 1. Mode A (two stage AEBR-ARMBR system) purified the wastewater in series, first using AEBR and second using ARMBR. The wastewater was connected directly to the ARMBR without the AEBR in mode B (the single-ARMBR system). Any biogas produced during the AEBR (mode A) or ARMBR (mode B) was collected using a gas bag (DuPont Corp., USA).

The COD removal and gaseous methane production were analyzed during the long-term operation to estimate electricity consumption and system efficiency under different anaerobic treatment modes.

Results and discussion

Effect of rotational speed and media volume on membrane fouling in ARMBR

During the first short-term test, two membrane sponge bioreactors were tested to investigate the effects of the rotary disk on membrane fouling control. One test was initiated with a continuous rotation of the disk, and the other test involved disk rotation initiation after the TMP had reached 30 kPa (Figure 2). During disk rotation, the TMP was maintained below 5 kPa after 600 min operation, whereas the TMP reached 30 kPa within 100 min in the absence of rotation. After rotation had begun, however, the TMP decreased sharply to about 3

Table 1. Long-term operation in two anaerobic modes.

Long-term mode (100 days)	Mode A		Mode B
	AEBR	ARMBR	ARMBR
HRT (h)	3	6	6
Influent flow rate (L/d)	16	16	16
Membrane flux (LMH)	-	11	11
Recirculation flow rate (L/d)	1,008	-	-
Rotation speed (RPM)	-	70	70
Media volume fraction (%v/v)	50	25	25

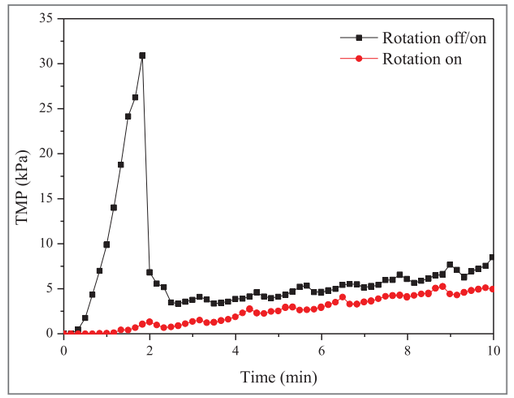

Figure 2. The effect of disk rotation on the TMP in an ARMBR. Conditions: rotation speed = 40 rpm, media volume = 30%, permeate flux = 12.5 LMH, and operation time = 6 h.

kPa within 40 min and then increased to 8 kPa after 10 h operation. Reduced membrane fouling mainly arose from the increase in the shear rate and the reduction in the concentration polarization on the membrane surface created by the disk rotation, in accordance with previous studies [12]. These results indicate that disk rotation methods can be applied successfully in MBR systems to reduce membrane fouling.

The designed ARMBR consisted of two membrane modules that were influenced by water flow in opposite directions. The diametrical direction of the water flow was generated using disk rotation parallel to the membrane surface, with an upward flow of water to one module and downward flow of water to the other module (Figure 3, inset). During the second short-term test, therefore, the filtration performances of the ARMBR modules were compared, and the relationship between the water flow direction and media was investigated (Figure 3). Without the addition of media, the average difference between the TMP values of the two modules was not significant (p>0.05), indicating that the permeabilities of the modules did not differ significantly, regardless of the water flow direction. The application of a 10% volume of media reduced the average TMPs at each module, regardless of the water flow direction. The use of media, however, increased the difference between the TMP values of the modules. The average TMP at a module in the upward flow region decreased significantly from 5.7 kPa to 1 kPa, whereas the average TMP at a module in the downward flow region showed a smaller reduction, from 7.5 kPa to 6.2 kPa. The TMP difference was confirmed using statistical analysis, with p<0.05. Lee et al. [6] reported that the extent of membrane fouling control in a MBR submerged in supporting media was substantially related to the potential collision energy between the media and the membrane surface. Collisions between the circulating media and the membranes introduced frictional forces that mitigated the cake layer on the outer surface of the membrane. The collision energy was proportional to the square of the moving media velocity. In the upward flow region, the directions of the disk rotation and media buoyancy were aligned so that the media moved faster than in the downward flow region, where the directions of the disk rotation and media buoyancy were opposed (Figure 3, inset). Consequently, the larger collision energy between the media and the membrane surface in the upward flow region enhanced the membrane's permeability. This study investigated only the relationship

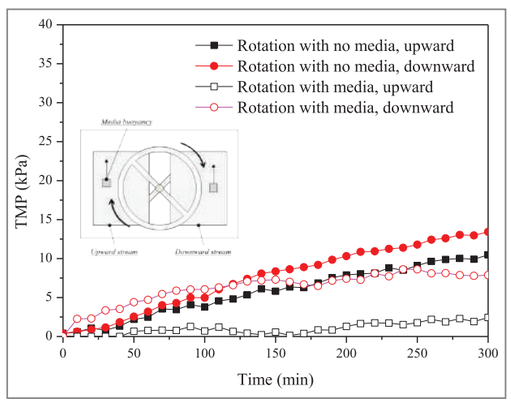

Figure 3. TMP variations of each filter module in the ARMBR. Conditions: rotation speed = 50 rpm, media volume = 10%, permeate flux = 15 LMH, and operation time = 6 h.

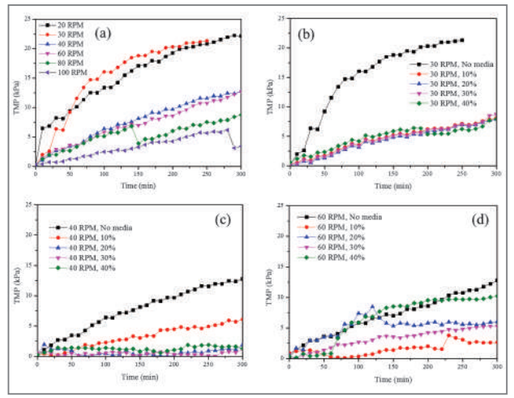

Figure 4. TMP variation with different rotation speed and media volume fraction in ARMBR: no media at different rotation speeds (a), different media volumes at 30 rpm (b), 40 rpm (c) and 60 rpm (d). Conditions: rotational speed = 20–100 rpm, media volume fraction = 0–40%, permeate flux = 15 LMH and operation time = 6 h.

between the low density-sponge media and the water flow direction. Additional research is needed to assess the relationship between the direction of the water flow and the various characteristics of the supporting materials, such as density, size, and shape on membrane fouling control.

A last short-term test was conducted to vary the rotational speed and media volume fraction in an effort to investigate the synergetic scouring effects of these parameters. The rotation speed was adjusted over the range 20–100 RPM, and the media volume fraction was adjusted over the range 0–40%. The average TMP values and the TMP variations during each 3 h operation session are presented in Figure 4. Without media, membrane fouling could be reduced by increasing rotation speed; however, control over membrane fouling was more effective when the media and rotation were employed simultaneously. At a rotation of 30–60 RPM, the TMP was reduced by 8–95% using a 10–40% media volume fraction. The presence of media could apparently be accompanied by a reduction in the applied disk rotation speed, and the presence of supporting media could reduce energy consumption associated with disk rotation. At a disk rotation speed of 30 RPM, the TMP was reduced from 14.9 to 4.6 kPa when 10% (v/v) supporting media was added. However, addition of media at higher dosages (20–40%) failed to improve the membrane permeability further. The efficient circulation of low-density media along the membrane surface requires that the driving force generated by the disk rotation outweigh the buoyancy of the media. At this rotation speed, however, efficient media circulation was difficult because the rotating disk did not impose a significant driving force for circulation. At a disk rotation speed of 40 RPM, synergetic effects were observed with the media volume. Increasing the media volume from 10 to 30% significantly enhanced membrane permeability from 58 to 94%, compared to the process conducted without added media. Further additions of media (to a 40% packing volume) only slightly increased the TMP. At a disk rotation of 60 RPM, a 10% media volume provided the greatest reduction in membrane fouling. A greater media volume failed to control the extent of membrane fouling. The increased TMP values may have resulted from the restrictions on the free circulation of media due to an excessive media packing density. Two-way ANOVA analysis was conducted to confirm the scouring effects of the disk rotation (20–100 RPM) and media volume (0–40%) for promoting membrane fouling control. Each fouling control method significantly reduced (p<0.05) the membrane fouling. A p-value of 0.016 was obtained for the disk rotation effects, and a p-value of 0.018 was obtained for the media packing volume effects.

Comparison between AEBR-ARMBR and single ARMBR in anaerobic wastewater treatment

Performance of the ARMBR under long-term operation was examined using two different operational modes. The first mode involved a pretreatment step (mode A, AEBR-ARMBR) and the second mode did not (mode B, ARMBR alone). The two modes were tested over a 100-day operational session (Table 2). Both modes A and B performed satisfactorily for organic removal, resulting in a

Table 2. Performance of different operational modes A and B.

			Mode A					Mode B	
			AEBR		ARMBR			ARMBR	
	n	Influent	Effluent	Removal (%)	Effluent	Removal (%)	Total Removal (%)	Effluent	Removal (%)
COD (mg/L)	16	342.9±17.4	42.2±18.2	87.7±5.3	12.5±2.9	66.6±12.4	96.3±0.9	12.5±3	96.3±0.9
CH_4 composition (%)	15		58.6±8.7					68±4.6	
CH_4 production yield ($L\cdot CH_4/g\cdot COD$)	15		0.141±0.024					0.15±0.029	

96.3% COD removal. In mode A, only a negligible fraction of gaseous methane was produced, as the COD loading obtained from AEBR was low. The gaseous methane was, therefore, collected from the AEBR in mode A. The gaseous methane composition was 13% higher and the production yield was 12% higher in mode B than in mode A. The HRT was twice as long and the COD removal was 9% greater in the ARMBR of mode B than in mode A, leading to enhanced gaseous methane generation, as opposed to the AEBR operated in mode A. The single ARMBR process was found to be superior to the two-stage process in terms of organic removal and energy production, considering the simple configuration of the single system.

In addition to COD removal and gaseous methane production, TMP variations in the ARMBRs operated in modes A and B were monitored (Figure 5). Unfortunately, the TMP values from days 0–4 and 10–25 were lost due to a malfunction in the data logging system; however, the TMP values generated within the initial and final lost periods displayed a discernable trend. During the 100 day treatment period, the TMP of the ARMBR operated

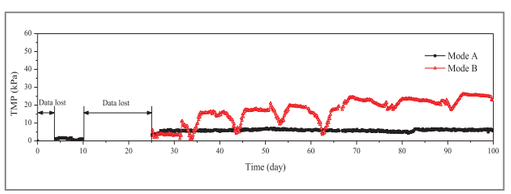

Figure 5. Variation of the TMPs of the ARMBR in modes A and B.

in mode A stabilized at 5 kPa, whereas the TMP of the ARMBR operated in mode B gradually increased and reached 23 kPa. Possibly due to the low organic loading from the AEBR operated in mode A, the cake layer formation on the membrane was substantially reduced in the ARMBR, in agreement with a previous report that found that the coupling of a fluidized bed reactor with a membrane reactor could potentially reduce membrane fouling [13]. Although no additional cleaning methods were applied to either of the ARMBRs operated in modes A or B over the 100 days of operation, the designated permeate flux was maintained. Consequently, stable long-term operation could be achieved in a single-ARMBR system (mode B) due to effective membrane control through the synergetic action of the disk rotation and the media even without a pretreatment step and periodic cleanings.

Electrical energy balance

Figure 6 plots the electrical energy requirements and production profiles in modes A and B. Positive values indicate the energy requirements for operating the reactors and negative values indicate energy gains from methane combustion. The electrical energy needs for operating the rotating and pumping equipment were calculated according to the methods of Fukukawa et al. [14] and Kim et al. [13], respectively. The calculated total required electricity was 0.112 kWh/m^3 for mode A and 0.104 kWh/m^3 for mode B. Only 0.013 kWh/m^3 of electrical energy was required to circulate the media in

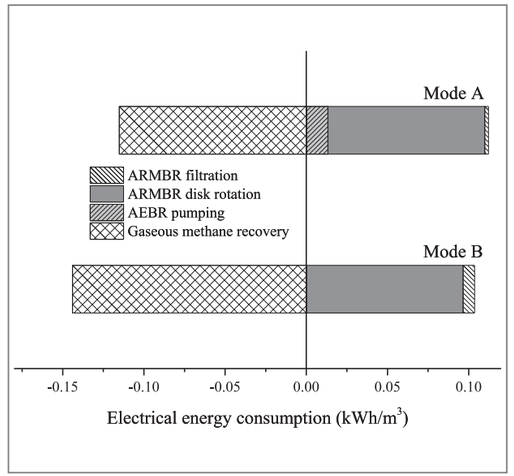

Figure 6. Energy balance of the anaerobic systems operated in modes A and B.

the AEBR. The AEBR pretreatment process of mode A required about 8% more electrical energy than mode B. The most significant electricity requirement was imposed by the disk rotation in the ARMBR, constituting 86.06% or 93.18% of the total required energy in modes A or B, respectively. The higher-than-average TMP measured in mode B increased the electrical energy needed for filtration by a factor of three relative to the electrical energy needed in mode A: 0.002 kWh/m^3 in mode A and 0.007 kWh/m^3 in mode B. The proportion of energy required for filtration, however, was small. Thus, the higher TMP in mode B did not significantly impact the economic viability of the total system.

The gaseous methane produced during anaerobic treatment could be converted into electrical energy, thereby offsetting the electricity consumed during operation of the anaerobic reactor. The methane energy conversion calculation used in this study is described in detail in [13]. The electrical energy obtained from gaseous methane combustion was 0.115 kWh/m^3 in mode A and 0.144 kWh/m^3 in mode B. The gaseous methane energy produced outweighed the electricity needs for the operating modes, yielding an excess of 0.003 kWh/m^3 and 0.04 kWh/m^3 during anaerobic operation in modes A and B, respectively. This total electrical energy balance of ARMBR was slightly lower compared to that reported by previous studies [13, 15]. However, lower material and operating costs resulting from no membrane and media replacement during ARMBR operation were able to compensate for the lower electricity balance of the system. Moreover, further optimization of the developed MBR system may be able to reduce this energy utilization.

Although this study used synthetic wastewater, sufficient levels of stable operation and electrical energy balance were obtained. These results collectively indicate that the anti-fouling strategy developed in this study may prove useful for effectively reducing the membrane fouling while treating real wastewater.

Conclusion

This study examined the performance properties of a rotary disk-equipped submerged MBR. In addition to the disk rotation, a sponge was used to sustain microbial growth as well as control membrane fouling. The scouring action caused by the simultaneous disk rotation and sponge media in the ARMBR successfully replaced the need for any other fouling control technique. This result supported the hypothesis that enhanced shear force and mass transfer of media due to disk rotation could alleviate membrane fouling in a MBR. The results also confirmed that a rotary disk was beneficial for balancing the electrical energy in a MBR.

Note

This article and images are drawn from “Membrane fouling control using a rotary disk in a submerged anaerobic membrane sponge bioreactor” in *Bioresource Technology*, Vol. 172, pp. 321–327, 2014.

References

[1] Sutton PM, Rittmann BE, Schraa OJ, Banaszak JE, Togna AP. *Water Sci Technol.* 2011; 63: 2004-2009.

[2] Park JBK, Craggs RJ. *Water Sci Technol.* 2007; 55: 257-264.

[3] Ueda T, Hata K, Kikuoka Y, Seino O. *Water Res.* 1997; 31: 489-494.

[4] Ngo HH, Guo W, Xing W. *Bioresour Technol.* 2008; 99: 2429-2435.

[5] Khan SJ, Zohaib-Ur-Rehman, Visvanathan C, Jegatheesan V. *Bioresour Technol.* 2012; 113: 161-164.

[6] Lee WN, Kang IJ, Lee CH. *Water Res.* 2006; 40: 1827-1835.

[7] Chu L, Wang J. *Chemosphere* 2011; 83: 63-68.

[8] Guo W, Ngo HH, Palmer CG, Xing W, Hu AYJ, Listowski A. *Desalination* 2009; 249: 672-676.

[9] Jaffrin MY, Ding LH, Akoum O, Brou A. *J Membrane Sci.* 2004; 242: 155-167.

[10] Zhu Z, Ladeg S, Ding L, Bals O, Moulai-Mostefa N, Jaffrin MY, Vorobiev E. *Ind Crop Prod.* 2014; 53: 154-162.

[11] Ríos SD, Salvadó J, Farrio X, Torras C. *Bioresour Technol.* 2012; 119: 406-418.

[12] Jaffrin MY. *Curr Opin Chem Eng.* 2012; 1: 171-177.

[13] Kim J, Kim K, Ye H, Lee E, Shin C, Mccarty PL, Bae J. *Environ Sci Technol.* 2011; 45: 576-581.

[14] Fukukawa H, Kato Y, Inoue Y, Kato T, Tada Y, Hashimoto S. *Int. J. Chem. Eng.* 2012.

[15] Yoo R, Kim J, McCarty PL, Bae J. *Bioresour Technol.* 2012; 120: 133-139.

[**Feature Articles**]

The Metabolic Shift Driven by Electricity in Electroactive Heterotroph *Clostridium Pasteurianum*

Okkyoung Choi

Department of Chemical Engineering, Department of Fuel Cells and Hydrogen Technology, Hanyang University

okgii77@hanyang.ac.kr

Youngsoon Um

Clean Energy Research Center

yum@kist.re.kr

Introduction

The focus of this article is on KIST's efforts in investigating renewable energy, and specifically, how electricity can be used to generate biofuel. The biofuels most commonly used today as alternatives to fossil fuels are ethanol and butanol, which are produced from chemical reduction processes associated with acetic acid and butyric acid. When reductions occur through microbial metabolic processes, the more electrons/carbon that flow into biofuel production, the greater the production of reduced compounds. In prior research, extra reducing power has been supplied

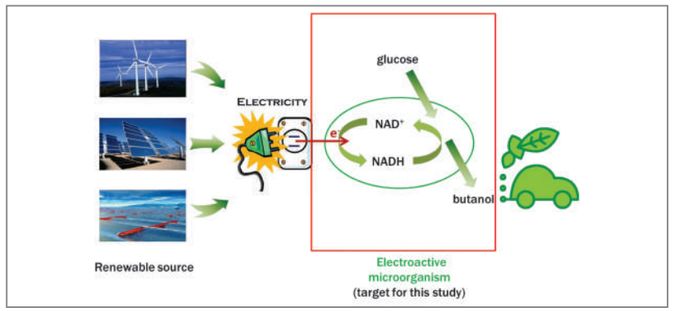

Figure 1. Overview of electricity-driven metabolic shift. Electricity is stored as chemical compounds. The electroactive microorganism directly accepts electrons from a cathode and produces more butanol.

through various methods such as adding more reduced chemicals to substrate [1, 2] or modifying pathways through metabolic engineering [3, 4]. The investigations presented here demonstrate that electricity can change microbial pathways, thereby increasing reduced products, specifically, butanol and 1, 3-propandiol. The discussion which follows shows how electroactive heterotrophic microbes accepted extracellular electrons directly from a cathode and used these electrons as a reducing power to generate butanol (Figure 1).

Clostridium pasteurianum directly accepts electrons from a cathode

We found that *Clostridium pasteurianum,* a butanol-producing bacteria, could directly accept electrons from a cathode without any mediator. *C. pasteurianum* DSM 525 showed a significant electroactivity with definite redox peaks in cyclic voltammetry (CV) analysis using a glassy carbon electrode. No redox reactions were found when CV was analyzed with fresh medium and cell-free culture supernatant (spent medium) using a sterilized graphite felt electrode, implying the absence of electroactive components in the supernatant (Figure 2).

Biofilm cells of *C. pasteurianum* on the cathode poised at +0.045 V vs. SHE were observed through SEM analysis, and it was found that *C. pasteurianum* DSM 525 cells stacked with each other on the cathode (Figure 3). Extracellular appendages were shown only in the biocathode of the bioelectrochemical system (BES), not in the graphite felt of the control culture (open circuit). Although the role of the extracellular appendages observed in the biocathode could not be elucidated from the SEM images alone, it is likely that the BES caused significant changes in the extracellular structure of *C. pasteurianum* DSM 525 attached on the cathode. Further characterization of *C. pasteurianum* DSM 525 cells in the BES would help clarify the interaction between the cathode and cells involved in direct electron transfer.

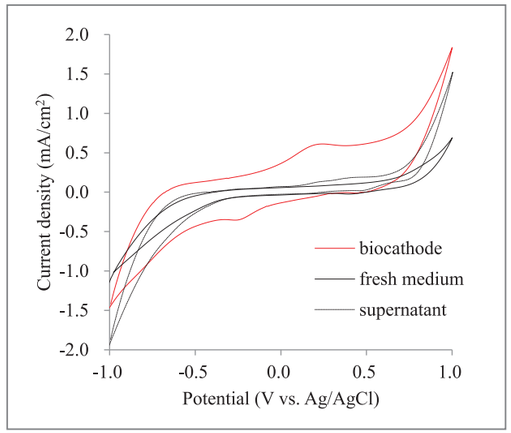

Figure 2. The cyclic voltammetry (CV) study. The CV of electroactive cells (biofilm on the cathode and suspended culture) cultivated for 8 hours in the cathode compartment under the potential +0.045 V vs. SHE. The scanning rate was 50 mV/s and Ag/AgCl was used as the reference electrode. The biocathode was the working electrode.

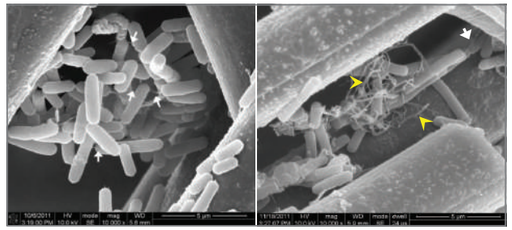

Figure 3. The scanning electron microscopy (SEM) images of the graphite felt cathode surfaces poised at +0.045 V vs. SHE. White arrows indicate short and thin nano-filamentous appendages. Yellow arrow-heads indicate long and thicker appendages.

Electron uptake by *C. pasteurianum* increases butanol production from glucose

Because *C. pasteurianum* accepted electrons from a poised electrode, we hypothesized that microbial electron uptake might induce the production of more reduced products from glucose with consuming electrons. To check the change in fermentation behavior, cell growth and product concentrations were

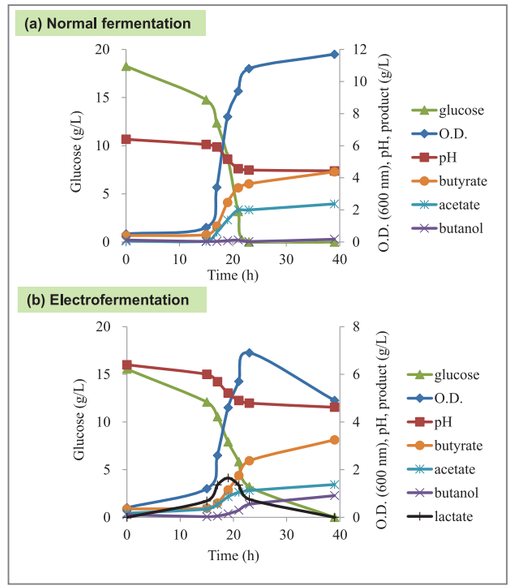

Figure 4. Time profile of (a) glucose fermentation and (b) electrofermentation. One representative result out of 11 replicate experiments is shown. Current consumption increased with microbial growth but decreased at the end of the stationary phase with cell lysis.

analyzed in both a control (without electricity) (Figure 4a) and electrochemically driven system (Figure 4b). Unexpectedly, lactate was produced in the exponential phase, at the expense of acetate and butyrate, only under the BES. Butanol production started to increase when lactate uptake was initiated (Figure 4b). Interestingly, the increase of butanol production (10.1 mM) after 20 hours of cultivation was roughly half of the consumed lactate (18.3 mM). Because 2 moles of lactate can be stoichiometrically converted to 1 mol of butanol through microbial metabolism, most of the increased butanol production in the BES was likely attributable to lactate consumption. Overall, butanol production increased (2.1 vs. 12.2 mM) and acid production decreased (49.7 vs. 36.9 mM in butyric acid; 39.6 vs. 22.9 mM in acetic acid) in the presence of electricity. The pH change in the control was not much different from that in the BES, whereas O.D. decreased suddenly during the stationary phase in the BES. Cell disruption has been reported in *Enterobacter* exposed to weak electricity (10 mA) [5] and in *C. tyrobutyricum* under a mediated BES [6]. There was no significant difference in gas composition between the control and BES (H_2/CO_2=1.09 in the control and 1.10 in the BES), indicating little concern to electrochemical hydrogen production. The potential applied in this study (+0.045 V vs. SHE) was far higher than the electrochemical hydrogen production potential (-0.41~ -0.27 V vs. SHE at pH range 4.5 ~ 7.0), which also supports little abiotic hydrogen production in this BES system.

C. pasteurianum shows current consumption-dependent final product distribution in glycerol fermentation

Unlike other butanol-producing clostridia species, *C. pasteurianum* is able to use glycerol as a sole carbon source and produce butanol and 1,3-PD as main products [7]. Considering that glycerol (4.7 e^- equivalent/C-glycerol) is a more reduced carbon source than glucose (4 e^- equivalent/C-glucose), *C. pasteurianum* in glycerol fermentation is capable of efficiently balancing the intracellular NADH/NAD^+ ratio by actively producing reduced metabolites such as 1,3-PD (net NADH-consuming) and butanol (net NADH-neutral in glycerol fermentation). This is different from glucose fermentation, in which the favorable metabolic pathway is butyric acid production (net NADH-neutral), not butanol production (net NADH-consuming). To investigate whether an active NADH-consuming metabolism during glycerol fermentation would affect current consumption and product profiles, the BES batch, supplemented with glycerol as a carbon source, was repeated with the remaining bioelectrode in the cathode compartment. Glycerol (250~300 mM) was completely consumed after 48 hours of cultivation during the repeated batches

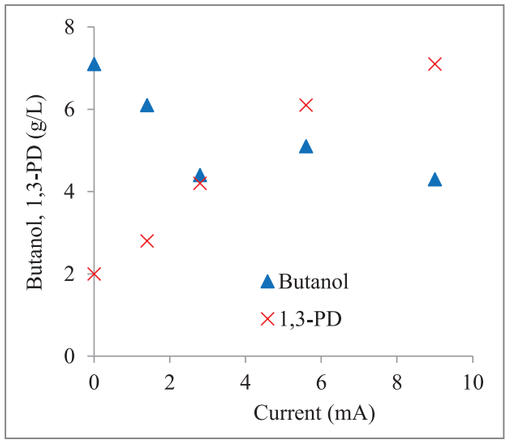

Figure 5. The current-dependent main product shift from butanol to 1, 3-PD in glycerol electrofermentation. The current was recorded at the stationary phase with maximum value and the concentration of product was the final concentration when 30 g/L glycerol was completely consumed.

and electron consumption increased to 9 mA in the 3rd~4th batches, a level higher than that with repeated BES batches with glucose (5 mA) (Figure 5). Of interest was that a higher current consumption resulted in more 1, 3-PD production and a shift of the major product from butanol to 1, 3-PD. This result implies that more current consumption can induce the metabolic pathway to produce a more net NADH-consuming compound (1, 3-PD) in glycerol fermentation. Final product distribution was current consumption-dependent in glycerol fermentation, supporting the idea that an electricity-driven metabolic pathway shift occurred in *C. pasteurianum* under the BES to produce more reduced compounds (net NADH-consuming compounds).

Small amount of electron uptake significantly stimulates NADH-consuming metabolism

Because cathodic electrons are supposed to be utilized as co-reducing equivalents, we compared reducing equivalent (NADH and cathodic electrons) flow from electron donors (carbon source and cathode) to final products in a control and in the BES; we investigated how cathodic electrons affected intracellular redox reactions. The electron consumption in the BES was 1.51 e^- mmol (equivalent to 0.8 mmol NADH) during glucose electrofermentation. Surprisingly, this electricity-derived NADH generation was only 1.5% of glucose-derived NADH generation (Figure 6a). In glycerol fermentation, the electricity-derived NADH, theoretically calculated from the electron consumption (4.96 e- mmol), was also only 2.3% of the glycerol-derived NADH (Figure 6b). This indicates that NADH generation from glucose and glycerol accounted for most of NADH in the BES; however, even a small amount of electricity significantly changed the metabolism toward net NADH-consuming compounds. Interestingly, NADH consumption in the BES increased more than the amount of electron-derived NADH. Because the amount of electricity-derived NADH was far smaller that of the substrate-derived NADH, a higher portion of NADH consumption out of NADH generation in the BES (Figure 6) is likely attributable to not only the utilization of cathodic electrons as additional reducing equivalents but also to the significant stimulation

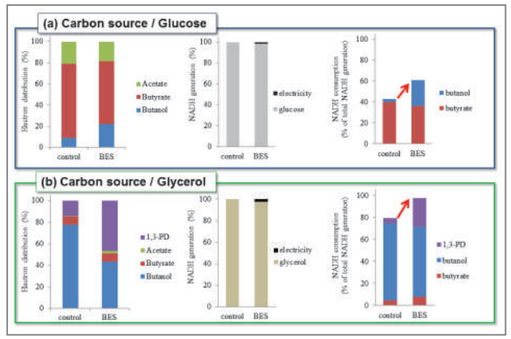

Figure 6. The electron distribution of products and the NADH distribution for generation/consumption with (a) glucose and (b) glycerol fermentation.

of carbon source-derived NADH consumption toward the production of more reduced compounds by cathodic electrons.

Conclusion

Our research has demonstrated that *Clostridium pasteurianum* DSM 525 simultaneously utilizes both cathode and substrate as electron donors through direct electron transfer. In a cathode compartment poised at +0.045 V vs. SHE, a metabolic shift in *C. pasteurianum* occurs toward NADH-consuming metabolite production such as butanol from glucose (20% shift in terms of NADH consumption) and 1,3-propandiol from glycerol (21% shift in terms of NADH consumption). Notably, a small amount of electron uptake significantly induces NADH-consuming pathways over the stoichiometric contribution of the electrons as reducing equivalents. Our results demonstrate a previously unknown electroactivity and metabolic shift in the biochemical-producing heterotroph, opening up the possibility of efficient and enhanced production of electron-dense metabolites using electricity.

Note

This article and images are drawn from “Electricity-driven metabolic shift through direct electron uptake by electroactive heterotroph *Clostridium pasteurianum*” in *Sci. Rep.* 4: 6961.

References

[1] Abbad-Andaloussi S, Amine J, Gerard P, Petitdemange H. *J. Appl. Microbiol.* 1998; 84(4): 515-522.
[2] Jin P, Lu SG, Huang H, Luo F, Li S. *Appl Biochem Biotechnol.* 2011; 165(7-8): 1532-1542.
[3] Flynn JM, Ross DE, Hunt KA, Bond DR, Gralnick JA. *mBio.* 2010; 1(5).
[4] Pandit AV, Mahadevan R. *Microb Cell Fact.* 2011; 10: 76.
[5] She P, Song B, Xing XH, van Loosdrecht M, Liu Z. *Biochem Eng J.* 2006; 28(1): 23-29.
[6] Choi O, Um Y, Sang BI. *Biotechnol Bioeng.* 2012; 109: 2494-2502.
[7] Moon C, Lee CH, Sang BI, Um Y. *Bioresour Technol.* 2011; 102(22): 10561-10568.

Correlations of amyloid-b concentrations between CSF and plasma in an acute Alzheimer mouse model

Scientific Reports
2014 Oct. / Vol. 4 / 6777-1 ~ 6777-4

Soo Min Cho, Hyunjin Vincent Kim, Sejin Lee, Hye Yun Kim, Woong Kim, Tae Song Kim, Dong Jin Kim & Young Soo Kim
yskim@bio.kist.re.kr

Amyloid-b (Ab) is one of the few neuropathological biomarkers associated with transporters of the blood-brain barrier (BBB). Despite the well-characterized clinical indication of decreasing Ab levels in the cerebrospinal fluid (CSF) during the development of Alzheimer's disease (AD), the link between the alternation of Ab level in the blood and the progress of the disorder is still controversial. Here, we report a direct correlation of Ab(1–42) levels between CSF and plasma in an AD mouse model. We injected monomeric Ab(1–42) directly into the intracerebroventricular (ICV) region of normal adult mouse brains to induce AD-like phenotypes. Using sandwich enzyme-linked immunosorbent assays, we observed proportional elevation of Ab(1–42) levels in both CSF and plasma in a dose-dependent manner. Our findings that plasma Ab(1–42) reflects the condition of CSF Ab(1–42) warrant further investigation as a biomarker for the blood diagnosis of AD.

Echogenic nanoparticles for ultrasound technologies: evolution from diagnostic imaging modality to multimodal theranostic agent

Nano Today
2014 Aug. / Vol. 9 No. 4 / 525 ~ 540

Sejin Sona, Hyun Su Min, Dong Gil You, Beob Soo Kim, Ick Chan Kwon
ikwon@kist.re.kr

Ultrasound technology in combination with echogenic particles is currently having a considerable effect on the modern medical field, not only as a conventional diagnostic modality, but also as a methodology for administering therapeutics to various types of lesions. The diagnostic and therapeutic effects of ultrasound technologies on diseased sites are governed by several primary factors, such as the ultrasound technique itself and the physicochemical properties of echogenic particles. Therefore, rational design and a good combination of echogenic particles with the ultrasound technique are the most decisive factors in achieving optimal diagnostic and therapeutic goals. Great strides have been made in the design and engineering of echogenic particles to meet diagnostic and therapeutic demands. Since echogenic particles exhibit quite different behaviors in response to ultrasound, the most important issue in achieving maximal therapeutic efficacy must be the establishment of technical rationales that depend on these particles' biomedical uses, from the selection of shell materials and gas types to the manufacturing techniques used to make particles of the proper diameter. Several attempts have been made to develop highly effective theranostic echogenic particles that have the proper particle size and yet can sustain intense echo signals for long enough to circulate repeatedly through the body, a primary requirement for targeting and accumulating at a diseased site. However, a very important challenge has been to obtain the most favorable *in vivo* nano-size for desirable biodistribution while ensuring a strong echo intensity.

In this review paper, the present status of research and the critical issues for developing theranostic echogenic particles as an ultrasound contrast agent and drug delivery vehicle are described. Firstly, a comprehensive introduction to conventional micro-sized echogenic particles is given with respect to their research history, diagnostic applications and intrinsic limitations. Then, recent progress in developing more advanced echogenic particles for diagnostic and therapeutic purposes is described. Most importantly in this paper, design criteria are given for developing promising theranostic echogenic particles to satisfy research needs and clinical demands, with special emphasis on overcoming the conflicting and insuperable size issue of echogenic particles.

Nonvolatile resistance switching on two-dimensional electron gas

ACS Applied Materials & Interfaces
2014 Sep. / Vol. 6 / 17785 ~ 17791

Jin Gwan Joung, Shin-Ik Kim, Seon Young Moon, Dai-Hong Kim, Hyo Jin Gwon, Seong-Hyeon Hong, Hye Jung Chang, Jin-Ha Hwang, Beom Jin Kwon, Seong Keun Kim, Ji-Won Choi, Seok-Jin Yoon, Chong-Yun Kang, Kwang Soo Yoo, Jin-Sang Kim, and Seung-Hyub Baek
shbaek77@kist.re.kr

Two-dimensional electron gas (2DEG) at complex oxide interfaces has generated considerable interest for application in next-generation multifunctional oxide electronics due to the exotic properties that do not exist in bulk. In this study, we report the integration of 2DEG into a nonvolatile resistance switching cell used as a bottom electrode, where the metal–insulator transition of 2DEG by an external field serves to significantly reduce the OFF-state leakage current while enhancing the on/off ratio. Using a Pt/Ta2O5–y/Ta2O5–x/SrTiO3 heterostructure as a model system, we demonstrate a nonvolatile resistance switching memory cell with a large on/off ratio (>106) and a low leakage current at the OFF state (~10–13 A). Beyond exploring nonvolatile memory, our work also provides an excellent framework for enhancing the fundamental understanding of novel physics in which electronic and ionic processes are coupled in complex heterostructures.

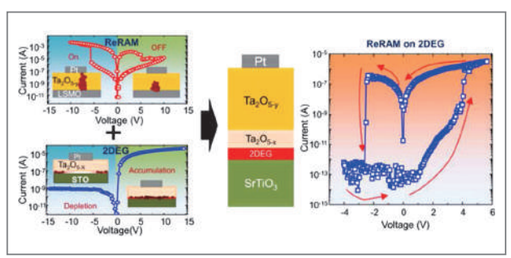

Highly sensitive immunoassay for the diagnosis of acute myocardial infarction using silica spheres encapsulating a quantum dot layer

Analytical Chemistry
2014 Oct. / Vol. 86 / 10157 ~ 10163

Hyojeong Han, Jae-Chul Pyun, Hyein Yoo, Hong Seog Seo, Byung Hwa Jung, Young Sook Yoo, Kyoungja Woo, and Min-Jung Kang
kjwoo@kist.re.kr

Commercial ELISA kits for substance P (SubP), which are helpful for the clinical diagnosis of acute myocardial infarction, are limited in efficacy because of low sensitivity. A highly sensitive immunoassay was developed using silica spheres encapsulating a quantum dot-layer (SQS) and labeling antibodies, on a Parylene A-modified plate. The high sensitivity was possible by taking advantage of the enhanced photoluminescence of the SQS and dense immobilization of SubP on the Parylene A-modified plate. Glutaraldehyde was used for cross-linking SQS to the anti-SubP antibody and SubP to the Parylene A coating. The SQS-linked immunosorbent assay (SQSLISA) was optimized and validated. The dynamic range for the assay was 1–10000 pg/mL with a linear correlation factor of 0.9992 when the competitive SQSLISA was employed. The intra- and interday accuracies were 93–100% and 87–122%, respectively. Reproducibility was lower than 11%. The developed method was applied to clinical samples collected from healthy controls (n = 30) and patients with acute myocardial infarction (n =16). It displayed a high correlation with a commercial ELISA kit, with a limit of detection that was 30-fold lower. Clinical sample analysis confirmed that SubP is a promising diagnostic marker for acute myocardial infarction. The SQSLISA is expected to be a practical and useful assay tool.

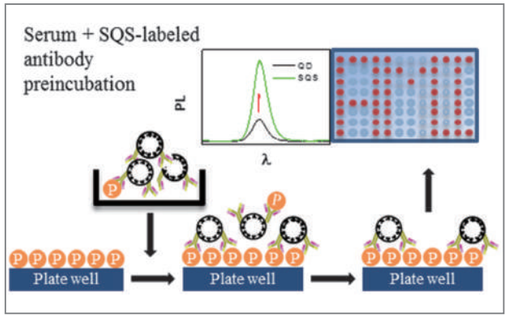

Controlling the intercalation chemistry to design high-performance dual-salt hybrid rechargeable batteries

Journal of the American Chemical Society
2014 Nov. / Vol. 136 No. 46 / 16116 ~ 16119

Jae-Hyun Cho, Muratahan Aykol, Soo Kim, Jung-Hoon Ha, C. Wolverton, Kyung Yoon Chung, Kwang-Bum Kim, and Byung-Won Cho
kychung@kist.re.kr

We have conducted extensive theoretical and experimental investigations to unravel the origin of the electrochemical properties of hybrid Mg2+/Li+ rechargeable batteries at the atomistic and macroscopic levels. By revealing the thermodynamics of Mg2+ and Li+ co-insertion into the Mo6S8 cathode host using density functional theory calculations, we show that there is a threshold Li+ activity for the pristine Mo6S8 cathode to prefer lithiation instead of magnesiation. By precisely controlling the insertion chemistry using a dual-salt electrolyte, we have enabled ultrafast discharge of our battery by achieving 93.6% capacity retention at 20 C and 87.5% at 30 C, respectively, at room temperature.

Competition between charge transport and energy barrier in injection-limited metal/quantum dot nanocrystal contacts

Chemistry of Materials
2014 Oct. / Vol. 26 / 6393 ~ 6400

Youngjun Kim, Seongeun Cho, Sunho Jeong, Doo-Hyun Ko, Hyungduk Ko, Namho You, Mincheol Chang, Elsa Reichmanis, Jun-Young Park, Sung Young Park, Jong Suk Lee, Heesun Yang, Insik In, and Byoungnam Park
jong.lee@kist.re.kr

Injection-limited contacts in many electronic devices, such as light-emitting diodes (LEDs) and field effect transistors (FETs), are not easily avoided. We demonstrate that charge injection in the injection-limited contact is determined by charge transport properties as well as the charge injection energy barrier due to vacuum energy level alignment. Interestingly, injection-limited contact properties were observed at 5 nm diameter lead sulfide (PbS) quantum dot (QD)/Au contacts for which carrier injection is predicted to be energetically favorable. To probe the effect of charge transport properties on carrier injection, the electrical channel resistance of PbS nanocrystal (NC) FETs was varied through thermal annealing, photoillumination, ligand exchange, surface treatment of the gate dielectric, and use of different sized PbS NCs. Injection current through the PbS/Au contact varied with the FET mobility of PbS NC films consistent with a theoretical prediction where the net injection current is dominated by carrier mobility. This result suggests that the charge transport properties, that is, mobility, of QD NC films should be considered as a means to enhance carrier injection along with the vacuum level energy alignment at the interface between QD NCs and metal electrodes. Photocurrent microscopic images of the PbS/Au contact demonstrate the presence of a built-in potential in a two-dimensionally continuous PbS film near the metal electrodes.

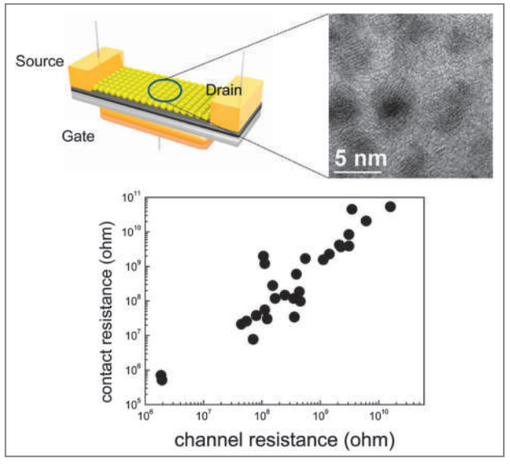

Method of preparing tetrabenazine and dihydrotetrabenazine

US 8993766 (2015.03.31)

Sun Joon Min / sjmin@kist.re.kr

The present invention relates to a method for preparing tetrabenazine (TBZ) and dihydrotetrabenazine (DTBZ), and more specifically, to a method for preparing tetrabenazine (TBZ) and dihydrotetrabenazine (DTBZ) by using simple and short reaction processes of using 6,7-dimethoxy-1,2,3,4-tetrahydroisoquinoline and 4-methyl-2-(3-(trimethylsilyl)prop-1-ene-2-yl)pentane as starting materials to sequentially perform an alkylation reaction, an Aza-Prins cyclization reaction in the presence of an oxidant and an oxidation reaction.

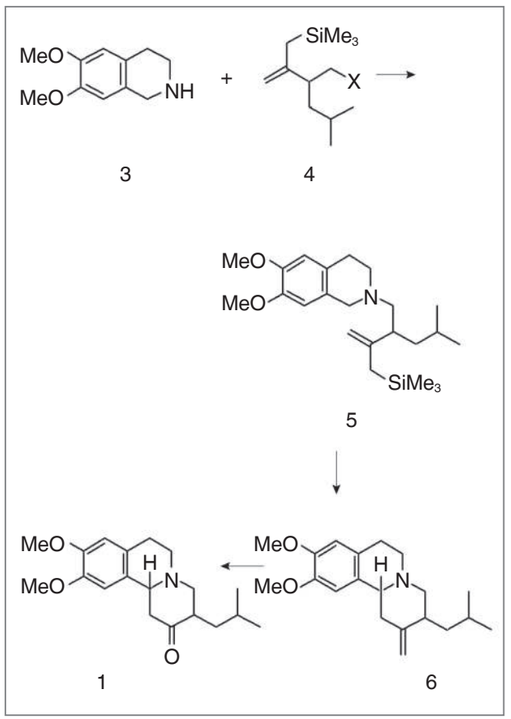

Apparatus and method for alternative aeration-effluent wastewater treatment using ceramic membrane

US 8980090 (2015.03.17)

Yong Su Choi / yschoi@kist.re.kr

Disclosed are an apparatus and method for alternative aeration-effluent wastewater treatment using a ceramic membrane, which allows biological treatment to be sufficiently performed in an intermittent aeration tank by combining an anaerobic tank with a plurality of intermittent aeration tanks and selectively changing an inflow path of influent water according to the operation status of the intermittent aeration tanks. The present disclosure is directed to providing an apparatus and method for alternative aeration-effluent wastewater treatment, which allows the aeration and treated water to continuously discharge through two intermittent aeration tanks by independently forming an air injection line and a treated water discharge line at a ceramic membrane provided in each intermittent aeration tank.

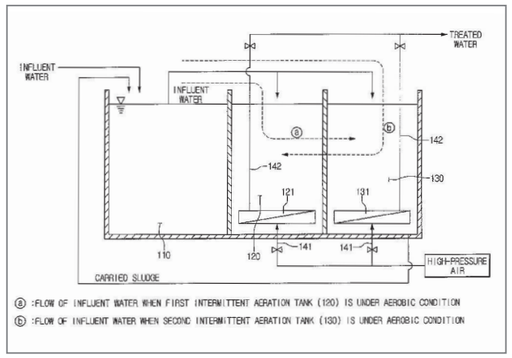

Method for producing renewable fuel using supercritical fluid

US 8968425 (2015.03.03)

Jong Min Park / ppjj@kist.re.kr

Disclosed is a method for producing a renewable fuel using a supercritical fluid. The method includes charging a supported catalyst into a continuous reactor and adding a catalyst activating material thereto to activate the supported catalyst, feeding an oil or fat, hydrogen and a supercritical fluid into the continuous reactor and allowing hydrogenation and hydrodeoxygenation reactions of the oil or fat in the supercritical fluid to proceed, and collecting a renewable fuel as the reaction product. The method enables the production of an oxygen-free renewable fuel in a higher yield at a lower hydrogen pressure and a lower reaction temperature than conventional methods for producing renewable fuels.

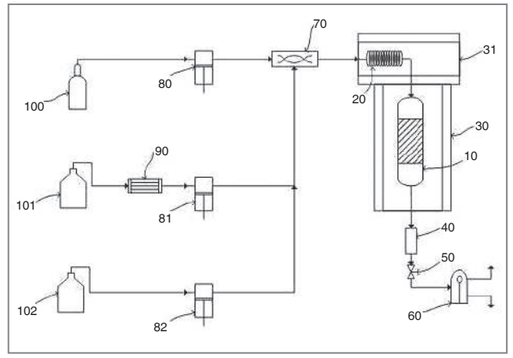

System and method for implementing 3-dimensional user interface

US 8963834 (2015.02.24)

Myoung Soo Park / meister@kist.re.kr

A system for implementing a 3-dimensional (3D) user interface includes an input device configured to collect position and normal direction information of a plurality of points located on a 3D object, a calculation device configured to process the position and normal direction information collected by the input device, and an output device configured to output a 3D virtual space set by the calculation device. The calculation device processes the position and normal direction information of the plurality of points, sets a plurality of virtual points corresponding to the plurality of points in the virtual space, and forms a 3D selection region including the plurality of virtual points in the virtual space, and the shape of the selection region is changed in correspondence with the change in the position and normal direction of the plurality of virtual points according to shape change of the 3D object.

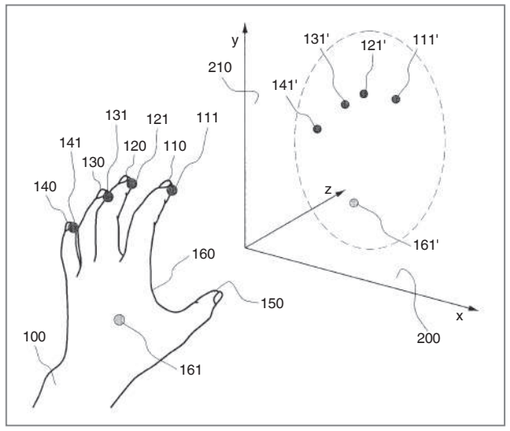

Recombinant protein for intracellular delivery of siRNA and composition comprising the same

US 8957186 (2015.02.17)

Hyung Jun Ahn / hjahn@kist.re.kr

The present invention relates to a recombinant protein for siRNA delivery, which allows the efficient intracellular and *in vivo* delivery of siRNA. More particularly, the present invention relates to a recombinant protein that allows a siRNA binding protein to be located in the interior cavity of a capsid protein of HBV (Hepatitis B virus), in which siRNAs of interest bind to the siRNA binding protein to be encapsulated within the capsid shell, thereby providing stability against external attack such as nucleases and achieving the efficient intracellular and *in vivo* delivery of siRNA by its release into the cytosolic space after cell uptake.

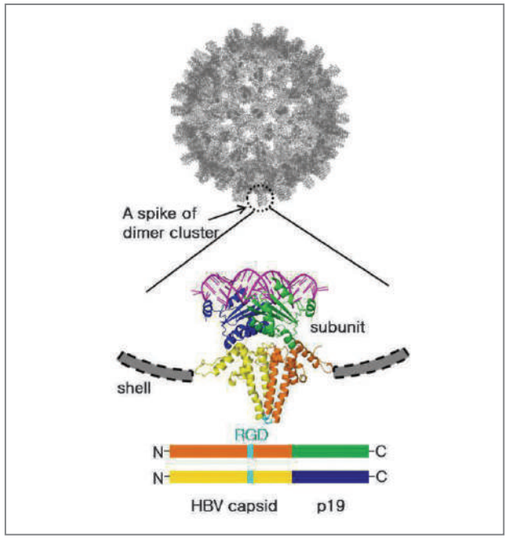

3-dimensional displaying apparatus using line light source

US 8951129 (2015.01.21)

Sung Kyu Kim / kkk@kist.re.kr

The present disclosure relates to a 3-dimensional displaying apparatus using line light sources, which includes: a display panel having a plurality of pixels; a backlight panel having a plurality of line light sources disposed to be spaced apart from each other by a predetermined distance, the backlight panel being spaced apart from one surface of the display panel; and a distance-adjusting unit for adjusting a distance between the backlight unit and the display panel. According to the present disclosure, it is possible to display autostereoscopic images which may minimize the quality deterioration of 3-dimensional images according to the change of distance from an observer to the 3-dimensional displaying apparatus, which is a problem of a displaying apparatus implementing 3-dimensional images by using a general parallax separating unit.

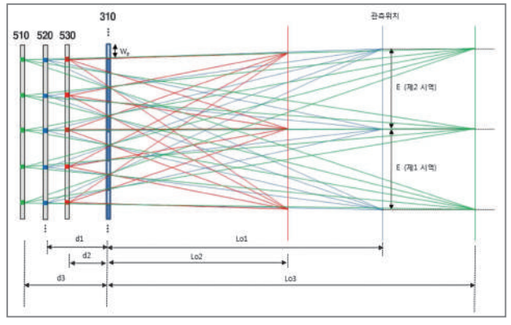

1. KIST R&D EXPO 2014: Idea Festival for Young Researchers

December 4, 2014

KIST held the KIST R&D EXPO 2014 on its Seoul campus to bring together young researchers with more senior scientists for an exchange of research ideas and expertise. The EXPO is an annual event intended to heighten public awareness of KIST's research activities.

During the 2014 EXPO, various events were scheduled that highlighted the most creative ideas currently under investigation, with a particular emphasis on research convergence. This topic was the focus of many morning sessions which introduced the work KIST is performing in this area as well as its prior accomplishments.

During the afternoon session, teams of young researchers from different fields exchanged ideas. There was also a Junior Symposium in which young researchers, junior researchers, and graduate students introduced their research topics and dissertations.

The Pioneer Award ceremony was also held in the afternoon. The evaluators for the award were not only experts in the field, but also lay people, such as students and administrative staff. They collectively selected the idea that was the easiest to understand and the most relevant for everyday use. The winning teams will be announced in the near future and will be awarded grants for their research. In a similar vein, an Idea Contest was held with 198 students from junior high and high schools participating. 12 of the best ideas were chosen by a group of judges composed of patent attorneys, researchers and science teachers.

Other events at the EXPO included a ceremony to commemorate the transfer of commercial technologies and patents to KIST business partners, and an award ceremony for outside researchers who have made significant contributions to joint research projects.

In the words of President Byung Gwon Lee of KIST, "The KIST R&D EXPO is organized and administered independently by researchers themselves. The purpose of this event is to have a venue for researchers to share their works without any interference from the government."

2. KIST Celebrates 49th Anniversary

February 10, 2015

On February 10, KIST held a ceremony to commemorate its 49th anniversary. Approximately 500 dignitaries, officers and employees attended this event, which showcased the major activities and achievements of the past year while presenting plans for the coming one. In anticipation of KIST's 50th anniversary next year, the emblem of the 50th anniversary was unveiled. Additionally, awards were presented to outstanding departments and employees.

KIST activities addressed at the ceremony included:

- the launch of two new institutes in January, the Post-Silicon Semiconductor Institute and the Robotics and Media Institute;
- the implementation of improved methods for the

administration and evaluation of research projects;
- cooperation with the government to establish the "Global Complex of Creative Knowledge and Science" in Hongrung, Seoul;
- taking a lead role to promote convergence and cooperation among universities, businesses and government-funded research institutes;
- providing assistance, such as with the V-KIST project, to developing countries trying to expand their S&T capabilities.

The ceremony emphasized how KIST is now preparing for new challenges as it increasingly looks beyond its national borders to establish itself as a leading R&D institute on a global scale. President Byung Gwon Lee suggested new roles for KIST over the next 50 years, saying "KIST will lead R&D innovation so as to identify new research themes which respond to changing times and people's expectations and will create tangible outcomes of importance to the nation."

3. "Nanoscience is Fun to Teach"

December 11, 2014

KIST hosted a two-day nanoscience (nanomaterials) education program for junior high and high school science teachers on its main campus in Seoul starting on December 11.

This program was designed to sharpen science educators' knowledge of nanoscience. The main curriculum focus was to teach real life applications of nanoscience and technology. The theme of the first day was an introduction to solar cells and nanotechnology followed by lectures on the application of nanotechnology to the field of bio-medical diagnosis. During the lab tour, participants had opportunities for hands-on experience with nano-equipment and were able to engage in conversations with researchers. On the second day, theories of nanoscience and analysis technology as well as nanoscience and semiconductor technology were addressed. Participants also learned about 3D printing technology, the application of nanotechnology, and

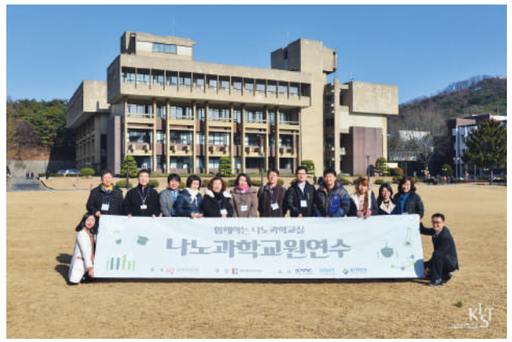

discussed the production of science education material.

In explaining the purpose of KIST's nanoscience education initiatives, President Byung Gwon Lee of KIST commented, "After meeting many science teachers, it became apparent that not only students, but also educators, needed further experience and education in nanoscience. This program commenced after educators from Gwangju, Suwon and Pohang asked KIST to provide them with programs that would improve their nanoscience teaching skills."

Won-jeong Chang, an educator from Nowon High School had positive comments about the program, "I chose to take part in this program to improve my understanding of nanotechnology. Since I had very limited exposure to nanotechnology, it was difficult for me to teach students about the subject. I am confident that what I've learned through this program will be proven very useful at my school." He added, "There should be more of these programs where science educators can receive education job training."

This program is part of an outreach project undertaken by KIST as a member of the Korea Foundation for the Advancement of Science and Creativity and is supported by the Korea Advanced Nano Lab Center, National Institute for Nanomaterials Technology and Nanotechnology Accumulation Center. The program is funded by the government through the sale of lottery tickets.

4. KIST and Woori Bank To Aid in Funding Small- and Medium-Sized Technology Businesses

February 9, 2015

KIST and Woori Bank have agreed to provide systematic financing to small- and medium-sized enterprises (SMEs) which are developing and marketing outstanding technologies. SMEs which demonstrate excellent technological capabilities but lack specialized managerial expertise will now be able to receive comprehensive help in business management strategy, finance, operations and tax affairs management.

These arrangements were formalized through the signing of a MOU on February 9 in the presence of Lee Byung-gwon, President of KIST, and Lee Kwang-gu, CEO of Woori Bank. In accordance with the MOU, SMEs with outstanding technology capabilities and high growth potential can receive systematic technology financing support without having to pay technology evaluation fees. In addition, a comprehensive solution designed to support overall business management, from management strategy to finance, operations and tax planning, will be provided to SMEs which face difficulties in securing staff with the necessary expertise in business administration.

KIST and Woori Bank will first provide support to members of the K-Club, which was established by KIST in 2013 for the purpose of supporting SMEs, and will gradually expand the scope of recipients. On the day the MOU was signed, Compass Systems, a member of the K-Club, entered into a contract with Woori Bank to receive Woori Creative Technology Business Credit. This financing support will enable Compass Systems to get a jump on technology development and marketing so as to exploit new markets.

Regarding the arrangement, Chairman Byung Gwon Lee said, "KIST will continue to provide substantial support so that technology-competent SMEs can grow into competitive global players." Similarly, Lee Kwang-gu, CEO of Woori Bank, commented, "We will provide systematic financial support at favorable interest rates in order to boost the growth of KIST's family companies and competent SMEs."

5. Cooperation of State-Funded Research Institutes Advances Korean Lunar Exploration Efforts

March 15, 2015

Advanced research on lunar exploration by 15 state-funded research institutes, initiated as a cooperative project in January 2014, is already making substantial progress. This research involves the development of a moon explorer, payload, ground stations for a Korean deep-space network and lunar exploration rover. This research is particularly significant in that all the participating state-run research institutes are voluntarily contributing to the budget of KRW 7.3 billion.

Important progress was achieved over the past year. First, the core technologies necessary for the Korean lunar exploration project were identified and the direction of research was defined. It is particularly noteworthy that specific technologies applicable to the Korean lunar exploration project have already been developed and are owned by the participating institutes.

For instance, the core technologies of aerospace secondary cells and weight reduction are applicable to explorers (supervisory institute: KASI). High definition camera technologies are applicable to payload equipment (supervisory institute: KASI). There were discussions on cooperation with NASA over specification design and

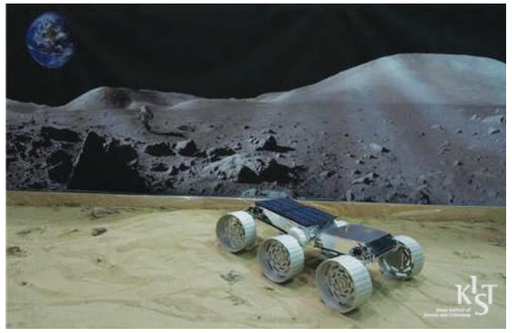

core control technology analysis for the development of deep space antennae for lunar exploration (supervisory institute: ETRI), and the development and operation of ground stations for a Korean deep-space network. In addition, the research institutes developed the design of a double body mechanism resistant to the environment on the moon and created a model to test lunar exploration rover technologies (supervisory institute: KIST).

This year, the participating institutes will conduct further research on the applicable technologies which were identified during the first year of the convergence research. All of these research activities will be conducted using the institutes' own financial resources, led by the Korea Aerospace Research Institute. Moon Hae-ju, Head of Science, Nuclear, Big Science Bureau at the Ministry of Science, ICT and Future Planning, said, "It is very encouraging that the 15 state-funded research institutes made such achievements through voluntary cooperation. They set a good example of cooperation among research institutes. Going forward, continuous research on convergence will contribute to the successful implementation of the lunar exploration project, and the Ministry will certainly secure a budget for the project next year and let the state-funded research institutes concentrate more on research."

6. KIST Enters into Research Cooperation Agreement with ITAE of Italy

April 22, 2015

On April 22, KIST signed a research cooperation agreement with The Institute of Chemical Methods and Processes for the Transformation and Storage of Energy (ITAE), an energy research institute operated under the National Research Council (CNR) of Italy. This agreement follows a previous agreement between the National Research Council of Science and Technology and CNR of Italy, signed on November 27, 2014.

The two parties agreed to facilitate joint research in the field of hydrogen fuel cells and promote cooperation through personnel exchange, joint symposiums and development of joint research topics in the fields of fuel cells and hydrogen production and storage.

The signing ceremony took place as part of the Korea-Italy Hydrogen and Fuel Cell Symposium which was co-hosted by KIST and the Italian Embassy in Korea as part of the Global Research Lab Project of the Ministry of Science, ICT and Future Planning.

The Advanced Analysis Center at KIST

The Advanced Analysis Center supports organic and inorganic chemical analysis, ultra-fine surface analysis, nano structure analysis and proteome analysis. An analysis center has been in existence at KIST since the opening of the institute in 1966, but its activities were limited to in-house chemical analysis and materials testing. Now however, with the significant expansion of the scope and depth of research activities and facilities around the country, as well as greater cooperative and convergent research, it has become the country's leading analysis center. Significantly, its facilites are open not just to KIST researchers, but also to other Korean and international researchers.

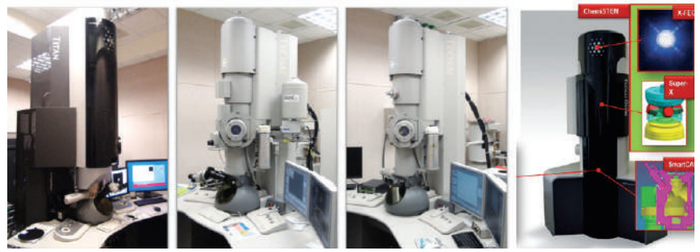

Transmission electron microscopy equipment
(TEM models: Tatan, Tecnai F20, Tecnai Cryo TEM, Talos)

XRD open lab

In recent years, there has been a realignment of research areas at KIST which involves a convergence of nano, elements, material and bio-technology into energy, circular environment technology and new medicine development. More specialized analysis is required to support these key research areas. Moreover, as some 10,000 cases of analysis are conducted nationally each year, advanced analysis is becoming a cornerstone for research conducted at universities and companies. The Advanced Analysis Center represents an invaluable resource for this expanding wave of analysis-based research.

A summary of the five major areas of analysis conducted at the center is included below.

1. Electron microscopy

The KIST Advanced Analysis Center houses equipment necessary in the development and commercialization of nano elements, specifically, transmission electron microscopy (TEM), environmental scanning electron microscopy (SEM) and focused ion beam (FIB). With this equipment, it is possible to analyze traditional structures based on TEM diffraction and identify the chemical bonds and electron structure of material. In certain cases, the structure of atoms can also be analyzed. In

SEM open lab

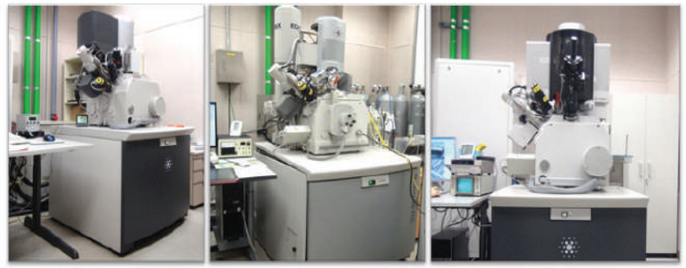

FIB equipment (FIB models: Nova600, Quanta3D, Hellos)

addition, advanced analysis that uses X-rays and SEM can obtain information at the atomic level which can be used as a tool for analysis of the structure of semiconductor material. This integrated operation enables the statistical processing of all operational data, enhancement of utilization and higher data reliability.

A FIB system is similar to SEM except it scans the surface of samples with ion beams rather than electronic beams, allowing applications such as complex imaging, real-time fracturing, micro processing, the production of TEM specimens and insulation or partial vapor deposition. FIB can evaluate the mechanical, electrical, thermal and chemical properties of nano materials in conjunction with electron microscopy observation. KIST is now equipped with three FIB systems.

2. Accelerator analysis

Synchrotron system

Understanding the unique physical properties of nano crystals, nano thin films and nano clusters requires the accurate analysis of the atoms and electron structures of the surfaces and interfaces of semiconductors and metals as well as nano elements and material. High brilliance, high collimation, photon energy tunability and polarization enable a wide range of analysis on minute elements or ultra-fine structures. Therefore, technology that uses radiation light sources can analyze minute elements of material, ultra-thin films with dozens of atom layers and nano structures on a nanometer scale.

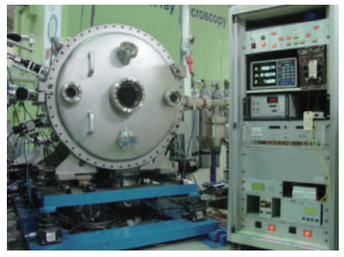

10D XAS KIST B/L and 1D XRS KIST-PAL B/L equipment

KIST has installed an absorption spectroscopy beam line (7B1 KIST) of soft x-ray areas onto the Pohang light source accelerator to carry out experiments of X-ray absorption spectroscopy and scattering of nano thin films, nano powder material, amorphous metal material and high molecule material. It is usually used to measure NEXAFS (near-edge x-ray absorption fine structure) and soft X-ray reflectivity.

A second KIST beam line (10B1 KIST-PAL XRD) of hard x-rays, operating since 2008, enables EXAFS (extended x-ray absorption fine structure) and HRXRD (high resolution x-ray diffraction). It uses Si(111) single crystal as monochrome equipment. Radiation EXAFS analyzes the properties of x-ray absorption of the absorption edge of certain elements and provides information on the kinds, distance and bonds of neighboring atoms as well as information on chemical bonds, based on changes in electron structure around the absorption edge. Thus, the local minute structure of nano materials, elements and mechanism of physical properties can be identified.

Mid- to large-sized 6MV electrostatic ion beam accelerator

KIST has been operating a mid- to large-sized 6MV electrostatic ion beam accelerator since February 2013. It can be used for archaeology, semiconductor research, new medical approaches, and other areas. It enables age dating and the latest biological and material research. Through the accelerated collision of elements that have high energy with a target material, the energy of x-rays and scattering particles can be measured, providing valuable information. This type of accelerator enables measurement of heavy and diverse radio-isotopes such as aluminium, chlorine, iodine and calcium that have been difficult to analyze.

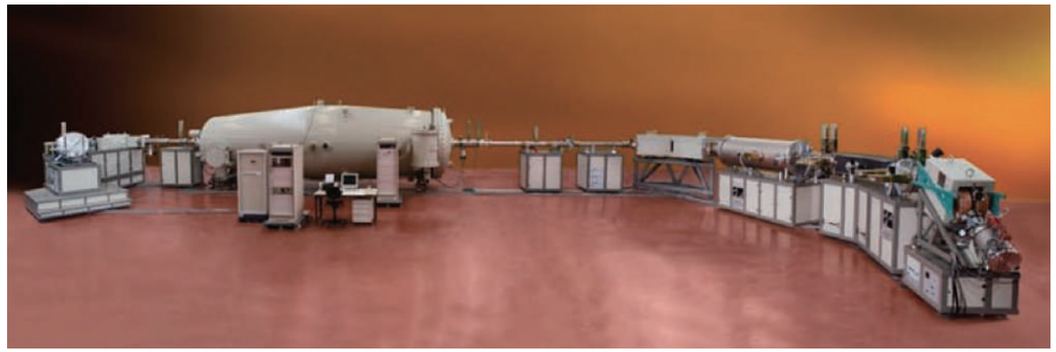

6 MV electrostatic ion beam accelerator

The newly opened ion beam accelerator facility is now equipped with 6 ion sources installed on three accelerators, providing services of a wide range of ion irradiation (hydrogen-uranium) of 30 keV to 60 MeV energy to Korea's semiconductor and other material researchers who have been hampered by the lack of an appropriate ion beam research facility. It is proving to be particularly useful in medical and biological fields because it enables trace analysis that measures individual atoms. For example, by injecting a minute amount of medicine attached to C-14 as a tracer, the medicine can be delivered and tracked without animal experiments. This is referred to as human-microdosing and can dramatically save time and money in the pre-clinical testing process.

Ultra-small angle neutron scattering instrument (KIST-USANS) installed at the cold neutron testing building of the Korea Atomic Energy Research Institute

Ultra-small angle neutron scattering instrument (KIST-USANS)

KIST has been operating an ultra-small angle neutron scattering instrument (KIST-USANS) installed at the Korea Atomic Energy Research Institute since December 2012.

It is KIST's cutting-edge neutron research equipment for material structure analysis with a ㎛ size. This equipment enables qualitative and quantitative measurement of liquid and solid material at a micron (1000 ㎚) or sub-micron (100㎚) size. With the use of neutron beams produced by a nuclear reactor at the Korea Atomic Energy Research Institute, the structure of internal materials and kinetics information can be obtained. Such information cannot be obtained by other equipment.

RBS

Starting with a 2 MV tandem particle accelerator purchased from an American company, NEC, the center has installed a wide range of analysis systems such as RBS (Rutherford Backscattering Spectrometry),

channeling, ERD (Elastic Recoil Detection), resonance scattering, and PIXE (Proton Induced X-ray Emission). With such systems, the center can now provide nondestructive quantitative analysis services on hydrogen, light elements and minute amounts of heavy elements on a ppm scale, thus contributing to the development of research in semiconductors, ceramics, metals, high molecular and new material areas. Because the KIST 2 MV accelerator is equipped with a 120 kV implantation beam line and MeV implantation beam line, it can be used for analysis and physical and chemical property reforming.

RBS instrument for the nano-analysis of material surface (Model: NEC 6SDH2)

3. Nano surface analysis

The center has installed high-end surface analysis equipment and utilized these technologies for surface and material analysis and assessment. Complex component analysis of high molecular material, semiconductors, metals, ceramics and other solids is now possible based on surface measurement technology, and a wide range of surface analysis methods has been developed to successfully identify almost all kinds of organic and inorganic material.

Dynamic Secondary Ion Mass Spectrometry (D-SIMS) is representative of cutting-edge surface analysis and can be used for component trace analysis of material and elements, quantitative analysis of minute amounts of component, multi-layered and minute area analysis. With such a sophisticated analysis capability, KIST can successfully carry out large state-funded projects related to nano technology, including nano material technology development, spintronics and tera bit nano elements. This analysis technology is playing an important role in the development of next-generation semiconductors based on trace analysis of ultra-fine material of several nanometers thickness such as in magnetic thin films and is providing essential information to assess the surface properties of advanced materials such as metals, semiconductors, ceramics and high molecular materials.

Surface analysis that uses SIMS includes qualitative and quantitative analysis of surface composition elements, molecular strucuture analysis, mapping vertical distribution map (element distribution analysis of depth), and image analysis. This technology is not only used for measuring the vertical distribution of ultra-thin films with several nm of resolution, but also for analyzing thick insulation specimens of ㎛ size.

X-ray photoelectron spectroscopy (XPS) measures the kinetic energy of electrons that are released through X-ray scanning of short waves to the material surface, identifying bonds of electrons within an atom on the specimen surface. It is used for identifying interactions of semiconductors occurring in the process of element assembly. It is also used for cleaning semiconductor surfaces, growing thin films of oxidants or analyzing processes such as element scanning. XPS provides appropriate and accurage information regarding chemical changes that occur at the interface between thin films in the case of elements such as heterojunction or quantum well structure. XPS has also been a boon to biomaterial research by providing detailed information on interactions in the interfaces between inorganic materials and bioorganic molecules.

Auger electron spectroscopy (AES) is another example of a technique used for surface analysis. It is used primarily to determine elemental compositions of materials and, in some cases, to identify the chemical states of surface atoms. The biggest advantage of AES is in analyzing localized areas through the focus of electron beams to obtain an enhanced image of surface topography in nano-sized spatial resolution.

4. Trace analysis

The center has the capacity to analyze trace metal components using atom absorption spectroscopy (AAS), X-ray fluorescence (XRF), X-ray diffraction (XRD), carbon-sulfur analysis equipment, and ultraviolet-visible (UV-VIS) spectroscopy. In addition to examining traces of metal components, these technologies allow analysis of fire-resistant and rare-earth elements without the need for complex separation or concentration processes. More than 80 elements can now be precisely analyzed with the center's equipment. The center is providing essential services for component analysis to support hydrogen fuel cell projects, chemical engineering, nano material research and other important fields.

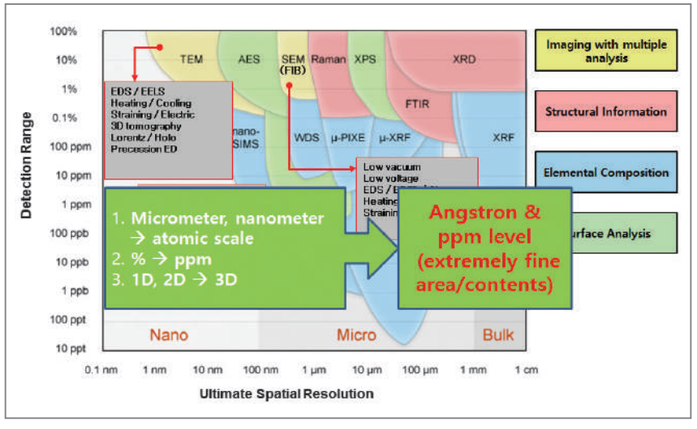

Trace analysis roadmap

5. Nuclear magnetic resonance analysis

KIST installed 900 MHz NMR equipment in December 2005 and has utilized it for proteomics, bio technology and new medicine development research. This equipment is one of only about 20 units in the world and is the most sophisticated device currently available for biometric molecule structure analysis.

The structure analysis method that relies on NMR is the only way to interpret the tertiary structure of biometric molecules on an atomic level, including proteins and nucleic acids found in a solution state. It enables identification of the bond state and structure of bioactive low molecule compounds versus biometric high molecule matter. Such structure information is essential for industries involved in the development of pharmaceuticals and other medical advances.

KIST is actively focusing on the fields of proteomics, chemoinformatics and metabolomics, source technologies for advances in disease diagnosis and new drug development, considered important avenues for future economic growth. KIST's large magnetic resonance equipment is critical for providing the type of in-depth and comprehensive structure analysis research that will support this new product development.

Conclusion

The KIST Advanced Analysis Center is conducting research, development and support for analysis technology by building and operating the world's most advanced and large-scale analysis equipment. In addition, the center has been open to analysis research by both Korean as well as international scientists and has continuously supported joint research activities. The expertise developed through 50 years of research combined with investment in the most advanced technologies and equipment ensure that the center will continue to provide the type of support and leadership needed to enable scientific breakthroughs.

Junku Yuh, Director-General

Robotics and Media Institute

Q1 This January you launched a research institute specializing in robotics and media. What was the background behind the launch of the institute and what changes will be necessary to make this new institute a success?

The establishment of the Robotics and Media Institute made sense for KIST since it already had outstanding expertise in this field, including research personnel with the requisite experience. KIST currently has around 60 researchers in robotics, which is an exceptionally large number compared to other government-funded research institutes. We have 45 full-time researchers assigned to the Robotics and Media Institute as well as other researchers who have relevant expertise working within other special institutes at KIST, such as the Biomedical Research Institute. Moreover, robotics is one of KIST's competitive strengths, as evidenced by its cotinuous inclusion in the Frontier Project, headed by Dr. Moon-Sang Kim, the Global Frontier Project, led by Dr. Bum-Jae Yoo, and the launching of a number of related commercial start-ups. The robotics field has been identified as an important driver of future national economic growth, which has led to a strong commitment by KIST's management to develop a stellar robotics research institute through convergence of science and technology with information communications technology (ICT). For all these reasons, I can say that the Robotics and Media Institute represents an essential activity for KIST.

An important change expected with the launch of the institute will be to gather researchers dispersed throughout the organization under one roof to concentrate their expertise in robotics and media. This will make it easier to perform large-scale research projects and generate significant outcomes. Such a change would give us not only the necessary scale to achieve results, but would also ensure competitiveness in robotics-media research.

Q2 What is the vision of the Robotics and Media Institute? Tell us about your core research topics and how they will be executed.

The vision of our institute is to be the world leader in robotics and media research. Our aim is to become a leading global research group developing cutting-edge technologies that converge robotics·media·ICT. The results of our research, involving both commercial and humanitarian applications, would improve the safety, security, health, education and welfare of the nation and the wider world.

The institute's flagship project is designed to achieve several important goals: 1) to be oriented to issues of future importance; 2) to provide for participation and collaboration among all the diverse research specialists associated with the institute in the areas of robotics, media and ICT; 3) to be completed within three years; and 4) to benefit the public. The project has been named "Connected Active Space (CAS) for X." It combines some of the *Internet of Things* concept with the previously proposed concept of *Smart Space*. In contrast to Smart Space, whose focus was rather passive, CAS is a concept that includes actions using robotic technology. X refers to the subject and what becomes X determines the completion.

For this first project, we will specifically target the elderly. Korea is already a society with a high proportion of seniors; therefore, social issues involving their health, safety and security are of paramount importance. Many analyses on future trends, including those reported by the National Research Council of Science and Technology, all point to the aging population as a primary issue, so this project topic is particularly relevant.

It will take some time to crystalize the specifics of the research, but we are thinking of making the hospital room the focus of our work. For example, a hospital bed could become a type of robot so that a patient would not have a hard time going from a bed to a wheelchair. This would complement current efforts by the Korean government to implement a *Comprehensive Nursing Service* in which family members are no longer required to look after a hospitalized patient. This service is already being tested at some hospitals, including Samsung Medical Center. In light of this and other initiatives, we need to develop systems that not only support hospitalized patients and the elderly, but also their family members and caregivers to make patient care easier and more convenient. Through technology, we are planning a system that would allow a patient to more easily navigate to the bathroom and support their mobility. Following implementation in a hospital setting, this technology could be applied to nursing homes and other care institutions. To accomplish this, we would need to conduct further clinical trials, but what we are trying to do here is to systemize our strengths in combining elemental technologies, and I believe that the Robotics and Media Institute can do a great job in this area.

Q3 As Director-General of the institute with full responsibility for administrative decisions, what will you be focusing on from an operations standpoint?

Before the launch of the Robotics and Media Institute, robotics and media researchers working within many different institutes and divisions at KIST could be evaluated unfairly or unreasonably when compared with researchers in other fields. For example, if a performance standard requires Journal Citation Reports in the top 20% of journals, there are extremely few journals in the robotics field to satisfy that criterion. Moreover, in the field of robotics-media, technology trends shift so rapidly that the typical one-year lag from submission to publication means that a significant advance can already be dated by the time of publication. It is my goal that researchers now consolidated under the institute's umbrella will not be at a disadvantage under the evaluation standards we apply. We need to think about how to attribute "value." Which is more important, the contribution generated in the field by a new idea or a well-written paper? The key is to find a balance between the two. Further discussion is required before we formulate our own evaluation method, but this can be accomplished through frank discussions combined with communication and understanding with other specialized institutes of KIST which have already gone through the process.

Another focus of institute operations will be to bring in researchers who have achieved particular prominence in their respective fields. We have many renowned researchers at the institute, including Dr. Sung-Kyu Kim, an expert in human computer interaction (HCI) 3D display, who is set to receive an award from the Minister of Science, ICT and Future Planning, and Dr. Sung-Chul Kang, the developer of a micro-surgical robot which was named as one of the country's top ten science and technology achievements of 2014. Dr. Kang was able to produce this result in only three years, a fact which attests to the high level of technical acumen of our researchers.

Although it will take some time, my plan is to provide support to all our research staff so they can develop into world-class researchers in their specific sub-sector. I believe our flagship project will help us along this journey.

Q4 Robotic technology is already widely used in our lives, examples being the back-up collision warning system and the car navigation system. You are a world-renowned expert in marine robots. Can you comment about the direction of new technology development in robotics·media?

When most people hear the word "robot," they think of cartoon heroes like Astro Boy Atom or Robot Taekwon V; however, at the institute what we pursue is more aptly termed robotic technology. There is still a long way to go until we see robots like Astro Boy Atom or Robot Taekwon V in our ordinary lives, but robotic technology is much more present in our lives than we think. In the late 1990s, people were skeptical of the implications of words like "automation" and "autonomous" and were fearful and put off by robots replacing humans in the workplace. They were uncomfortable with the idea of a robot wielding a surgical blade, but nowadays we have devices such as the da Vinci surgical robot performing complex medical procedures. Similarly, the U.S. military is working toward a fully unmanned system, deploying drones quickly and replacing one out of three air combat missions with unmanned combat planes.

Marine robotics is my specialty, and in the 1990s, I carried out a project with an underwater vehicle termed, not autonomous, but semi-autonomous, because of the aversion to the concept of automation. In other words, the study involved a system that was autonomous and unmanned for regular operation, but which was monitored by a human at all times so that if anything went wrong the human could immediately interrupt the operation. Today, by contrast, hospitals often advertise their surgical robots, while cleaning robots have become quite ordinary. This reflects how robotic technology is becoming more widely accepted in our lives. I believe that robotic·media technology will continue to become more prevalent around us and used to bring convenience and safety to all aspects of our lives.

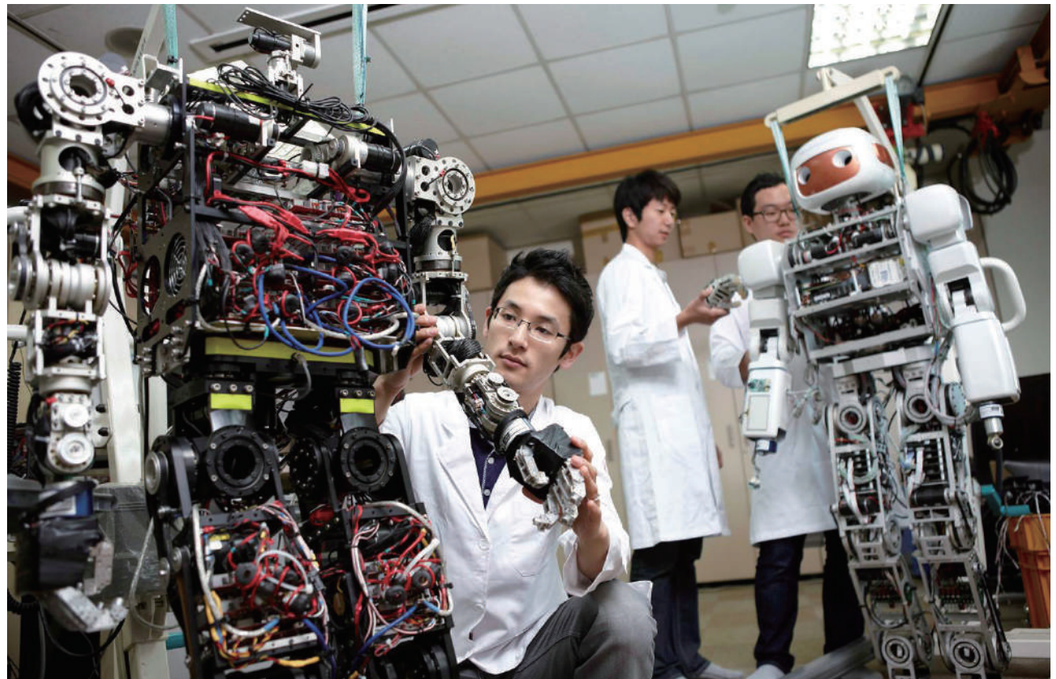

Q5 It seems like collaboration with business is ever more important to commercialize the achievements of research institutes. What do you think is needed or should be improved to successfully commercialize robotics-media breakthroughs?

I think using the concept of the ecosystem is very important if we are to industrialize robotic technology. In other words, many parts need to work together to make a complete whole. For this to be effective, I believe there are certain things that research institutes, business and the government each should do. Research institutes should undertake research that nobody has ever done before, such as develop source technologies, and business should take the lead in commercializing these technologies. The government's role is to link these two parties together to create a seamless cycle. Even when an exciting new technology is developed, it can be difficult to commercialize if the cost is too high. For example, robotic technology depends on readily available and reasonably priced component parts. To keep costs down, we need

access to these components, but Korea is still very weak in the components industry, so I believe that we need to solve that issue first.

We should also think about developing products in overseas locations or globally outsourcing technologies. In the case of robotics·media, it is very difficult to create a market by relying exclusively on domestic demand, so we have to keep our eyes on overseas markets as well. Actually, overseas markets should be considered from the beginning of product development; not just robots, but all technology-based products cannot be successful by targeting only the domestic market. We need strategic approaches that looks at all these factors for companies to manufacture products that are truly competitive. Only with the creation of a sound ecosystem in which research institutes, business and the government cooperate fully can the commercialization of new technologies thrive.

Q6 You have held various positions in the U.S. in academia and at the National Science Foundation, and after coming back to Korea, served as President of Korea Aerospace University for seven years before joining KIST last year. What are your opinions on ways for government-funded research institutes to become competitive in this era of convergence·collaboration?

I believe that Korean government-funded research institutes need to be more sensitive to demographic trends. What I mean is that they need to prepare for a reduction in the number of researchers in Korea caused by the overall population decrease. Already, people talk about more than half of the universities in Korea closing down. It might be a bit of hyperbole to say this, but in simple mathematics that would mean that the number of researchers would drop by half. We need to predict and be prepared for a situation where we would need to effectively utilize this more limited number of researchers.

In Korea, researchers are largely concentrated at government-funded research institutes, research-focused universities, and company research labs. Ultimately, we need to encourage ways for these pools of researchers to work together to ensure future competitiveness. Currently, universities and government-funded research institutes are somewhat in competition with each other to win research funds as they follow a strategic approach. In the U.S., a project is assigned to multiple research teams, which allows the best outcome to be selected for future use, but in Korea, it is difficult to support funding multiple teams simultaneously due to limitations in resources. Considering this, we need to think of some different structure to achieve the most effective outcome. The U.S. system has its own set of issues, of course, but we need to look at these kinds of diverse approaches to make the best use of our pool of researchers. In other words, we need to take a broader view and consider different research entities not as competitors, but more as partners for collaboration and openness to achieve greater research outcomes.

Q7 What are your plans and goals in 2015?

KIST is an organization with an impressive history and it already has great systems in place, but since we're starting a new institute, there are many things to organize. I have been with KIST for just two years so I have a lot to learn about the personnel structure and other systems at KIST. In order to learn, I am trying to listen a lot. I try to listen to various members of our institute and keep communication flowing. Personally, as a new employee with diverse experiences, I believe I am able to contribute to the institute by offering a fresh perspective and seeing issues from a different angle than those who have been with KIST for a long time. I plan to put my best effort into building an open, creative and effective environment for robotics-media research.

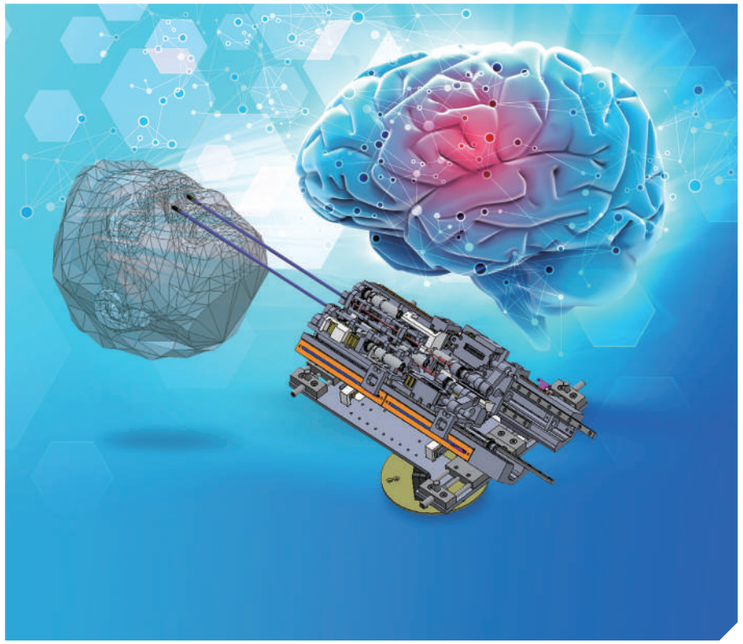

Cover image : **Microsurgical robot for endonasal skull base surgery**

Editorial Information

Editor-in-Chief

Tae Hoon Lim

Editorial Board Members

Hae-Young Koh
Hyun Kwang Seok
Il Ki Han
Joonyeon Chang
Youngsoon Um
Seok Won Hong
Jongjoo Kim
Byung Soo Park

Managing Editor

Sang-A Chang
sarachang@kist.re.kr
+82-2-958-6039
Web Address
www.kist.re.kr/en

English Advisory Services

Anne Charlton
The Final Word Editing Services
the_final_word@live.com

Korea Institute of Science and Technology

Hwarangno 14-gil 5, Seongbuk-gu, Seoul 136-791, Republic of Korea
Tel +82-2-958-6039 www.kist.re.kr/en
E-mail sarachang@kist.re.kr

Post-Silicon Semiconductor Institute

A future that lies beyond silicon electronics

KIST's Post-Silicon Semiconductor Institute is working to develop advanced semiconductors using new materials and exhibiting superior performance to silicon-based technology. The goal is to produce semiconductors that are 10x faster and use 1/10 the current power consumption.
Research is focused on oxide semiconductors, spin electronic devices, opto-electronic convergence devices and attachable electronic devices for health monitoring.

KIST
Korea Institute of Science and Technology